UNIVERSITÉ DE GENÈVE
Département de physique nucléaire
et corpusculaire

FACULTÉ DES SCIENCES
Professeur Allan CLARK

Measurement of the Cross Section for Production of Prompt Diphoton in $p\overline{p}$ Collisions at $\sqrt{s} = 1.96$ TeV

THÈSE

présentée à la Faculté des sciences de l'Université de Genève
pour obtenir le grade de Docteur des sciences, mention physique

par
Yanwen LIU
de la Chine

Thèse N° 3571

GENÈVE
Atelier de reproduction de la Section de physique
2004

Contents

Abstract **5**

Acknowledgments **7**

1 Résumé **9**

1.1 Introduction théorique 10

1.2 Le collisionneur et le détecteur 12

1.3 La mesure de la section efficace de deux photons 14

1.3.1 La sélection des candidats 14

1.3.2 Soustraction du bruit de fond. 15

1.3.3 Sections efficaces 17

I Theoretical Introduction **21**

2 The Standard Model of Particle Physics **22**

2.1 Physics 22

2.2 The Standard Model of Particle Physics 23

2.2.1 Gauge bosons 24

2.2.2 Leptons and Quarks 25

2.2.3 Scalar fields and Higgs Mechanism 26

2.2.4 Parameters in the Standard Model 29

3 Perturbation theory and diphoton production **31**

3.1 Perturbation theory 31

3.2 Diphoton production in $p\overline{p}$ collisions 33

II Experimental Setup 46

4 Tevatron 47

4.1 Accelerator 47
4.2 The luminosity 49

5 The CDF II experiment 52

5.1 The CDF coordinate system 52
5.2 An overview of the detector 55
5.3 The tracking system 55
5.4 The calorimetry 58
5.4.1 The Central Calorimeter 58
5.4.2 The Plug Calorimeter 65
5.5 Muon detectors 66
5.6 The luminosity monitor 67
5.7 The trigger system 68
5.8 Offline reconstruction 69

III Data Analysis 73

6 The Analysis 74

6.1 Photon Identification 74
6.2 Data Sample 76
6.3 Monte Carlo Samples 83
6.4 Event selection 83
6.4.1 Detector Acceptance 83
6.4.2 Isolation 92
6.4.3 No-track cut 92
6.4.4 No extra CES cluster 103

6.4.5 Z-Vertex . . . 107
6.4.6 CES χ^2 and Had/EM energy ratio . . . 107
6.4.7 Summary . . . 109
6.5 Background Subtraction . . . 113
6.6 Efficiency calibration . . . 118
6.6.1 CES χ^2 Efficiency calibration . . . 118
6.6.2 CPR efficiencies . . . 120
6.6.3 Systematic uncertainty from background subtraction. . . . 121

7 Diphoton Production Cross Sections **125**
7.1 Data/Theory comparisons . . . 125
7.2 Conclusion . . . 131

Bibliography **143**

Abstract

This thesis presents the measurement of prompt diphoton production rate in proton-antiproton collisions at a center-of-mass energy of 1.96 TeV using the upgraded Collider Detector at FermiLab (CDF II). This process deserves some attention for the following reasons.

The $H \to \gamma\gamma$ decay mode is an important channel for the Standard Model (SM) Higgs boson searches in the low mass region ($M_H < 130$ GeV) at the forth coming LHC. In many models involving physics beyond the SM, cascade decays of heavy new particles generate a $\gamma\gamma$ signature. Some examples are supersymmetry with a light gravitino, radiative decays to a higgsino-LSP and models with large symmetry groups. The QCD production of prompt photon pairs with large invariant mass is the irreducible background to these searches. The rate is huge and requires to be quantitively evaluated prior to any of the possible discoveries. In a hadronic collider environment such as LHC, prompt photon signals are contaminated by the production of neutral mesons which decay to multiple collinear photons. The experience of classifying background of neutral meson source is very important.

The process can be used to test the Next-to-Leading Order (NLO) calculation of Quantum Chromodynamics (QCD). The 4-momentum of particles in the di-photon final state can be precisely determined due to the fine energy resolution of the electromagnetic calorimeters. The imbalance in the transverse momentum of the two photons reflects the transverse motion of the colliding partons. At collider energies, most of the transverse momentum of the incoming partons can be attributed to multiple soft gluon emissions prior to the collision, of which the effect to di-photon production can be resummed by Collins-Soper-Sterman (CSS) formalism [8]. The

Tevatron data can be used to test the resummation formalisms.

We have used 207 pb^{-1} of data collected by CDF II detector during the February 2002 to September 2003 running period to study the diphoton QCD production, and compared with next-to-leading order predictions. The background is subtracted using a statistical method based on the difference between the EM showers iniated by photons and by the backgrounds. The cross sections are measured as a function of diphoton mass, diphoton system transverse momentum and azimuthal angle between the two photons. The results are found to be consistent with perturbative QCD predictions.

Acknowledgments

This thesis could not have been completed without the help from many people, a few of which I would like to mention.

I would like to thank my supervisors Allan Clark and Xin Wu for the possibility to work at CDF, and the invaluable guidence they have provided during the past five years.

I am very much indebted to my advisors and co-workers in CDF photon group, Bob Blair, Ray Culbertson, Joey Huston, Steve Kuhlmann and other colleagues for their teaching me all the interesting stuff about the simple yet complicated particle, the photon. The work presented in this thesis is the first physics data analysis I have ever done. The coordinated debugging of the ShowerMax reconstruction code is not written down in the thesis. But I should not forget. I am certain that the analysis would take much longer to accomplish without these extremely responsive collaborators. I will not forget the panic I was in to when the Shower-Max detector was found to be behaving less nicely than in Run 1, and the guidence provided by these people to a solution. I would like to thank Bob for his having consistently supervised the analysis, and his accepting to be the jury at my thesis defence.

I would like to thank Gary Barker, Sung-Won Lee and Peter Wilson for their reviewing the analysis, and very constructively helping us improve the paper draft.

I would like to thank Csaba Balazs and Jean-Philippe Guillet for their providing and explaining the theoretic calculations.

It was a very pleasant experience to work with Annie Leger on the AMS board, and I benefitted from her grand expertise.

I would like to thank Martin Pohl for his accepting to be the jury at the thesis

defence.

I would like to acknowledge my Geneva/CDF colleagues, Andras, Mario, Mauro, Monica, Sofia for their help and the discussions over coffee, lunch and beers, which made the work at CDF and the stay at Fermilab enjoyable. In addition, I would like to thank Mario for his time spent reading my thesis and his thoughful comments which led to great improvements.

I would like to thank Bertrand Echenard for his great help to the French chapter of this thesis.

I would like to thank Catherine and Peggy for their help on all administrative issues in the past five years and their tolerating my poor French.

I would like to acknowledge Yann for his being extremely responsive to any computer-related issues in the university, and his very reliably adminstrating the systems.

Last but certainly not least, I would like to thank my wife, Qinqin, for her love, her patience and tolerance to a sometimes-absent-minded husband.

Chapter 1

Résumé

Cette thèse présente la mesure de la section efficace de production de deux photons isolés et prompts dans des collisions proton-antiproton à une énergie de centre de masse $\sqrt{s} = 1.96$ TeV observées par l'expérience CDF 2. L'analyse a été effectuée sur les données récoltées pendant la période avril 2002 - septembre 2003, correspondant à une luminosité intégrée $\int \mathcal{L}dt = 207 \pm 12$ pb^{-1}.

Cette thèse comporte trois parties :

1. Introduction théorique : Le chapitre 2 passe en revue les principaux aspects du modèle standard. La théorie des perturbations ainsi que les diagrammes les plus importants pour la production de deux photons sont présentés dans le chapitre 3.

2. Accélérateur et détecteur : Le chapitre 4 décrit l'accélérateur de protons et d'antiprotons Tevatron. La structure du détecteur CDF 2 est détaillée dans le chapitre 5.

3. Analyse : Le chapitre 6 est consacré à la description de l'analyse des données. Pour terminer, les résultats sont comparés aux prédictions théoriques dans le chapitre 7.

1.1 Introduction théorique

Le modèle standard est une théorie quantique des champs décrivant les interactions fortes, faibles et électromagnétiques des quarks et des leptons. Ses prédictions ont été vérifiées par de nombreuses expériences, le plus souvent avec une précision extraordinaire. Elle n'a pas encore été mise en défault et reste à ce jour la théorie qui décrit le mieux les diverses observations expérimentales. Le groupe de jauge du modèle standard est

$$G_{MS} = SU(3) \times SU(2)_L \times U(1)_Y \tag{1.1}$$

Le premier facteur, SU(3), désigne le groupe de jauge de la chromodynamique quantique (QCD), le groupe de la couleur. Le facteur $SU(2)_L \times U(1)_Y$ représente le groupe de jauge unifiant les interactions faibles et électromagnétiques. Il contient l'hypercharge faible $U(1)_Y$ ainsi que l'isospin faible $SU(2)_L$, l'indice L indiquant que seuls les fermions de chiralité gauche se transforment sous ce groupe. Le groupe de jauge de l'interaction électromagnétique, $U(1)_{e.m.}$, est un sous-groupe de $SU(2)_L \times U(1)_Y$. Le mécanisme de Higgs est introduit pour briser spontanément les symétries $SU(2)_L \times U(1)_Y$ autre que $U(1)_{e.m.}$ et générer la masse de deux bosons de jauge faibles, $W^{\pm}$ et Z^0. Appliqué à l'interaction de Yukawa, ce mécanisme produit également la masse des fermions. Le boson de Higgs reste de nos jours la seule particule prédite par le Modèle standard à ne pas avoir été detectée.

L'étude de la production de deux photons isolés dans les collisons proton-proton ou proton-antiproton présente de nombreux intérêts. Citons en premier lieu la recherche du boson de Higgs au LHC, dont la désintégration en deux photons devrait produire une signature caractéristique. Ce processus constitue par ailleurs un des principaux canaux de recherche du Higgs. De nombreux modèles de physique impliquant des interactions au-delà du modèle standard prédisent l'existence de nouvelles particules lourdes, leur cascade de désintégration devant produire une signal $\gamma\gamma$. Par exemple, certains modèles dit "Gauge-Mediated SuperSymmetry breaking" prévoyent la désintégration d'un neutralino en un gravitino léger plus un photon. Le production de paires de neutralinos produirait donc une signal $\gamma\gamma$ plus une énergie transverse

manquante. Signalons enfin que certaines résonances de mesons technicolorés pourraient se désintégrer en $\gamma\gamma$. L'étude de ces nouveaux processus requiert donc une bonne compréhension de la production de paires de photons dans les processus QCD.

La réaction $p\overline{p} \rightarrow \gamma\gamma$ est décrite au premier ordre (Leading Order, LO) par le processus $q\overline{q} \rightarrow \gamma\gamma$, illusté dans la Figure 1.1. Les processus d'ordre supérieur (Next-to-Leading-Order, NLO) incluent les diagrammes de type $q\overline{q} \rightarrow \gamma\gamma g, gq, \overline{q} \rightarrow \gamma\gamma q(\overline{q})$, comprenant des corrections réelles et virtuelles d'ordre $\mathcal{O}(\alpha_s)$, comme le montre les Figures 1.1b et 1.1c. Ces processus sont regroupés sous l'appelation de "two-direct". Etant donné que la probabilité de fragmentation d'un quark énergétique en un photon est d'ordre α_{em}/α_s, les processus impliquant la production d'un (zero) photon direct et un (deux) photon(s) issus de la fragmentation d'un parton apportent une contribution effective aux diagrammes de premier ordre. Les Figures 1.2 et 1.3 illustrent les processus où un photon, respectivement deux photons issus de la fragmentation d'un parton sont produits. L'ensemble de ces processus, comprenant les corrections réelles et virtuelles d'ordre $\mathcal{O}(\alpha_s)$, sont calculés à l'ordre NLO. On les appelle contributions de fragmentation. Finalement, la contribution du diagramme de boîte $gg \rightarrow \gamma\gamma$ (Figure 1.4) avec une boucle de quarks est supprimé à l'ordre $\mathcal{O}(\alpha_s^2)$, mais elle peut être appréciable dans certaines régions cinématiques, à petit x, où la densité de gluons est élevée.

La production de diphotons est calculée par deux programmes: DIPHOX [9] et ResBos [11]. DIPHOX inclut toutes les contributions mentionnées ci-dessus à l'ordre NLO, tandis que ResBos utilise les processus "two-direct" à l'ordre NLO et les contributions de fragmentation au premier ordre. ResBos contient toutefois le calcul de la ressommation des états initiaux comprenant une émission de gluons de basse énergie (initial state soft gluon resummation). Les effects de ces émissions sont particulièrement important lorsqu'on analyse l'impulsion transverse du système des deux photons, q_T, cette dernière étant décrite par une fonction delta au premier ordre et diverge lorsque $q_T \rightarrow 0$ dans le calcul NLO.

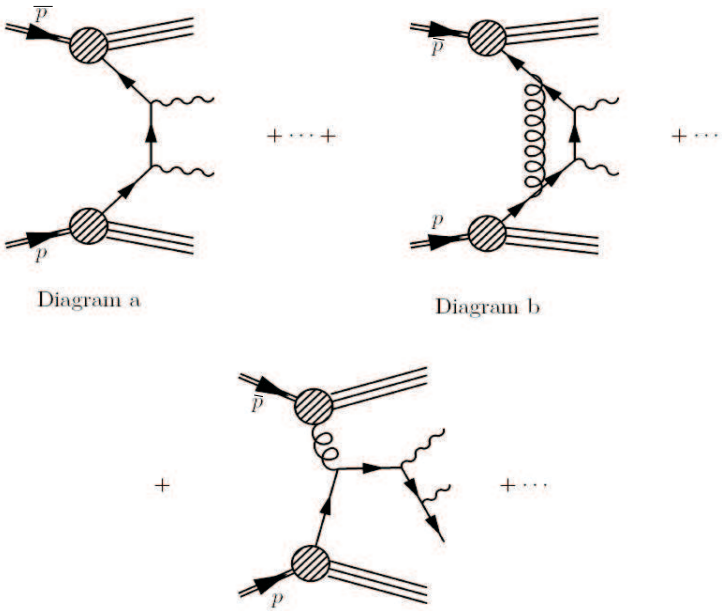

Figure 1.1: Exemple de diagrammes où les deux photons finaux sont produits dans des processus durs: ces contribution sont appellées “two-direct”.

1.2 Le collisionneur et le détecteur

Le Tevatron, situé au 'Fermi National Accelerator Laboratory' (FNAL ou Fermilab) à Batavia, Etats-Unis, est un collisionner proton-antiproton ayant une énergie de centre de masse de 1.96 TeV. L'expérience généraliste CDF (Collider Detector at Fermilab) est l'une des deux expériences construites sur cette accélérateur. Le système de coordonnées employé à CDF est le suivant: l'axe z est orienté dans la direction du faisceau de protons, l'axe x s'éloigne du centre de l'accélérateur et l'axe y se situe dans le plan perpendiculaire au Tevatron. L'origine du système d'axes se trouve au centre du détecteur. Etant donné sa géométrie cylindrique, il est souvent plus facile d'utiliser un système de coordonnées polaires. Dans ce cas, r désigne la distance entre un point et l'origine du système d'axes, ϕ l'angle azimutal qui se trouve dans le plan $x - y$ et θ l'angle polaire. On définit également la pseudo-rapidité η comme $\eta \equiv \log \tan(\theta/2)$.

Le détecteur CDF 2, version améliorée de CDF pour le RUN 2, est un spectromètre magnétique à symétrie cylindrique. En s'éloignant du point d'interaction,

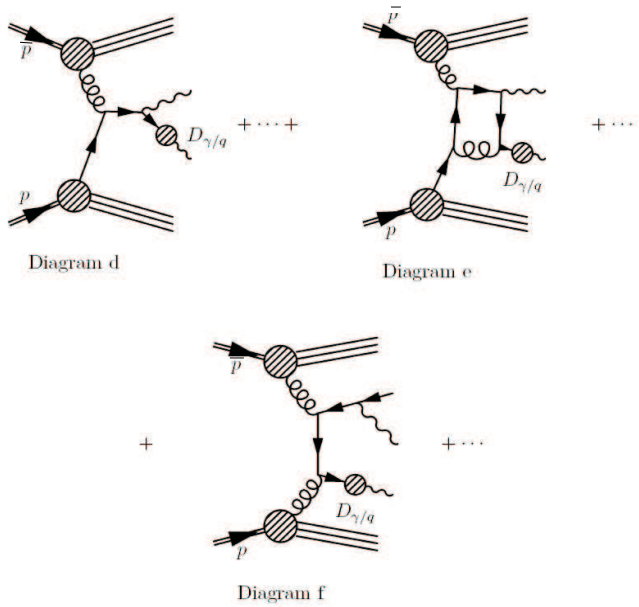

Figure 1.2: Exemple de diagrammes où un photon direct est produit ainsi qu'un photon issu de la fragmentation d'un parton. Ces contribution sont appellées "one-fragmentation".

on trouve tout d'abord un détecteur de vertex composé de microrubans de silicium puis une chambre à dérive et un solénoïde. Ces deux sous-détecteurs forment le détecteur central, immergé dans le champ magnétique de 1.4 T produit par le solénoïde. Immédiatement après le solénoïde se trouve une chambre à fil preshower (CPR), permettant d'identifier les conversions γe^+e^- ayant eu lieues dans le détecteur interne ou le solénoïde. Viennent ensuite le calorimètre électromagnétique (CEM) puis hadronique (CHA), segmentés en tours de dimensions $\Delta\eta \times \Delta\phi \approx 0.1 \times 0.26$. Le CEM se compose de plusieurs couches de scintillateurs intercalées entre des couches de plomb. Une chambre proportionnelle à fil (CES) est instalée près du maximum de la gerbe électromagnétique. Elle permet de déterminer plus précisément la position de la gerbe ainsi que de mesurer son profil latéral. La résolution en énergie du CEM est donnée par $\sigma(E)/E = 13.5\%/\sqrt{E \sin\theta}$ (avec E en GeV) et la résolution spatiale du CES vaut ± 2 mm at 50 GeV.

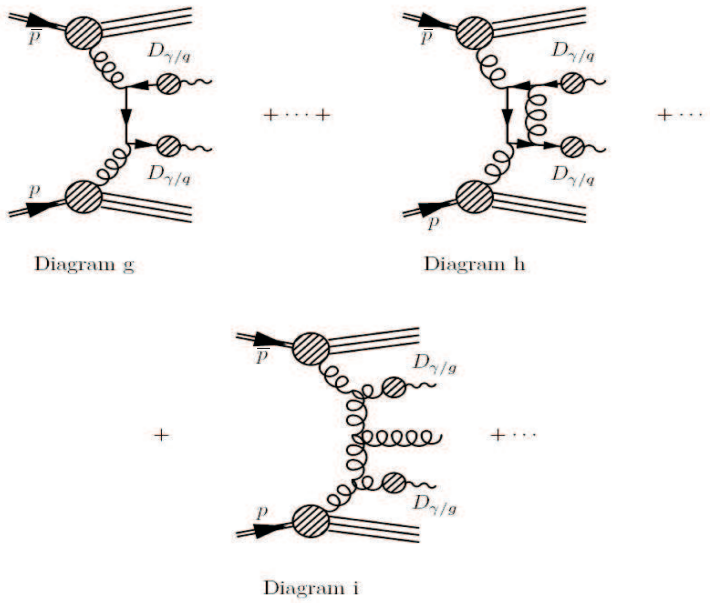

Figure 1.3: Exemple de diagrammes où les deux photons finaux sont issus de la fragmentation de partons. Ces contribution sont appellées “two-fragmentation”.

1.3 La mesure de la section efficace de deux photons

1.3.1 La sélection des candidats

Cette analyse est basée sur des événements récoltés par un trigger qui exige au moins deux objets électromagnétiques (EM) ayant chacun une énergie transverse, E_T, supérieure à 12 GeV. Des critères plus stricts sont appliqués durant l'analyse offline. L'énergie transverse du photon le plus énergétique doit être plus grande que 14 GeV. Afin d'éviter la région cinématique où le calcul NLO QCD peut devenir instable à cause de l'annihilation imparfaite des divergences réelles et virtuelles des gluons, l'énergie de l'autre photon doit être supérieure à 13 GeV. La pseudorapidité des photons doit se situer dans l'intervalle $|\eta| < 0.9$, afin d'exclure les régions proches des bords du CES et garantir la qualité de l'indentification des photons. De plus, la distance selon l'axe z entre la position du vertex reconstruit et le centre du détecteur (z-vertex) doit être plus petite que 60 cm. Le rapport entre l'énergie mesurée par le

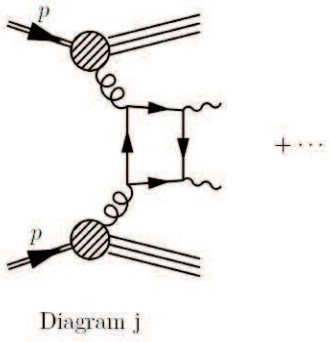

Figure 1.4: Le diagramme de boîte $gg \to \gamma\gamma$: deux gluons initiaux produisant deux photons finaux via une boucle de quarks.

calorimètre hadronique et électromagnétique (Had/EM) doit être inférieure à 0.055 + 0.00045×E, où E désigne l'énergie électromagnétique mesurée en GeV. L'isolation doit être inférieure à 1 GeV. Cette dernière est définie par l'énergie électromagnétique autre que celle du photon contenue dans un cône de rayon R=0.4 dans le plan $\eta - \phi$ autour de la direction du photon. Les candidats associés à des traces sont rejetés. Le profil latéral de gerbes électromagnétiques mesuré dans le CES est comparé à celui d'électrons mesurés lors de faisceaux tests. Le χ^2 de la comparaison (CES χ^2) doit être inférieur à 20. Finalement, les candidats photon associés aux plusieurs gerbes dans le CES supérieur à 1 GeVsont également éliminés. L'efficacité de ces différents critères de sélection, évaluée en utilisant une combinaison de données et de Monte Carlo PYTHIA, est donnée dans Tableau 1.1. L'efficacité du trigger pour détecter un seul photon, déterminé à l'aide d'un trigger de photon inclusif, vaut approximativement 80% à 13 GeVet dépasse 99% pour des photons d'énergie supérieur à 15 GeV. L'efficacité totale, comprenant l'efficacité de sélection et du trigger, vaut 15.2%.

Un total de 889 événements est obtenu après avoir appliqué les différents critères de sélection.

1.3.2 Soustraction du bruit de fond.

Cet échantillon contient encore la contamination de mesons neutres qui se désintègrent en plusieurs photons, tels que le π^0 ou η. Pour estimer ce bruit de fond, une méthode

Efficacité du trigger	0.951
Efficacité de reconstruction et coupes fiducielles	0.423
Critère d'isolation énergétique	0.727
Aucune trace associée à la gerbe EM	0.699
Aucun dépôt d'énergie additionnel > 1 GeVdans le CES	0.899
χ^2 du CES < 20	0.970
Rapport Had/EM $< 0.055 + 0.00045 \times$E/GeV	0.976
$\mid$ z-vertex $\mid < 60$ cm	0.877
Total	0.152

Table 1.1: L'efficacité des différents critères de sélection.

statistique basée sur l'analyse de la forme des gerbes EM produites par des photons directs ou issus de mesons a été appliquée. Pour les photons ou mesons qui ont une énergie transverse plus petite que 35 GeV, la fraction de photons directs contenus dans l'échantillon est estimée à partir du CES χ^2 . Lorsque les mesons ont une énergie transverse supérieure à 35 GeV, les photons qu'ils émettent en se désintégrant sont quasiment collinéaires et la gerbe EM qu'ils créent n'est plus distinguable de celle produite par un seul photon. Le CPR est alors utilisé pour déterminer le bruit de fond dans cette région. En effet, la probabilité qu'un photon se convertisse en une paire e^+e^- dans le détecteurs intérieurs ou le solénoïde (1.1 longueur de radiation) et laisse un signal dans le CPR est plus grande pour les photons issus de mesons que les photon directs.

Nous examinons les photon candidats si le CES $\chi^2 <4$ quand $E_T < 35$ GeV(région de basse E_T) ou si la charge mesurée par le CPR est inférieure à 500 fC quand $E_T > 35$ GeV(région de haute E_T). Chaque événement est ensuite réparti dans une de ces quatre catégories: le deux candidats sont des photons, le premier candidat est un photon et le second un meson, le premier candidat est un meson et le second un photon ou les deux sont des mesons. Conaissant l'efficacité pour qu'un vrai photon soit reconnu comme photon ou meson et celle pour un meson soit identifié comme un photon ou meson, il est possible de d'éterminer le véritable nombre dévenements $\gamma\gamma$ dans les données (ainsi que le nombre de photon-bruit de fond et bruit de fond-bruit de fond).

1.3.3 Sections efficaces

Les sections efficaces sont calculées à l'aide de la formule suivante:

$$d\sigma/dX = N_{\gamma\gamma}/(L \times \Delta X \times \varepsilon_{tot}) \tag{1.2}$$

où X désigne la varible cinématique qui nous intéresse, $N_{\gamma\gamma}$ le nombre d'événements $\gamma\gamma$ dans un bin, ΔX la taille du bin, $\mathcal{L}$ la luminosité intégrée, et ε_{tot} l'éfficacité de la sélection. La distribution de la section efficace en fonction de la masse $\gamma\gamma$, $M_{\gamma\gamma}$, se trouve dans la Figure 1.5 avec les prévisions de DIPHOX, ResBos et PYTHIA [37]. Les prévisions de PYTHIA ont été multipliées par un facteur 2 par rapport à la section efficace totale mesurée. La distribution de la variable q_T est montrée sur la Figure 1.6 et celle de l'angle entre les deux photons, $\Delta\phi$, sur la Figure 1.7. Les barres d'erreur internes indiquent l'erreur statistique seulement, les barres entières l'erreur statistique et systématique. Les points sont placés au milieu de chaque bins.

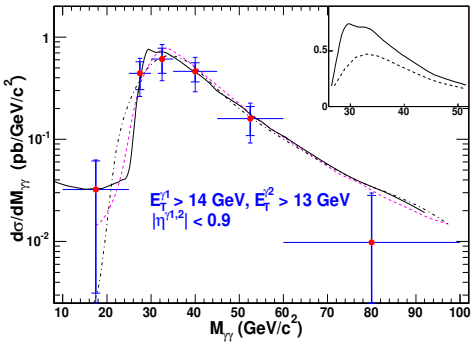

Figure 1.5: La distribution de masse invariante $\gamma\gamma$, $M_{\gamma\gamma}$, pour les données avec les prédictions de DIPHOX (trait plein), ResBos (traitillé), et PYTHIA (point et trait). Les prédictions de PYTHIA ont été multipliées par un facteur 2. L'encart montre (échelle linéaire) la section efficace NLO prédite par DIPHOX avec (trait plein) et sans (traitillé) la contribution gg.

La section efficace en fonction de ces variable sont données dans les Tableaux 1.2, 1.3 et 1.4.

Commençons d'abord par quelques commentaires sur les différentes prédictions théoriques.

$M_{\gamma\gamma}$ (GeV)	Données (pb/GeV)	DIPHOX (pb/GeV)	ResBos (pb/GeV)	PYTHIA (pb/GeV)
10-25	$0.03 \pm 0.03 \pm 0.01$	0.04	0.01	0.01
25-30	$0.44 \pm 0.13 \pm 0.12$	0.41	0.31	0.18
30-35	$0.61 \pm 0.17 \pm 0.16$	0.70	0.65	0.38
35-45	$0.46 \pm 0.10 \pm 0.14$	0.46	0.43	0.24
45-60	$0.16 \pm 0.05 \pm 0.04$	0.19	0.16	0.09
60-100	$0.01 \pm 0.02 \pm 0.01$	0.04	0.04	0.02

Table 1.2: Section efficace en fonction de la masse invariante $\gamma\gamma$ pour les données et les prédictions de DIPHOX, ResBos et PYTHIA.

q_T (GeV)	Données (pb/GeV)	DIPHOX (pb/GeV)	ResBos (pb/GeV)	PYTHIA (pb/GeV)
0-1	$0.70 \pm 0.30 \pm 0.14$	-2.45	0.34	0.53
1-2	$1.18 \pm 0.43 \pm 0.28$	5.59	0.95	1.15
2-4	$0.92 \pm 0.35 \pm 0.28$	2.06	1.03	0.94
4-8	$0.96 \pm 0.23 \pm 0.32$	1.17	0.94	0.46
8-12	$0.29 \pm 0.21 \pm 0.13$	0.44	0.59	0.21
12-16	$0.42 \pm 0.14 \pm 0.12$	0.24	0.36	0.12
16-24	$0.19 \pm 0.09 \pm 0.05$	0.13	0.19	0.07
24-32	$0.12 \pm 0.06 \pm 0.03$	0.09	0.07	0.03
32-40	$0.10 \pm 0.05 \pm 0.05$	0.06	0.03	0.01

Table 1.3: Section efficace en fonction de q_T pour les données et les prédictions de DIPHOX, ResBos et PYTHIA.

$\Delta\phi$ (rad)	CDF Données (pb/rad)	DIPHOX (pb/rad)	ResBos (pb/rad)	PYTHIA (pb/rad)
0.0-0.2	$1.06 \pm 0.52 \pm 0.34$	0.69	0.01	0.02
0.2-0.4	$0.89 \pm 0.52 \pm 0.32$	0.56	0.23	0.09
0.4-0.6	$0.51 \pm 0.63 \pm 0.19$	0.71	0.73	0.44
0.6-0.8	$3.34 \pm 1.10 \pm 1.04$	1.83	3.08	1.09
0.8-1.0	$15.56 \pm 2.59 \pm 4.70$	23.37	17.52	10.68

Table 1.4: Section efficace en fonction de $\Delta\phi$ pour les données et les prédictions de DIPHOX, ResBos et PYTHIA.

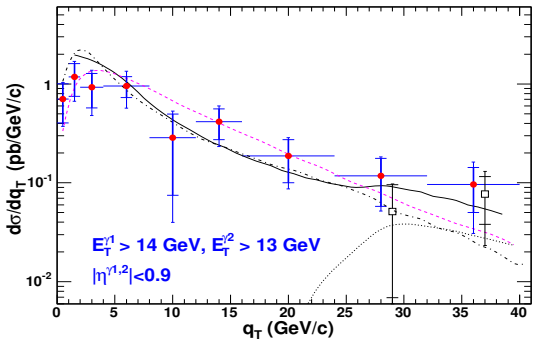

Figure 1.6: La distribution de l'impulsion transverse du système des deux photons, q_T, pour les données (ronds pleins) avec des prédiction de DIPHOX (trait plein), ResBos (traitillé), et PYTHIA (point et trait). Les prédictions de PYTHIA ont été multipliées par un facteur 2. Les résultats pour les données (ronds vides) et les prédictions de DIPHOX (pointillés) lorsque $\Delta\phi < \pi/2$ sont visibles pour $q_T > 20$ GeV.

- Les sections efficaces en fonction de $M_{\gamma\gamma}$ obtenues par les différents calculs sont en assez bon accord les unes avec les autres, excepté à basse masses où DIPHOX prédit une plus grande section efficace que ResBos ou PYTHIA. On constate également, comme le monte l'encart de la Figure 1.5, que le processus gg fournit la plus grande contribution à la section efficace à basse masse. Cette contribution diminue rapidement lorsque la masse augmente. La production de deux photons dans les collisions proton-antiproton au Tevatron permet en outre d'étudier la réaction $gg \to \gamma\gamma$ et de mieux connaître la distribution de densité de gluons dans le proton à petit x et grand Q^2.

- La section efficace en fonction de q_T prédite par ResBos est lisse sur tout l'intervalle de q_T tandis que les prédictions de DIPHOX deviennent instable à bas q_T, et ce à cause des singularités qui apparaissent dans le calcul pour un ordre fixé. A haut q_T, DIPHOX présente une épaule, effet absent des prédictions de ResBos.

- Les prédictions de ResBos sont supérieures à celles de DIPHOX pour $\Delta\phi > \pi/2$ mais significativement inférieures à petit $\Delta\phi$.

Les différence entre les prédictions de ResBos et DIPHOX sont tout de même

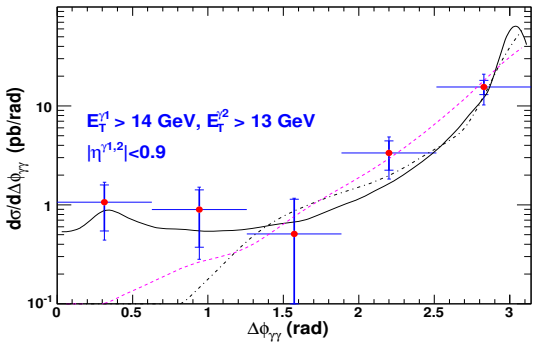

Figure 1.7: La distribution de l'angle entre les deux photons $\Delta\phi$ pour les données (rond pleins) avec des prédictions de DIPHOX (trait plein), ResBos (traitillé), et PYTHIA (point et trait). Les prédictions de PYTHIA ont été multipliées par un facteur 2.

prévisibles. En effet, les contributions de fragmentation ne sont calculées qu'au premier ordre pour ResBos. Nous avons vu précédemment que la probabilité qu'un quark produise un photon est d'ordre $\alpha_{em}\alpha_s$. Certains processus de type $2 \rightarrow 3$ où le quark final produit un deuxième photon, tel que $qg \rightarrow gq\gamma\gamma$, sont ainsi d'ordre $\alpha_{em}^2\alpha_s$. Ces contribtuions d'ordre NLO sont incluses dans DIPHOX mais absentes de ResBos, ce qui a pour effet de sous-estimer le taux de production à haut q_T, à bas $\Delta\phi$ et à basse masse $\gamma\gamma$.

Abordons maintenant la comparaison entre les données et les diverses prédictions. La section efficace mesurée en fonction de la masse $\gamma\gamma$ est en assez bon accord avec les différentes prédictions. Dans le premier bin de masse, DIPHOX semble mieux reproduire les données que ResBos ou PYTHIA, mais les erreurs statistiques sont trop importantes pour en tirer une conclusion ferme. A bas et moyen q_T, ainsi que pour $\Delta\phi > \pi/2$, les données sont mieux reproduites par ResBos que DIPHOX. C'est dans ces régions que les effets dus aux émissions de gluons sont importants. A l'inverse, DIPHOX est meilleur à grand q_T et $\Delta\phi < \pi/2$, là où la contributions des processus de fragmentation $2 \rightarrow 3$ est élevée. On constate finalement que PYTHIA reproduit raisonnablement bien la forme des données. Une statistique plus grande serait évidemment nécessaire pour obtenir des conclusions plus précises.

Part I

Theoretical Introduction

Chapter 2

The Standard Model of Particle Physics

2.1 Physics

I do not know what I may appear to the world
but to myself I seem to have been only like a boy
playing on the seashore, and diverting myself
in now and then finding a smoother pebble
or a prettier shell than ordinary,
whilst the great ocean of truth
lay all undiscovered before me.
SIR ISACC NEWTON
Brewster's Memories of Newton, Vol II, Chap. XXVII

Physics is the science that deals with matter and energy, their properties, and their interactions.

My understanding of the purpose the field and research attitude are the best elaborated as follows:

" The physicist looks for a structure which will enable him to **make an orderly model of a chaotic universe.** In principle, it should eventually become possible to extend the methods of physics to all fields of knowledge, but in practice this

still appears to be somewhat ambitious. For one thing there are difficulties with the mathematics in handling complex systems. For another some important links are still missing. But the objective is to **achieve actual understanding**, not just a collection of facts. To accomplish this physicists have to go wherever their travels take them. It is impossible to predict all the social implications of fundamental research. Columbus did not anticipate that he would discover a continent. He set out to test a theory and to find a new path to the Orient. **The important thing is that he went.**" [1]

2.2 The Standard Model of Particle Physics

The aim of particle physics is to understand the basic constituents of matter and their interactions. According to our present knowledge, the basic consistuents of the matter are leptons and quarks (and their anti-particle partners). They interact through 4 fundamental forces:

1. Gravity
2. the weak interaction
3. the electromagnetic interaction
4. the strong interaction

So far, the most successful theory to model the strong, weak and electromagnetic interactions is the"Standard Model"(SM).

Gravity is the weakest interaction up to the presently accessible energy scales. It is the best described by Einstein's General Relativity theory, as a quantized theory has not yet been formulated. This interaction is not incorporated in the SM.

The weak and electromagnetic interactions are unified in the SM by the electroweak sector. The strong interaction is the interaction among quarks, modelled by Quantum Chromodynamics (QCD) in the SM.

The principal idea of the SM is reviewed in the successive sections.

The Standard Model is a Quantum Field Theory (QFT) [1], which describes the strong, weak and electromagnetic interactions of quarks and leptons. The gauge group of the standard model is

$$G_{SM} = SU(3) \times SU(2)_L \times U(1)_Y, \tag{2.1}$$

where $SU(3)$ is the gauge group of QCD (group of the color) and $SU(2)_L \times U(1)_Y$, including $U(1)_{em}$, is the gauge group that unifies the weak and electromagnetic interactions into electroweak theory. The coupling constants for the gauge groups $SU(3)$, $SU(2)_L$ and $U(1)_Y$ are g_s, g and $g\prime$ respectively. The $SU(3) \times U(1)_{em}$ symmetries are exact, while the $SU(2)_L \times U(1)_Y$ symmetries are spontaneously broken by the Higgs mechanism to generate the masses of $W^{\pm}$ and Z^0.

2.2.1 Gauge bosons

The Lie algebra of the $SU(3)$ group has 8 generators. In the 3-dimensional representation, the 8 generators are 3×3 hermitian matrices with zero trace : $T^A_{\mathbf{3}} = 1/2\lambda^A, A = 1, \ldots, 8$, with λ^A the Gell-Mann matrices. The generators satisfy the relations $[T^A_{\mathbf{3}}, T^B_{\mathbf{3}}] = if^{ABC}T^C_{\mathbf{3}}$, and $Tr(T^A_{\mathbf{3}}T^B_{\mathbf{3}}) = 1/2\delta^{AB}$, where f^{ABC}, the structure constants of $SU(3)$, are real numbers. Each generator is to be associated with a gauge field. So, there are 8 gauge bosons from the $SU(3)$ symmetry of Standard Model : $A^B_\mu, B = 1, \ldots, 8$(gluons).

Similarly, 2-dimensional representation of $SU(2)$ has 3 generators : $T^a_{\mathbf{2}} = 1/2\sigma^a, a = 1, 2, 3$, with σ^a the Pauli matrices, corresponding to 3 gauge bosons $W^a_\mu, a = 1, 2, 3$. Finally with the gauge field for $U(1)_Y$ local symmetry B_μ, there are altogether 12 gauge bosons in the Standard Model, among which the four bosons $W^a_\mu, (a = 1, 2, 3)$ and B_μ generate $W^{\pm}$, Z^0 and the photon after the spontaneous gauge symmetry breaking.

[1] Among many existing literatures on the subject, the textbooks on QFT by J-P Derendinger [2], C. Itzykson & J-B Zuber [3] are my favorite, and heavily used for the theoretic discussions in this thesis. The convention of mathematical notations in Appendix A of Ref. [2] is adopted.

2.2.2 Leptons and Quarks

Leptons and quarks (and their anti-particle partners) are the basic constituents of matter. In the SM, they are described by spinor fields. They have spin 1/2, and obey Fermi-Dirac statistics. Leptons and quarks can be classified by their gauge transformations (or, in other words, their couplings with the gauge bosons).

1. Quarks (and anti-quarks) are color-triplets, and participate in strong interactions.

2. Leptons (and anti-leptons) are color-singlets, and don't participate in strong interactions.

Left-handed fermions (leptons, quarks and their anti-particle partners) are doublets of $SU(2)_L$, and participate in weak interactions. Right-handed fermions are $SU(2)_L$ singlets, and do not participate in weak interactions. In the SM, right-handed neutrinos do not interact with any of the three forces, which is the reason they can be eliminated from the model – in fact the minimal standard model does not include right-handed neutrinos.

Although not predicted by the theory itself, observations so far suggest that there are 3 generations of fermions. The $SU(3)$, $SU(2)_L$, and $U(1)_Y$ quantum numbers of fermions are repeated 3 times in Nature! One can enumerate the fermions of each generation in minimal standard model as the following :

- Quarks : Left-handed quarks form $SU(2)_L$ doublets : $\binom{U}{D}_L$. Right-handed quarks are $SU(2)_L$ singlets : U_R, D_R. The number of quarks are tripled due to the quantum number (color) of $SU(3)$. So there are $(2+2) \times 3 \times 2 = 24$ quarks in each generation, where the last $\times 2$ is to count the corresponding anti-quarks.

- Leptons : Left-handed leptons are $SU(2)_L$ doublets : $\binom{E}{\nu}_L$. The only right-handed $SU(2)$ singlet is E_R, because the right-handed neutrinos are omitted in the model. So, there are $(2+1) \times 2 = 6$ leptons in each generation, taking the anti-particles into account.

To date, the existence of leptons and quarks in the three generations have been verified from experimental data. Some of their properties have also been studied over time. The masses and charges of leptons and quarks are listed in Table 2.1 and Table 2.2 respectively. Two remarks can be made here :

a) The confinement hypothesis assumes that only color singlet states can be observed in nature – there are no underlying restrictions from theory. States of fractional charge have never been observed. Quarks form themselves into bound states called mesons and baryons with strong interactions. This process is called *hadronization*.

b) The mass eigen-states of down-type quarks mix to form eigen-states of weak interactions.

$$\begin{pmatrix} d\prime \\ s\prime \\ b\prime \end{pmatrix} = \begin{pmatrix} V_{ud} & V_{us} & V_{ub} \\ V_{cd} & V_{cs} & V_{cb} \\ V_{td} & V_{ts} & V_{tb} \end{pmatrix} \begin{pmatrix} d \\ s \\ b \end{pmatrix} \tag{2.2}$$

The 3x3 matrix is called the Cabibbo-Kobayshi-Maskawa matrix. It is unitary, and has 4 free parameters : three angles and one phase. The parameterization can be found in Ref. [4].

Generation	Lepton	Mass(MeV/c^2)	charge
1	e	0.511	-1
	ν_e	$< 3 \times 10^{-6}$	0
2	μ	105.6	-1
	ν_μ	$< 0.19(CL = 90\%)$	0
3	τ	1777.0	-1
	ν_τ	$< 18.2(CL = 95\%)$	0

Table 2.1: Leptons in the Standard Model [5]

2.2.3 Scalar fields and Higgs Mechanism

Introducing explicit mass terms of gauge bosons and fermions breaks the gauge invariance of the Lagrangian, which makes the theory nonrenormalizable. However, a

Generation	Quark	Mass	charge
1	$up(u)$	$1-5MeV/c^2$	+2/3
	$down(d)$	$3-9MeV/c^2$	-1/3
2	$charm(c)$	$1.15-1.35GeV/c^2$	+2/3
	$strange(s)$	$75-170MeV/c^2$	-1/3
3	$top(t)$	$174.3\pm5.1GeV/c^2$	+2/3
	$bottom(b)$	$4.0-4.4GeV/c^2$	-1/3

Table 2.2: Quarks in the Standard Model [5]

theory with massless fermions and gauge bosons obviously deviates from the experimental observations. The SM utilizes the Higgs mechanism [6] to break the gauge symmetries. The idea is to introduce scalar fields to the theory, which keep the Lagrangian gauge invariant while break the symmetries of the vacuum expectation. The SM uses a doublet of complex scalar fields : $H^\alpha, \alpha = 1, 2$. The gauge transformations of the scalar fields are as the following:

- $SU(3) : \delta H^\alpha = 0, \alpha = 1, 2$
- $SU(2)_L : \delta H^\alpha = i\omega(T_{\mathbf{2}})^\alpha_\beta H^\beta, \alpha = 1, 2$
- $U(1)_Y : \delta H^\alpha = -1/2 i\omega H^\alpha, \alpha = 1, 2$

It is useful to define

$$H = \begin{pmatrix} H^1 \\ H^2 \end{pmatrix}. \tag{2.3}$$

The quantity $H^\dagger H$ is invariant under $SU(3) \times SU(2)_L \times U(1)_Y$ transformations. This is useful for constructing the Lagrangian of the scalar fields. In fact, the scalar potential of the SM is

$$V(H, H^\dagger) = -\mu^2(H^\dagger H) + \lambda/2(H^\dagger H)^2, \tag{2.4}$$

where μ^2 and λ are real and positive numbers.

The potential of vacuum is minimized when

$$\langle 0|H^\dagger H|0\rangle = \mu^2/\lambda. \tag{2.5}$$

The condition is invariant under gauge transformations. It is possible to choose a gauge, such that

$$\langle 0|H|0\rangle = \frac{1}{\sqrt{2}}\begin{pmatrix} v \\ 0 \end{pmatrix}, v = \sqrt{\frac{2\mu^2}{\lambda}}. \tag{2.6}$$

This gauge choice is called "unitary gauge".

The physical vacuum is the state with the least energy. By introducing the scalar potential, the vacuum expectation value have continuous minima (Eq. 2.5). One can choose the unitary gauge to define the physical vacuum Eq. 2.6. The Lagrangian in terms of the displacement of the physical vacuum is no longer gauge invariant.

One can verify that

$$exp(i\omega[T^3_{\mathbf{2}} + Y])\langle 0|H|0\rangle = \langle 0|H|0\rangle. \tag{2.7}$$

The $U(1)_Q$ symmetry, generated by $Q = T^3_{\mathbf{2}} + Y$ is conserved. The other three symmetries of $SU(2)_L \times U(1)_Y$ are spontaneously broken. Goldstone's theorem states that one massless spin 0 boson, called *Goldstone boson* is created for each spontaneously broken continuous symmetry. The four real components of H split into 3 Goldstone bosons and 1 massive Higgs boson. In the unitary gauge, the scalar doublet H becomes

$$H_{unit.} = \frac{1}{\sqrt{2}}\begin{pmatrix} h(x) + v \\ 0 \end{pmatrix}, v = \sqrt{\frac{2\mu^2}{\lambda}}, \tag{2.8}$$

where $h(x)$ is a physical real scalar field in the theory. After redefining the gauge fields as:

$$\begin{cases} W^+_\mu = \frac{1}{\sqrt{2}}(W^1_\mu - iW^2_\mu) \\ W^-_\mu = \frac{1}{\sqrt{2}}(W^1_\mu + iW^2_\mu) \\ Z_\mu = \cos\theta_W W^3_\mu - \sin\theta_W B_\mu \\ A_\mu = \sin\theta_W W^3_\mu + \cos\theta_W B_\mu \end{cases}$$

where θ_W (Weinberg angle) is defined by

$$\cos\theta_W = \frac{g}{\sqrt{g^2+g\prime^2}}, \sin\theta_W = \frac{g\prime}{\sqrt{g^2+g\prime^2}}, \tag{2.9}$$

the SM Lagrangian (with unitary gauge defined in Eq. 2.6) that describes the electroweak bosons becomes:

$$\begin{aligned}\mathcal{L}_{unit.} = &-\tfrac{1}{4}A_{\mu\nu}A^{\mu\nu} - \tfrac{1}{4}Z_{\mu\nu}Z^{\mu\nu} - \tfrac{1}{4}W^+_{\mu\nu}W^{-\mu\nu} \\ &+\tfrac{1}{2}\tfrac{g^2+g\prime^2}{4}v^2Z_\mu Z^\mu + \tfrac{g^2}{4}v^2W^+_\mu W^-_\mu \\ &+\tfrac{1}{2}(\partial_\mu h)(\partial^\mu h) - \mu^2h^2 - \sqrt{\tfrac{\lambda}{2}}\mu h^3 - \tfrac{\lambda}{8}h^4 + \tfrac{\mu^4}{2\lambda} \\ &+...,\end{aligned} \tag{2.10}$$

where

$$\begin{aligned}A_{\mu\nu} \equiv \partial_\mu A_\nu - \partial_\nu A_\mu, \qquad Z_{\mu\nu} \equiv \partial_\mu Z_\nu - \partial_\nu Z_\mu, \\ W^+_{\mu\nu} \equiv \partial_\mu W^+_\nu - \partial_\nu W^+_\mu, \quad W^-_{\mu\nu} \equiv \partial_\mu W^-_\nu - \partial_\nu W^-_\mu.\end{aligned} \tag{2.11}$$

Some interactions terms are omitted for brevity. The theory now describes :

- A massless gauge field A_μ, the photon field.
- A spin 1 field and its conjugation : W^-_μ and W^+_μ, with mass $M_W = \frac{gv}{2}$.
- A field Z_μ, with mass $M_Z = \frac{1}{2}\sqrt{g^2+g\prime^2} = M_W/\cos(\theta_W)$.
- A real scalar field h(x), the unique Higgs boson in the theory, with mass $m_h = \sqrt{2\mu^2}$.

The mass terms for the fermions are introduced to the SM by the fermion-Higgs boson interactions (Yukawa interactions).

2.2.4 Parameters in the Standard Model

There are 18 free parameters in the Standard Model.

- Three coupling constants of the three gauge groups: g_s, g and $g\prime$. The most frequently used forms are

$$\alpha_s = \frac{g_s^2}{4\pi} \qquad (strong\ coupling\ constant)$$

$$\sin\theta_W = \frac{g\prime}{g^2 + g\prime^2} \qquad (\theta_W : Weinberge\ angle)$$

$$\alpha_{em} = \frac{e^2}{4\pi}, e = g\sin\theta_W \qquad (fine\ structure\ constant).$$

- Mass of $W^{\pm}$ boson, or equivalently, Fermi constant G_F. At the lowest order of perturbation theory,
$$\frac{g^2}{8M_W^2} = \frac{1}{2v^2} = \frac{1}{\sqrt{2}}G_F \tag{2.12}$$
- Nine masses of quarks (u, d, s, c, b, t) and leptons (e, μ, τ).
- Four parameters for the Cabibbo-Kobayashi-Maskawa matrix.
- Mass of Higgs boson.

Chapter 3

Perturbation theory and diphoton production

An overview of the Standard Model is given in the previous chapter. In this chapter, the method of perturbation theory and Feynman diagrams will be briefly introduced and important contributing processes for diphoton production will be discussed in some detail.

3.1 Perturbation theory

Collider experiments have become the principal experimental method of high-energy physics research. At colliders, particles are accelerated and collided against each other. On a macroscopic scale, interaction times are extremely small. It is therefore impossible to follow in detail the time evolution during the scattering. We can only give the following picture based on the *asymptotic assumptions* : long before the collision, well-separated wave packets evolve independently and freely. The collision process then follows, involving scattering, absorption, or creation of new particles. Long after the collision, free wave-packets separate, representing the outgoing states. They are again described by free fields. For example, consider an interacting real

scalar field $\phi(x)$. The asymptotic assumptions are expressed as :

$$\begin{aligned} t = x_0 \to -\infty : \phi(x) \to Z^{1/2}\phi_{in}(x), \\ t = x_0 \to +\infty : \phi(x) \to Z^{1/2}\phi_{out}(x). \end{aligned} \tag{3.1}$$

where

- Z is a constant between 0 and 1, to account for the fact that the interacting field $\phi(x)$ may not conserve the number of particles;
- $\phi_{in}(x)$ denotes the free field of the initial state long before the collision;
- $\phi_{out}(x)$ denotes the free field of the final state long after the collision.

The amplitude $\langle b, out|a, in\rangle$ enable us to obtain the probability that an incoming state $|a\rangle$ will evolve in time and be measured in the $|b\rangle$ state. The calculation of elements $\langle out|in\rangle$ consists of two steps :

- To relate $\langle out|in\rangle$ in terms of generalized Green's function of the interacting fields from the asymptotic assumptions.
- To calculate the Green's function in perturbation theory.

The first step is called "reduction" [7]. For instance, the amplitude of $2 \to 2$ scattering of real scalar particles can be related to 4-point generalized Green's function:

$$\begin{aligned} \langle q_1, q_2; out|p_1, p_2; in\rangle &= (non - connected) \\ &+ (iZ^{-\frac{1}{2}})^4 \int d^4x_1 \int d^4x_2 \int d^4y_1 \int d^4y_2 e^{-ip_1x_1 - ip_2x_2 + iq_1y_1 + iq_2y_2} \\ &\quad ((\partial^\mu\partial_\mu)_{x_1} + m^2)((\partial^\mu\partial_\mu)_{x_2} + m^2)((\partial^\mu\partial_\mu)_{y_1} + m^2)((\partial^\mu\partial_\mu)_{y_2} + m^2) \\ &\quad \langle 0|T\phi(x_1)\phi(x_2)\phi(y_1)\phi(y_2)|0\rangle \end{aligned}$$

where $p1, p2$ $(q1, q2)$ denote the 4-momenta of the 2 scalar particles at initial (final) state; "non-connected" stands for the contribution where the two particles pass by each other without interacting; $\phi(x)$ is the field that describe the scalar particles; m is the mass of these scalar particles.

Suppose, the Lagrangian of the theory can be decomposed as a free part $\mathcal{L}_0$ and an interacting part $\mathcal{L}_I$:

$$\mathcal{L} = \mathcal{L}_0 + \mathcal{L}_I. \tag{3.2}$$

The Gell-Mann and Low formula expresses n-point Green's function of interacting fields in terms of free fields:

$$\begin{aligned} G(x_1, \cdots, x_n) &\equiv \langle 0|T\phi(x_1)\cdots\phi(x_n)|0\rangle \\ &= \frac{\langle 0|T\phi_{in}\cdots\phi_{in}(x_n)exp[i\int d^4x\mathcal{L}_{\mathcal{I}}]|0\rangle}{\langle 0|Texp[i\int d^4x\mathcal{L}_I]|0\rangle}. \end{aligned}$$

When the interaction is weak (i.e $\mathcal{L}_I$ is small), the numerator can be expanded as polynomial series of $\mathcal{L}_I$, and expansion terms up to finite order can give a good approximation of the interaction amplitude. After having applied Wick's theorem, the amplitude can be written as products of propagators of free fields and vertices factors, which can be visualized by connected lines and vertices (Feynman Diagrams).

Interactions are characterized by the effective coupling constants, of which, the values depend on the energy scale of the interactions.

At the scale of Z^0 boson mass (91.2 GeV), $\alpha_{em} \approx \alpha_{weak} \approx 1/128, \alpha_s \approx 0.12$; the coupling constants are sufficiently small so that the perturbation method works well for calculations of electromagnetic, weak and strong interactions.

3.2 Diphoton production in $p\overline{p}$ collisions

The high-energy interactions of hadrons are described by the QCD improved parton model [12]. In this model a hard scattering process between two hadrons is the result of an interaction between *partons* : the quark and gluons which are the constituents of the incoming hadrons. The incoming hadrons provide "broad-band" beams of partons which posses varying fractions of the momenta of their parent hadrons. The cross section for a hard scattering process initiated by two hadrons with four momenta $P1$

and $P2$ can be written as

$$\sigma(P1, P2) = \sum_{i,j} \int dx_1 dx_2 f_i(x_1, \mu^2) f_j(x_2, \mu^2) \hat{\sigma}_{ij}(p_1, p_2, \alpha_s(\mu^2), Q^2/\mu^2). \qquad (3.3)$$

The momenta of the partons which participate in the hard interaction are $p_1 = x_1 P_1$ and $p_2 = x_2 P_2$. The characteristic scale of the hard scattering is denoted by Q. The functions $f_i(x, \mu^2)$ are the quark or gluon distributions, defined at a factorization scale μ. The short-distance cross section for the scattering of partons of types i and j is denoted by $\hat{\sigma}_{ij}$. The *factorization scale* μ is an arbitrary parameter. It can be thought of as the scale which separates the long- and short-distance physics. Thus a parton emitted with a small transverse momentum (less than the scale μ), is considered part of the hadron structure and is absorbed into the parton distribution. A parton emitted at larger transverse momentum is part of the short-distance cross section. The scale μ should be chosen to be of the order of the hard scale Q which characterizes the parton-parton interaction. The parton-parton short-distance cross section $\hat{\sigma}_{ij}$ is typically given by perturbation calculations. The more terms included in the perturbative expansion, the weaker the dependence of $\sigma(P_1, P_2)$ on μ will be. [1]

In $p\bar{p}$ collisions, the leading order (LO, $\mathcal{O}(\alpha_{em}^2)$)contribution of diphoton production is from quark anti-quark annihilation ($q\overline{q} \to \gamma\gamma$), see Diagram a in Fig. 3.1.

The contributions from the subprocesses in which one or both of the photons come from the collinear fragmentation of a hard parton in the short distance subprocesses are of LO too. See for example Diagram d (in Fig. 3.2) and Diagram g (in Fig. 3.3).

The next-to-leading order (NLO, the order of $\alpha_{em}^2 \alpha_s$) contributions include subprocesses with real or virtual $\mathcal{O}(\alpha_s)$ corrections to the subprocesses discussed above.

The $gg \to \gamma\gamma$ (Fig. 3.4)process with gluon-gluon at initial state coupled to the $\gamma\gamma$ final state via a quark loop is beyond NLO; it is suppressed by $\mathcal{O}(\alpha_s^2)$. But the rate is large in the kinematic regions where the gluon density is high, such as low $\gamma\gamma$ invariant mass region.

[1] The parton distribution functions used in the cross section predictions should be compatible with the perturbation calculations, e.g, CTEQ and MRST pdf's are meant to be used with NLO programs [14].

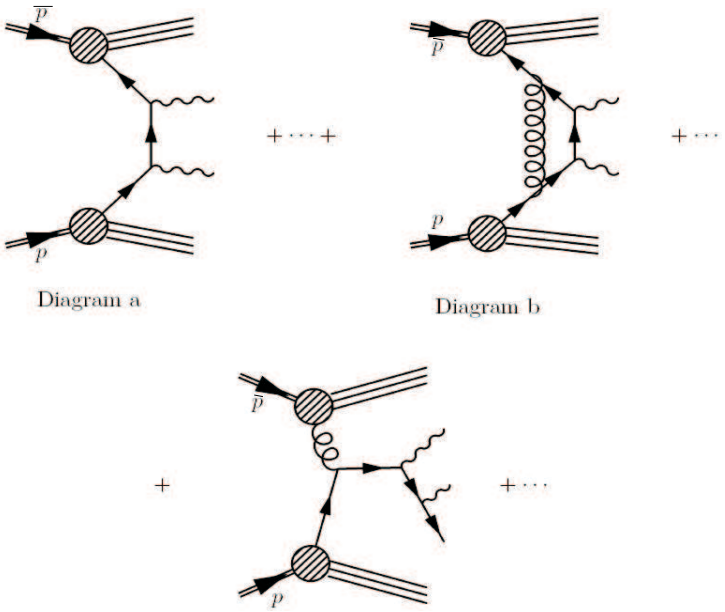

Figure 3.1: Examples of diagrams with the two photons at final state produced at hard-scattering : these contributions are called "two-direct".

DIPHOX [9] is fixed-order calculation that includes all the processes discussed above. ResBos [11] includes the processes where both photons are produced at hard-scattering to NLO accuracy, and processes involving the fragmentation contributions to LO. Moreover, ResBos resums the effects of multiple gluon emissions at initial state; this is particularly important for the study of variables that are sensitive to the soft momenta emissions at initial state. For example, the two-photon system transverse momentum (q_T) is a $\delta-$function at LO, and diverges as $q_T \to 0$ at NLO.

The differential cross sections as function of diphoton mass, the diphoton q_T, and the $\Delta\phi$ between the two photons are calculated with both DIPHOX and ResBos for comparison with the experimental results. The following kinematics cuts are imposed to the calculations and data analysis:

- $E_T^{\gamma 1} > 14$ GeV, $E_T^{\gamma 2} > 13$ GeV,
- $|\eta^{\gamma_{1,2}}| < 0.9$,

where $\gamma_{1(2)}$ denotes the harder(softer) photon at final state; E_T denotes the transverse

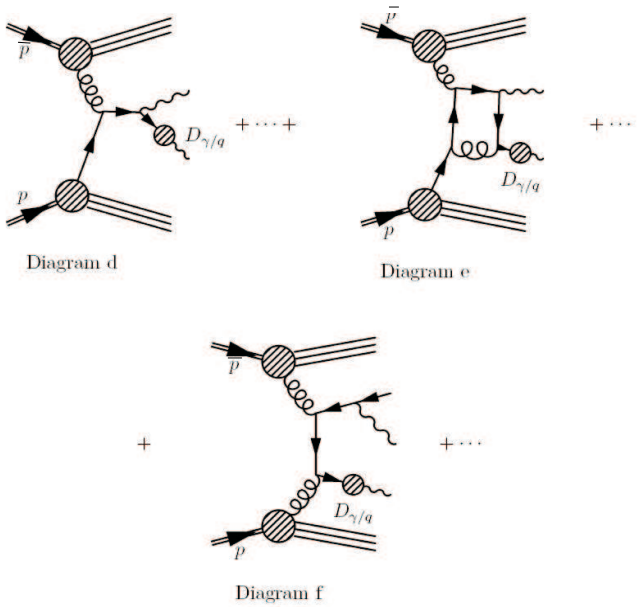

Figure 3.2: Examples of diagrams with one of the two photons at final state produced at fragmentation : these contributions are called "one-fragmentation".

energy; η denotes the pseudo-rapidity [2].

The minimum transverse energy requirements are different for the two photons in order to void producing critical kinematic regions where the cancellations between virtual and real soft/collinear gluon divergences become imperfect in fixed-order calculations.

Shown in Fig. 3.5, is the mass distribution predicted by DIPHOX, with a symmetric E_T cut. Note that the cross section drops to negative at mass = 26 GeV bin for the curve without $gg \to \gamma\gamma$ box contribution. With an asymmetric E_T cut, in Fig. 3.6, the cross section prediction does not go below zero for either case.

The $\gamma\gamma$ cross section is difficult to measure because of the background from neutral mesons such as π^0, η. The background is huge because essentially every jet contains one or more π^0s. *Isolation* cut is typically placed to reduce the huge background. The isolation of a photon is defined as the transverse energy (E_T) sum in the 0.4 cone in $\eta - \phi$ space around the photon, minus the photon E_T. The isolation of each photon is

[2]Both calculations use the same coordinate system as CDF does. The CDF coordinate system is described in Chapter 5.

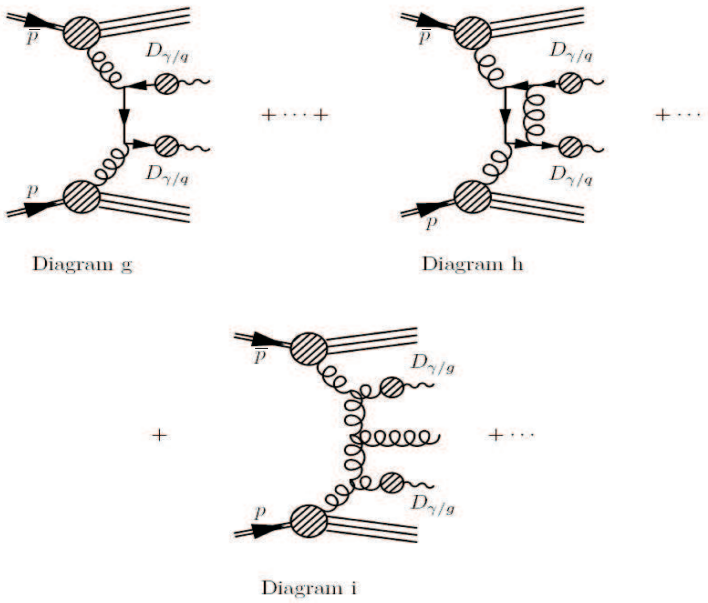

Figure 3.3: Examples of diagrams with both photons produced at fragmentation : these contributions are called "two-fragmentation".

required to be below 4 GeV in the DIPHOX calculation. It is found that this isolation criterion effectively removes the contributions where both photons are produced at fragmentation, while the contribution with one photon produced at fragmentation is visible. The 4 GeV isolation cut is to be compared with 1 GeV cut on data (see Chapter 6). The isolation cut in DIPHOX is varied from 1 GeV to 4 GeV; the looser isolation in the calculation has no significant impact on the numerical results, but makes the predictions more reliable [10].

The mass, q_T and $\Delta\phi$ from the DIPHOX and ResBos exhibit the following:

- The $\gamma\gamma$ invariant mass distributions are compared in Fig. 3.9. The invariant mass distributions agree pretty well for a large mass region. Except at very low mass, DIPHOX predicts much higher rates.

- The $\gamma\gamma$ q_T distributions are compared in Fig 3.10. The ResBos curve is smooth for the overall region, while DIPHOX curve appears unstable at low q_T. The singularity at $q_T \to 0$ has been explained earlier. The divergence at $q_T = 4$ GeV is from the isolation cut implemented in DIPHOX. The isolation cut in

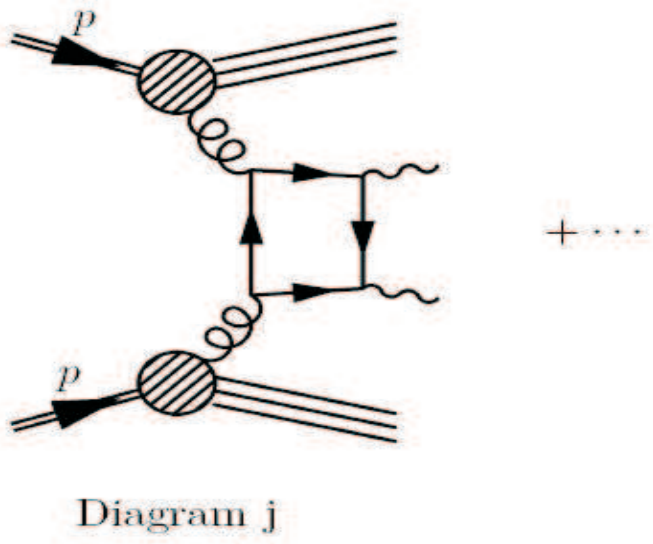

Figure 3.4: The "box" diagram : the gluon-gluon at initial state coupled to $\gamma\gamma$ via a quark loop. This process is at order of $\alpha_{em}^2\alpha_s^2$, but the rate is still appreciable at some kinematic regions because of the high gluon density at low x.

DIPHOX is at the parton level : defined as the sum of the transverse energies of partons in 0.4 cone around the photon. For the one fragmentation contribution, which has a photon balanced against a jet at the final state, with the second photon embedded in the jet (Fig. 3.7), the isolation of the photon inside the jet is equal to the two-photon q_T.

The isolation cut at 4 GeV makes the q_T distribution of this contribution a step function at LO. The step function is convoluted with the probability of one gluon emission at NLO. The convolution is divergent.

Another feature from the comparison is that at the high end, DIPHOX curve is enhanced, while ResBos is not. This region corresponds mostly to the phase space where the two photons are about collinear. The difference is expected: as noted earlier, the fragmentation contribution in ResBos is effectively at LO. Since fragmentation to a photon is effectively of order α_{em}/α_s, some 2→3 processes like qg→gqγ, with the quark in the final state fragments to a second

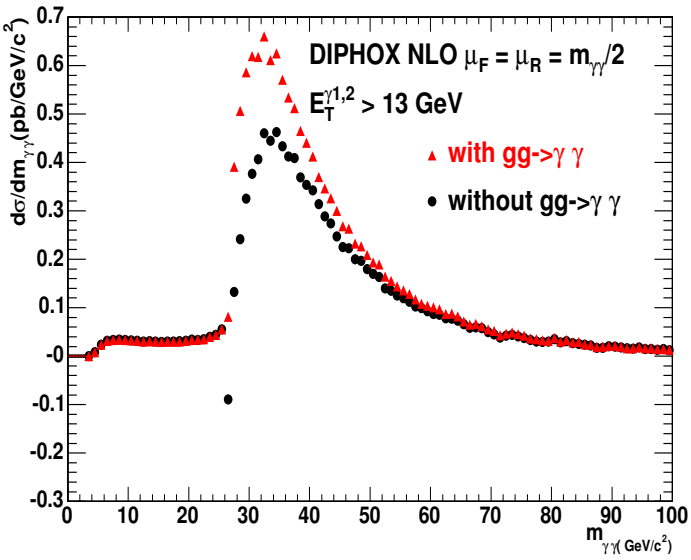

Figure 3.5: Invariant mass distributions by DIPHOX NLO predictions. The box contribution is negligible at high mass region. But the calculated cross section is negative at the 26 GeV bin in the prediction without box contribution, because the cancellation of divergences from real and virtual soft/collinear gluon emissions becomes imperfect with the symmetric cuts.

photon (see Fig. 3.8) are effectively of order $\alpha_{em}^2 \alpha_s$. This contribution is not in ResBos yet, which makes it underestimate the production rate at high q_T. In fact, the enhancement from fragmentation contributions has been observed before [48].

- The $\Delta\phi$ distributions are compared in Fig 3.11; for exactly the same reason explained above, ResBos underestimates the cross section at small $\Delta\phi$ due to the absence of 2→3 fragmentation contributions. This also explains the fact ResBos underestimates the rate at small diphoton mass for the given set of kinematics cuts.

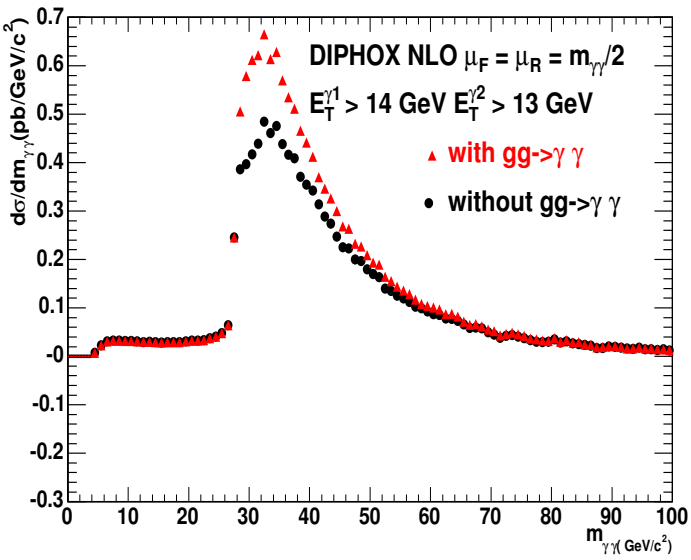

Figure 3.6: Invariant mass distributions by DIPHOX NLO predictions. No singular point on either of the two curves, with the asymmetric E_T cut. The prediction is more reliable with asymmetric cuts, and we adopt the asymmetric E_T cut for data/theory comparisons.

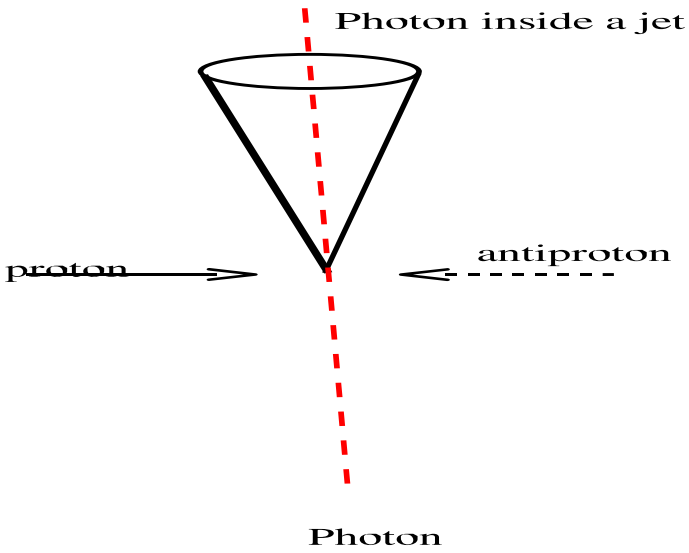

Figure 3.7: The final state of "one-fragmentation" contribution : a photon balanced against a jet, within which embeded another photon. For this configuration, the q_T of the two photons is equal to the isolation of the photon insided the jet. The isolation cut makes q_T distribution a step function for this contribution.

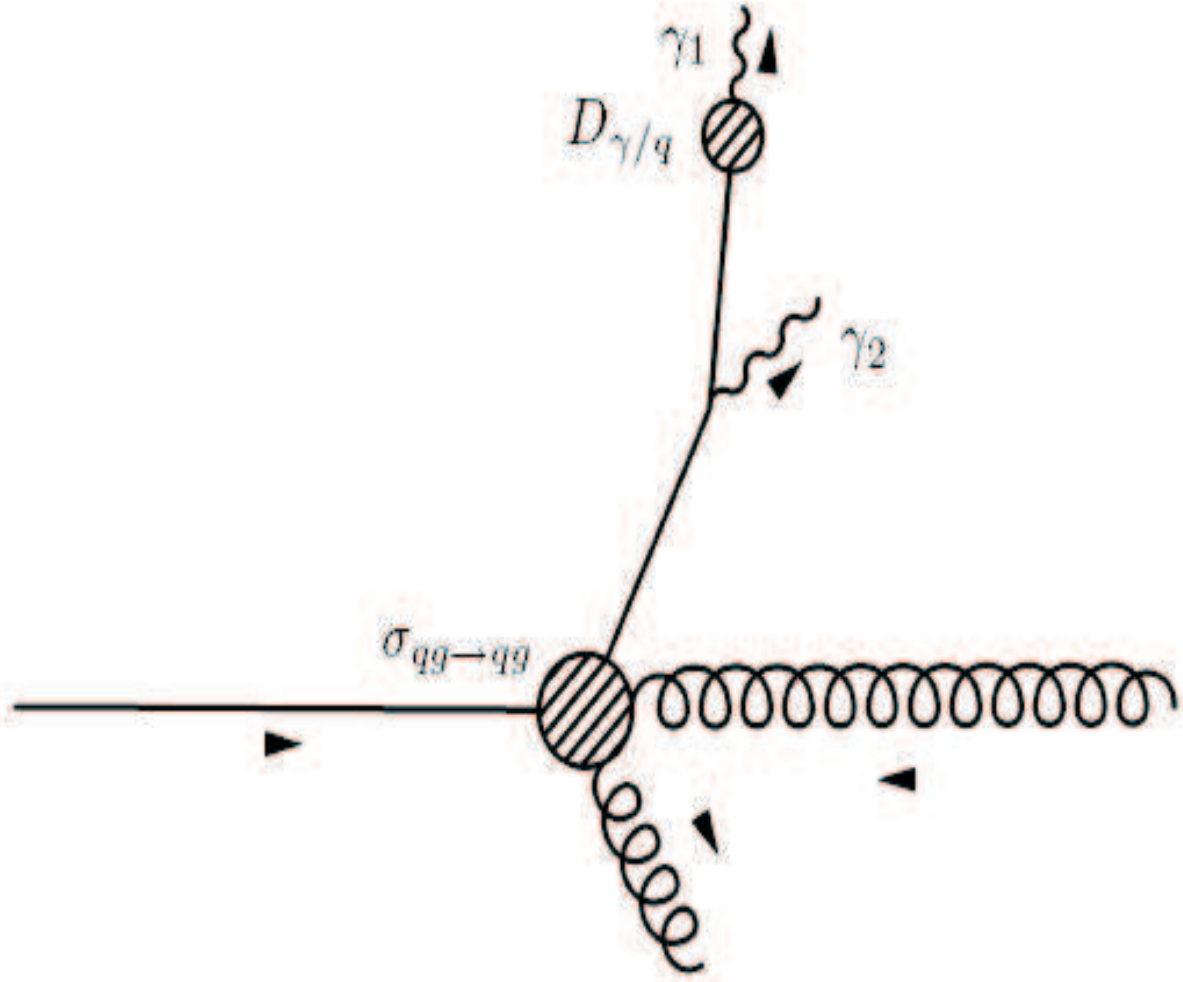

Figure 3.8: Kinematics of the 2→3 processes in DIPHOX : quark-gluon fusion. The quark in the final state radiates a photon, and another photon is produced at the hadronization of the quark.

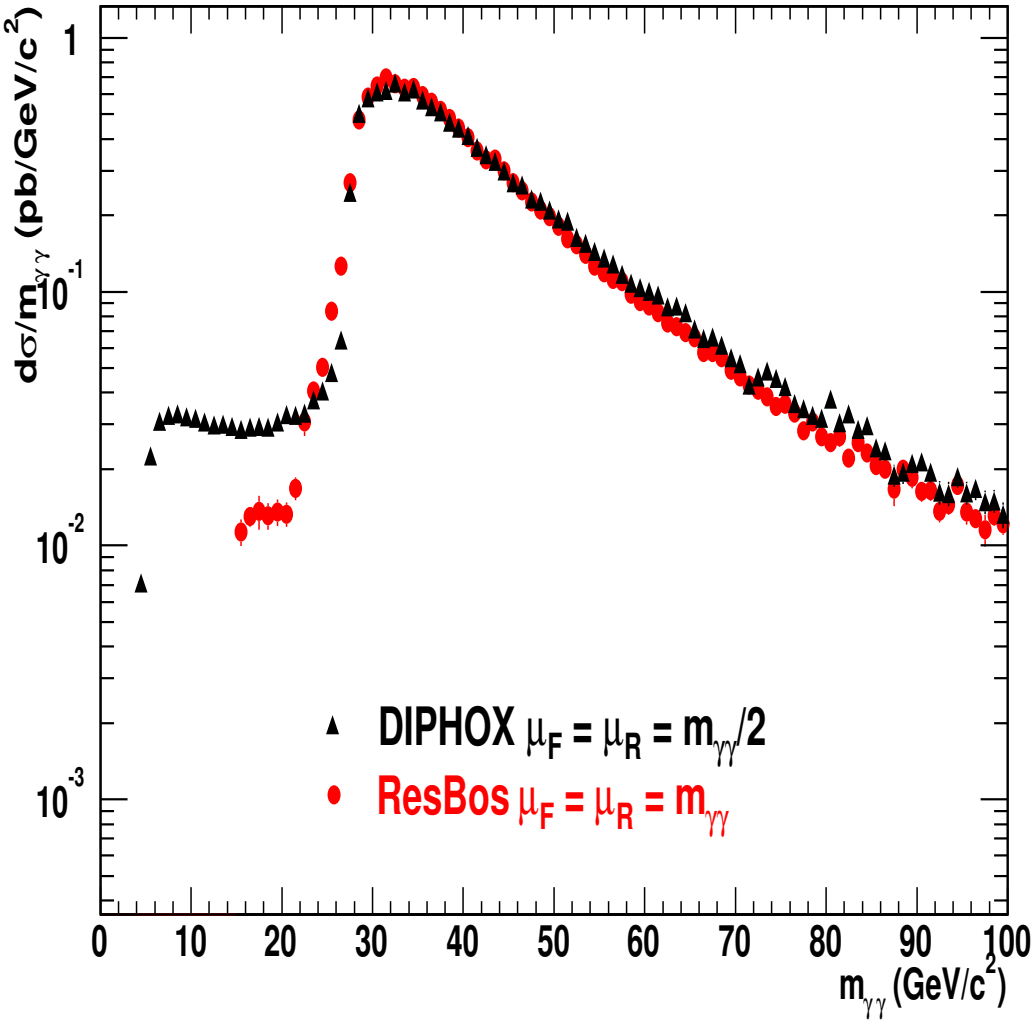

Figure 3.9: Invariant mass distributions from DIPHOX and ResBos. The transverse energy (E_T)of the leading photon is required to be above 14 GeV; the E_T of the softer photon is required to be above 13 GeV. The threshold effect at $m_{\gamma\gamma} = 28$ GeV from the back-to-back contributions is evident. At lower mass, DIPHOX predicts a higher production rate than ResBos due to the $2 \rightarrow 3$ contributions illustrated in Fig. 3.8, which is currently absent in ResBos.

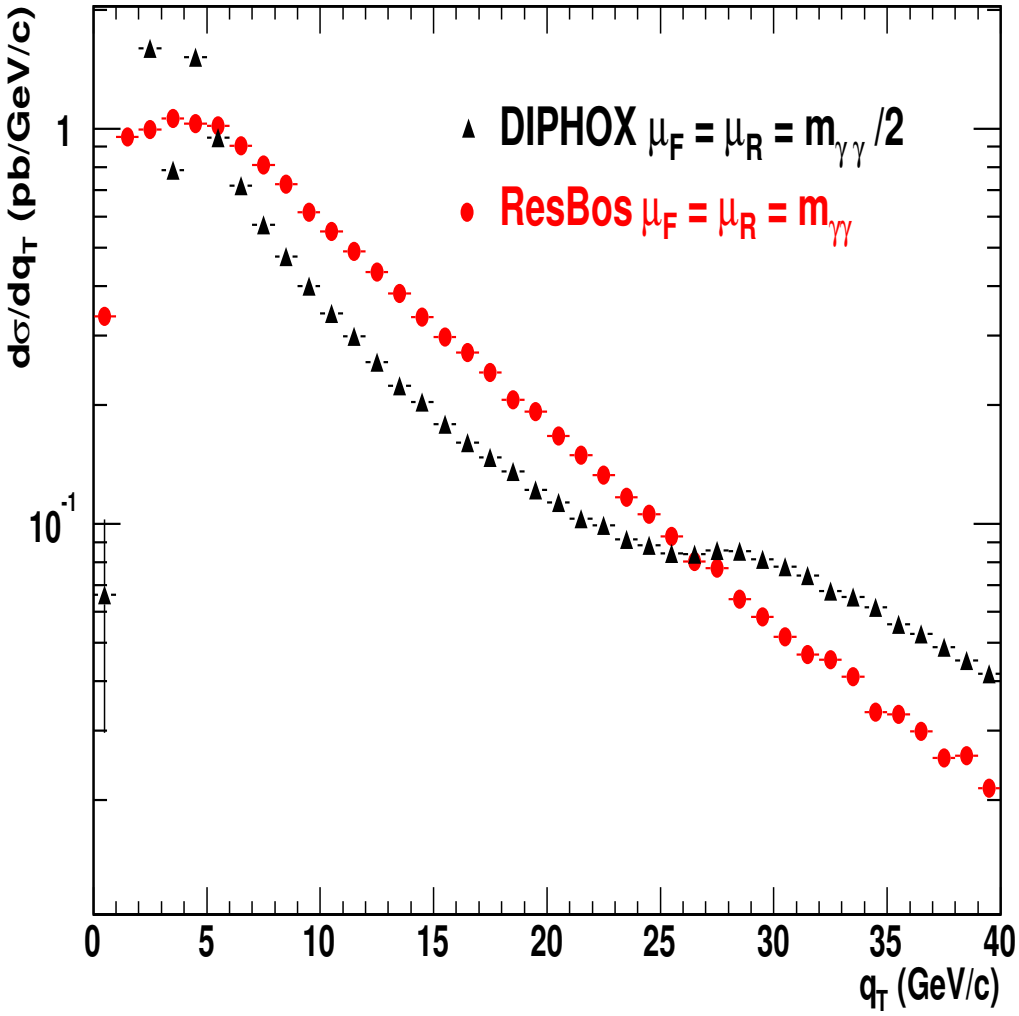

Figure 3.10: Diphoton q_T (the transverse momentum of the two-photon system) distributions from DIPHOX and ResBos. DIPHOX curve is unstable at low q_T due to the divergences of the fixed-order calculation. ResBos resums the effect of multiple soft gluon emissions at initial state and predicts a smooth q_T distribution. DIPHOX curve is enhanced at large q_T due to the $2 \rightarrow 3$ processes illustrated in Fig. 3.8, which is currently absent in ResBos.

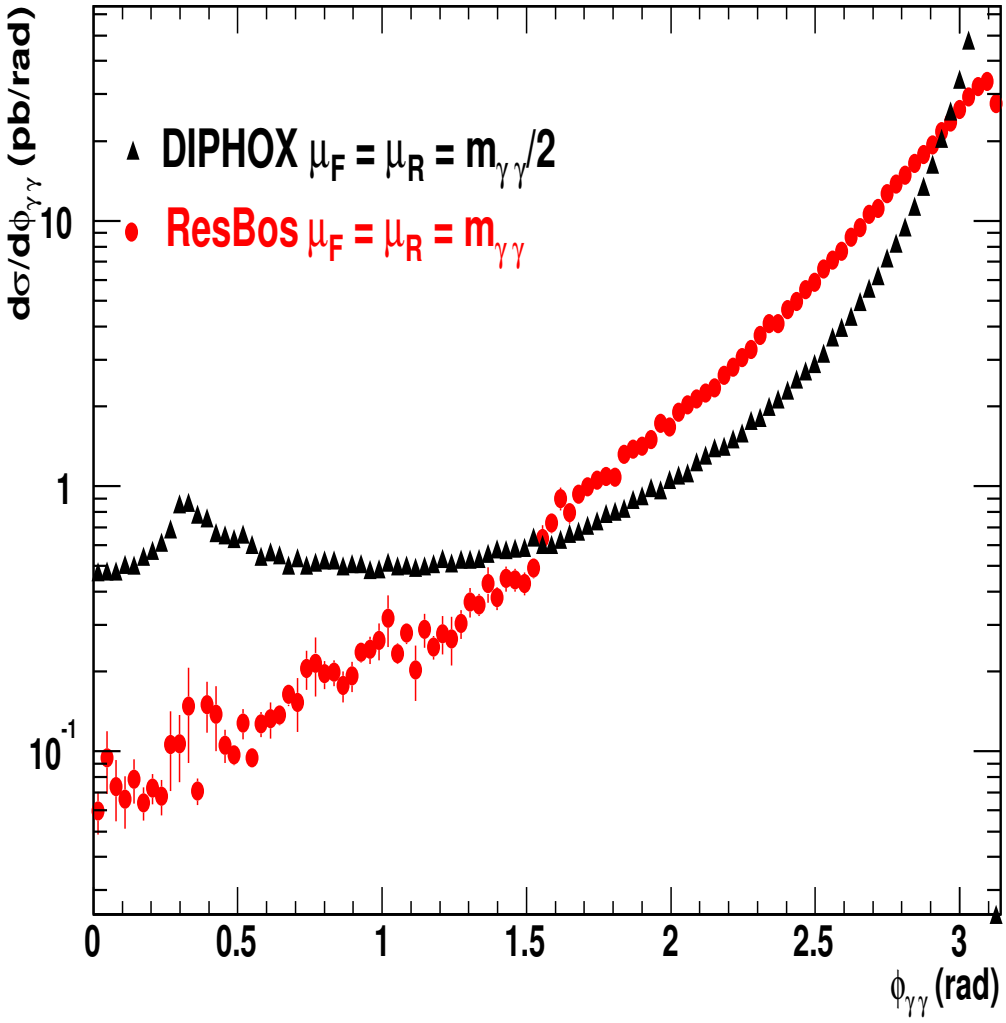

Figure 3.11: $\Delta\phi$ between the two photons ($\phi_{\gamma\gamma}$) from ResBos and DIPHOX. The fixed-order calculation, DIPHOX, is divergent at $\phi_{\gamma\gamma} = 0$ and $\phi_{\gamma\gamma} = \pi$. The divergence at $\phi_{\gamma\gamma} = \pi$ is supressed by an anti-collinear cut implemented in DIPHOX, which requires $\sqrt{(y_{\gamma 1} - y_{\gamma 2})^2 + (\phi_{\gamma 1} - \phi_{\gamma 2})^2} > 0.3$. This cut produces the bump at $\phi_{\gamma\gamma} = 0.3$. On average, the DIPHOX predicts a higher rate for $\phi_{\gamma\gamma} < \pi/2$ region due to the $2 \rightarrow 3$ processes illustrated in Fig. 3.8, which is currently absent in ResBos.

Part II

Experimental Setup

Chapter 4

Tevatron

To date, the Tevatron at Fermi National Accelerator Laboratory (FNAL, or Fermilab) is the most powerful accelerator in the world. The Tevatron accelerates and collides protons and anti-protons in a six-kilometer-long underground ring [49].

4.1 Accelerator

At Fermilab, a chain of accelerators is used to produce and accelerate protons and antiprotons before injecting them into the Tevatron ring. The schematic diagram showing the path of protons and anti-protons is presented in Fig 4.1.

1. Preaccelerator

   The Cockcroft-Walton pre-accelerator provides the first stage of acceleration. The device consists of the source housed in an electrically charged dome. Hydrogen gas (H_2) is ionized to create negative ions(H^-), each consisting of two electrons and one proton. The ions are accelerated by a positive voltage and reach an energy of 750 KeV.

2. Linac

   Next, the negative hydrogen ions enter a linear accelerator, approximately 152 meters long. A system of 14 cylindrical accelerating radio-frequency (RF) cavities arranged collinearly accelerate the 750 KeV negative hydrogen ions to 400

MeV. Before entering the third stage, the ions pass through a carbon foil, which removes the electrons, leaving only the positively charged protons.

3. Booster

   The third stage, the Booster, is located about 6 meters below ground. The Booster is a circular accelerator that uses magnets to bend the beam of protons in a circular path. The protons travel around the Booster about 20,000 times so that they are accelerated by the electric field repeatedly to attain an energy of 8 GeV.

4. Main Injector & Anti-Proton recycler

   The Main Injector, completed in 1999, accelerates particles and transfers beams. It has four functions:

   - It accelerates protons from 8 GeV to 150 GeV.
   - It sends 120 GeV protons to the Anti-proton Source, where the protons protons collide with a nickel (Ni) target. The collisions produce a wide range of secondary particles including many antiprotons, over a large spread of angles and energies centered about the forward direction and 8 GeV. These antiprotons are then debunched and stochastically cooled. The beam is the transferred to the accumulator ring.
   - It receives antiprotons from the Anti-proton Source and increases their energy to 150 GeV.
   - It injects protons and antiprotons into the Tevatron.

   Inside the Main Injector tunnel, an Anti-proton Recycler (green ring) has been installed. It stores unused antiprotons returned from the Tevatron and reject them.

5. Tevatron

   The Tevatron receives 150 GeV protons and antiprotons from the Main Injector and accelerates them to 0.98 TeV. Travelling at a speed close to the light, the

protons and antiprotons circle the Tevatron in opposite directions. The beams cross each other at the centers of the multi-ton CDF and DZero detectors located inside the Tevatron tunnel.

4.2 The luminosity

In high energy collisions, the *instaneous luminosity* $\mathscr{L}$ is defined as the interaction rate per unit cross section ($collisions/(s*cm^2)$). For a process of interest, the number of interaction per second N is then given by

$$N = \sigma \times \mathscr{L}, \tag{4.1}$$

with σ the cross section of the process.

Cross sections are usually given in unit of *barn*, corresponding to 10^{-24}cm^2. The integrated luminosity $\int \mathscr{L} dt$ is then in unit of barn^{-1}.

During the period August 1992 through March 1996, i.e the Run I period, the Tevatron integrated 180 pb^{-1}, with the peak instaneous luminosity of 25×10^{-30} $\text{cm}^{-2}\text{s}^{-1}$.

Run II started integrating luminosity in March 2001. The first portion of data good for studying physics with photons is used in this analysis. The integrated luminosity is 207pb^{-1}($1\text{pb}^{-1} = 10^{36}$ cm^{-2}), corresponding to the February 2002 to September 2003 running period, during which the instaneous luminosity was at the order of $10^{31}cm^{-2}s^{-1}$, see Fig. 4.2.

The CDF acquired luminosities in the four calendar years since the start of Run II are shown in Fig. 4.3. The performance of the accelerator was greatly improved after the 10 week shutdown in the fall of 2003 from the improvements of the beam lifetimes and emittance growth for the recycler.

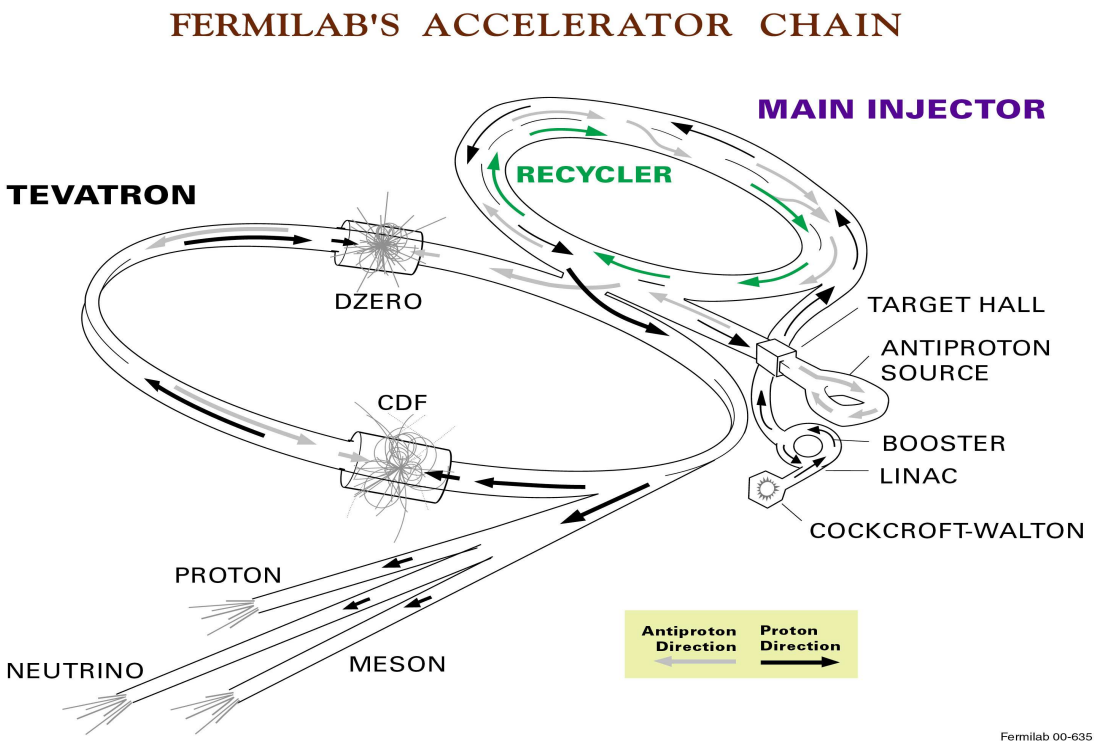

Figure 4.1: The accelerator complex at FNAL.

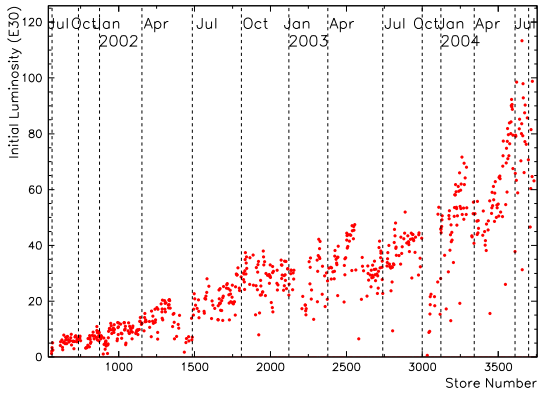

Figure 4.2: Instaneous luminosity of Tevatron Run II as function of store number. The corresponding period is indicated on the top of the figure.

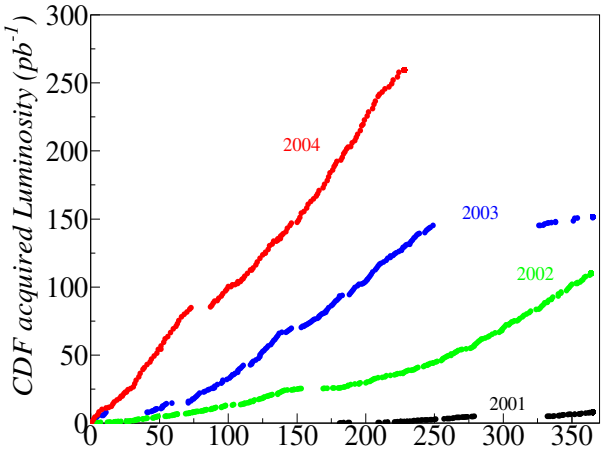

Figure 4.3: CDF acquired luminosities as function of the day in 2001-2004 calendar years.

Chapter 5

The CDF II experiment

The upgraded Collider Detector at Fermilab (CDF II) [15] is one of the two general-purpose detectors built to study the high energy collisions at the Tevatron. It is a solenoidal detector which combines high precision charged particle tracking with fast projective calorimetry and fine grained muon detection, designed for a maximum solid angle coverage. An isometric view of the detector is shown in Fig 5.1; an elevation view is shown in Fig 5.2. In this chapter, sub-systems of CDF will be described, with emphasis on components that are important for photon detection.

5.1 The CDF coordinate system

CDF uses a left-handed Cartesian coordinate system : the origin is located at the center of the detector, which is also the nominal collision point. The positive z-axis points along the beam-line in the direction of protons (west to east); the x-axis points horizontally towards the center of the ring, and the y-axis points upwards; θ, ϕ are used to denote polar and azimuthal angles respectively. The variable *pseudorapidity*, defined as

$$\eta \equiv -\ln(\tan(\frac{\theta}{2})), \tag{5.1}$$

is typically used for convenience - it is the massless approximation of the *rapidity* ($y \equiv \frac{1}{2}\ln\frac{E+p_z}{E-p_z}$) which is additive under Lorentz boosts along the z direction. The

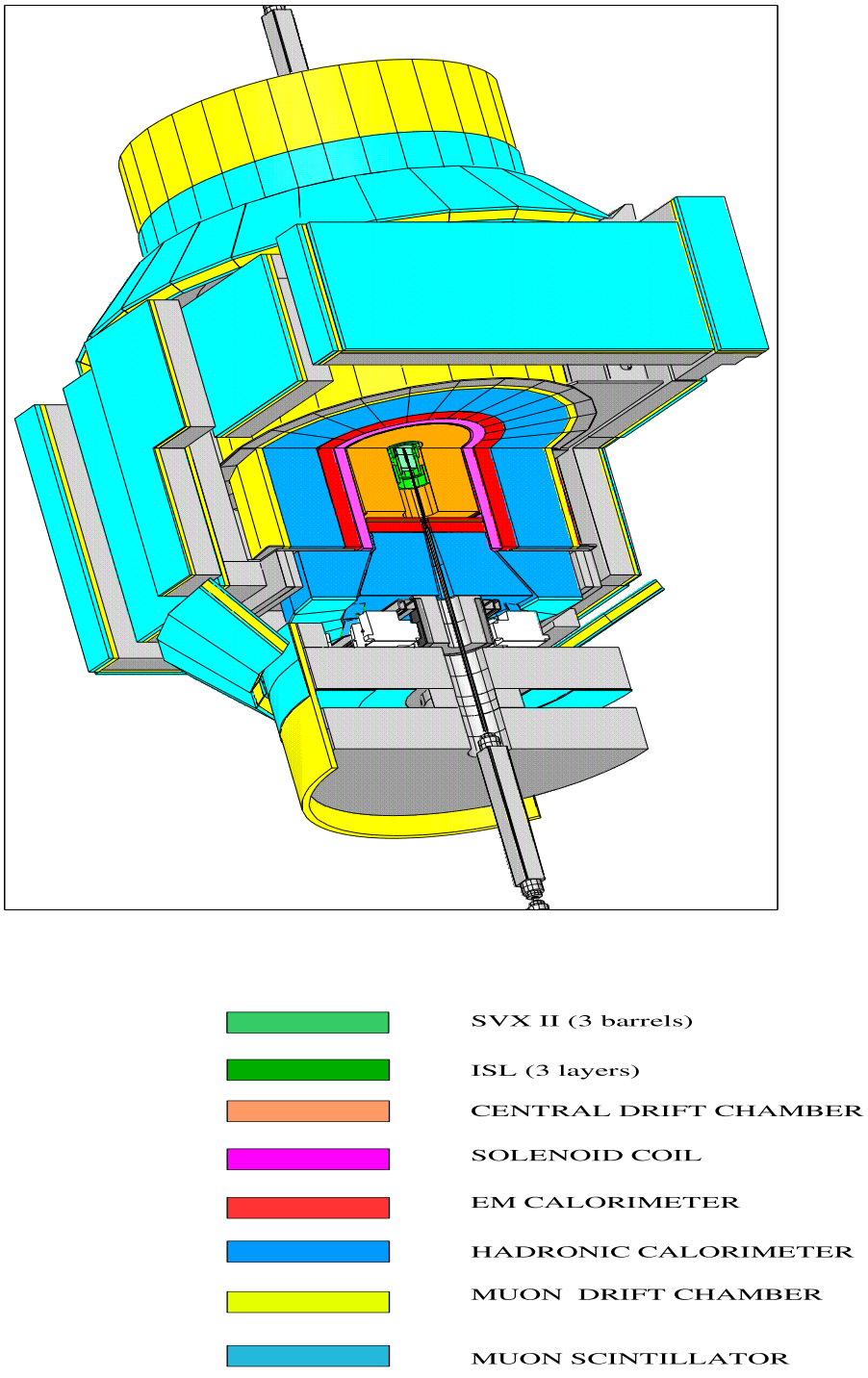

Figure 5.1: An isometric view of the CDF II detector

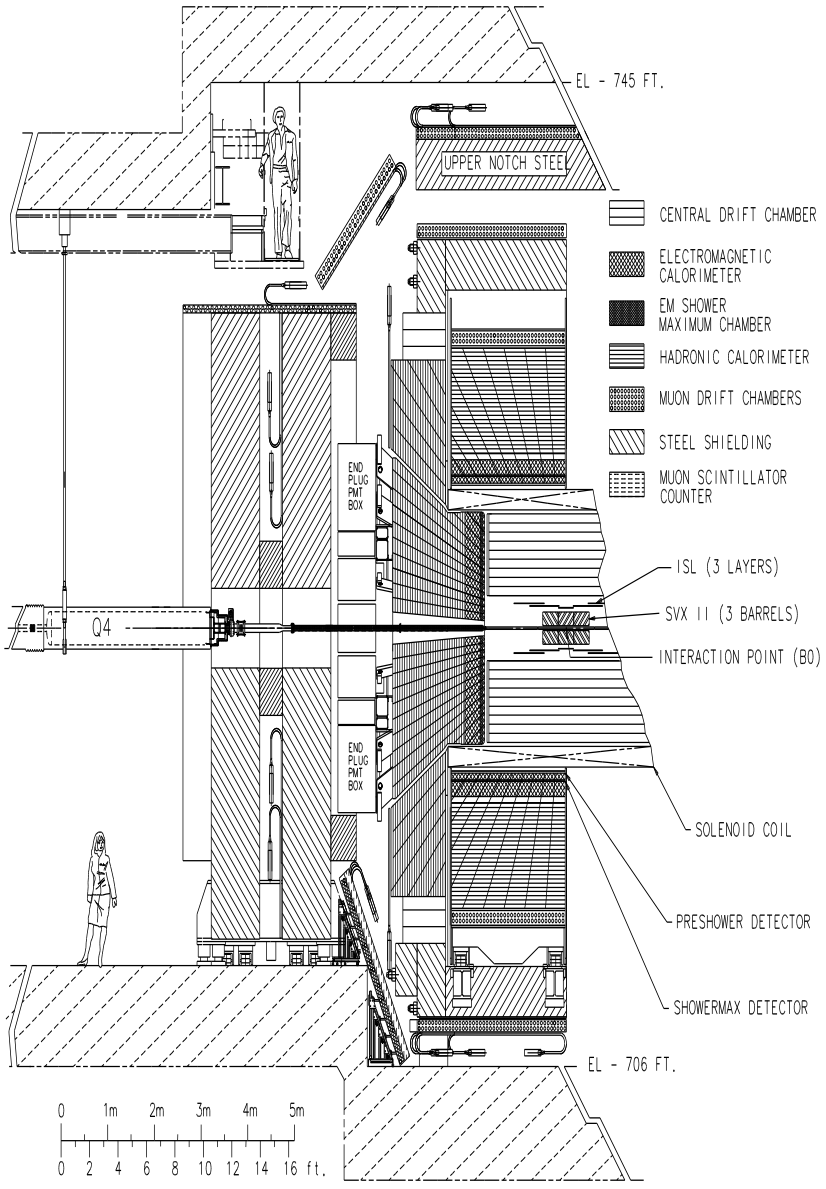

Figure 5.2: An elevation view of the CDF II detector

pseudo-rapidity is equal to zero at $\theta = \pi/2$, and have positive values in the proton direction($z > 0$) .

The transverse energy (E_T) and transverse momentum (p_T) are the projection of energy and momentum to the x-y plane:

$$p_T = p \times \sin(\theta), \tag{5.2}$$

$$E_T = E \times \sin(\theta). \tag{5.3}$$

5.2 An overview of the detector

The CDF II detector can be viewed as being made up of three main functional parts: the tracking system, the calorimetry, and the muon detectors. A super-conducting solenoidal magnet provides a 1.4 T magnetic field parallel to the beam axis in a volume of 1.5 m in radius and 4.8 m in length, which contains the tracking detectors. The calorimetry and muon detectors are all outside the solenoid. The following sections will provide a brief review of the sub-systems.

5.3 The tracking system

The tracking system is very important for the entire experiment - the correlation of tracks with Electromagnetic (EM) calorimetry and muon chamber information is the basis of lepton identification. The correlation at the trigger level allows low p_T thresholds for efficient collection of top candidates, W boson decays, and high rate B physics triggers. At the offline level, more precise versions of this correlation, using shower position and E/p for electrons, and stub position and slope for muons give high purity, high efficiency lepton selection. The tracks are also used for *in situ* calibration of the central calorimeter. A J/ψ peak, recorded with low p_T muon triggers is compared with the world average J/ψ mass to normalize the momentum scale of the tracking system. This calibration is then transfered to the EM calorimeter

using the electron tracks in a large sample of inclusive electrons. The response of the hadron calorimeter is measured using a large sample of isolated tracks, and this is combined with test beam data to normalize the absolute scale. The scale of the hadron system is then checked against the EM calibration using events where a single jet recoils against a well-identified photon or a $Z \rightarrow e^+e^-$ decay.

The CDF II tracking system is schematically shown in Fig 5.3. At large radii (48 to 131cm), a open cell drift chamber, the COT, which uses small drift cells and a fast drift gas to achieve drift times less than 100 ns, covers the region $|\eta| \leq 1.0$. In the COT four axial and four stereo super-layers with 12 wires each will provide 96 measurements, using 30240 readout channels (16128 axial and 14112 stereo) for the entire detector. The entire COT is roughly 1.3% radiation lengths at normal incidence. The COT provides hit resolution of $\sim$ 140 microns. The momentum resolution with COT stand-alone tracking is roughly $\sigma p_T/p_T \sim 0.0015 p_T$, with p_T measured in GeV.

Inside the COT, a silicon "inner tracker" is composed of two components.

- A micro-vertex detector (SVX II) at very small radii (between 2.4 cm and 10.7 cm) establishes the ultimate impact parameter resolution. The SVX II is composed of three cylindrical barrels with a total length of 96 cm. It covers $\sim$ 2.4 σ of the luminous region, resulting in an almost 100% geometrical acceptance for b-tagging. Each barrel supports five layers of double-sided silicon micro-strip detectors. One side of all layers is azimuthal; on the other sides three layers are perpendicular to the azimuth and two are 1.2° small angle stereo.

- In the central region, a layer of double-sided silicon is placed at a radius of 22 cm. In the region $1.0 \leq |\eta| \leq 2.0$, two layers of double-silicon are placed at radii of 20 cm and 28 cm. These silicon layers are called the Intermediate Silicon Layers (ISL). The Intermediate Silicon Layers (ISL) use similar technology to that of SVX II. All layers make an $r - \phi$ and a 1.2° small angle stereo measurement.

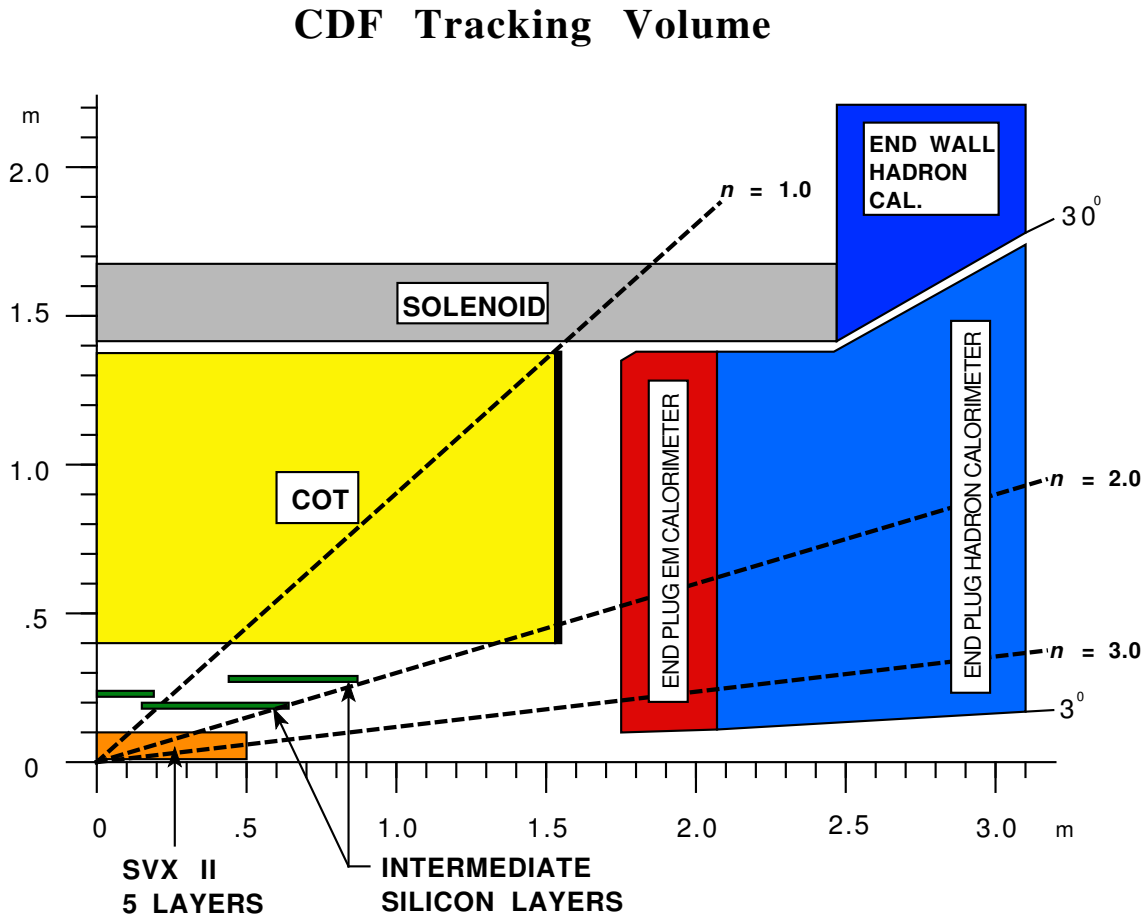

Figure 5.3: The cross section schematic view of the CDF II inner tracking system. The tracking system consists of a silicon tracker at small radius surrounded by a large open cell drift chamber. The silicon tracker is made of five layers of Silicon Vertex detector (SVX II) at very small radius, followed by three layers of Intermediate Silicon Layers(ISL).

5.4 The calorimetry

The calorimetry consists of two subsystems, covering different pseudo-rapidity regions: central ($|\eta|$ <1.1) and plug (1.1< $|\eta|$ <3.6).

5.4.1 The Central Calorimeter

The central calorimeter is divided into the EM compartment (CEM) followed by a hadron compartment (CHA) located just after. Both calorimeters are segmented into towers of granularity of $\Delta\eta \times \Delta\phi \approx 0.1 \times 0.26$. The Central Electromagnetic calorimeter (CEM) [16], the most important component of this analysis, consists of a scintillator-lead sampling calorimeter along with an embedded multi-wire proportional chamber (CES) located near shower maximum at six radiation lengths.

The characteristic of the CEM are summarized in Table 5.1.

An inner aluminum base plate, 0.55 in. thick on average, begins the CEM calorimeter at a perpendicular radius of 68 in. from the beam line. In the CEM, there are 31 layers of 5 mm thick SCSN-38 polystyrene scintillator, cut and polished on the interior sides. Interleaved with the scintillator are 30 layers of $\frac{1}{8}$ in. thick lead (Pb), clad on both sides with 0.015 in. aluminium. The CES is between the eighth lead layer and the ninth scintillator layer. In order to maintain a constant radiation length thickness as polar angle (θ) varies, both at the strip chamber and total depth, acrylic is substituted for lead in certain layers. The towers, and the strip chamber in one module (a $\Delta\phi \approx 0.26$ slice, i.e, one wedge) of CEM is drawn schematically in Fig. 5.4. There are 24 wedges on each side.

One wedge [1]is notched to allow a "chimney" for access to the super-conducting solenoid. The EM calorimeter of that wedge is 12 in. shorter than usual, with seven normal towers and one combined tower; thus, the total number of photo-tubes used in the CEM is 48 modules × 10 towers per module × 2 photo-tubes per tower - 2 "chimney" towers × 2 photo-tubes per tower = 956.

The CES measures the charge deposition on orthogonal strips and wires. Cathode strips running in the azimuthal direction provide z information, while anode wires

[1]The chimney wedge is tower 5 at the east side.

running in the z direction provide r-ϕ information. The orientations of strips and wires are shown in Fig. 5.5. Inside each chamber the wires running along z directions are split in the middle in $|z|$ (at approximately 121 cm). There are 32 wires at low $|z|$, and 32 at high $|z|$ for a total of 64 on one side in one wedge. The strips are slightly different pitch in low |z| (1.57 cm in towers 0-4) and high |z| (2.01cm in towers 5-9) [2]. The CES allows for a position determination of the EM shower and for a measurement of the shower transverse profile. The average energy resolution of the CEM is $\sigma(E)/E = 13.5\%\sqrt{E\sin\theta}$ (with E in GeV) and the position resolution of the CES is $\pm$ 2mm for photons with E_T above 30 GeV.

Another important component for this analysis is the Central Preradiator Chamber (CPR) mounted in front of the wedges, and just outside the magnet coil. The CPR is a set of four multi-wire proportional chambers, two at each side, positioned at a radius of 162 cm from the beam-line (between the solenoid and the CEM). Inside each CPR chamber, the wires running along the z direction are split at about $z \approx 120$ cm. There are 16 wires at low |z| (7.9< |z| <119.7 cm) and 16 at high |z| (123.5< |z| <235.3 cm). The CPR samples the early EM shower development in the solenoid, which is very important for determining the background contamination from neutral mesons that decay to multiple photons for the high E_T region. More details are described in Chapter 6.

The central and end-wall hadron calorimeter [17] are composed of alternating layers of iron and scintillator. The central modules, forming four "C"-shaped arches, cover polar angles between 45° and 135°. They are 32 layers deep and each module weighs 12 tons. The end-wall modules cover polar angles from 30° to 45° and from 135 ° to 150 °. One quadrant of the calorimeters is shown in Fig. 5.6.

The parameters of Center and End-Wall hadron calorimeters are summarized in Table 5.2 and 5.3 respectively.

[2] see the Fig 5.4 .

Modules		
	12/arch + 2 spare	50
	Length	98 in.
	Width	15° in ϕ
		(or 17.9in. at 68+ in. from beam-line)
	Depth(including base plate)	13.6in.
	Weight	2 tons
Towers		
	10/module	478
	Length	$\Delta\eta$ 0.11
	Thickness	18 X_0
	Layers	20-30 lead
		21-31 scintillator
		1 strip chamber
	Lead	$\frac{1}{8}$ in. aluminum clad
	Scintillator	5 mm SCSN-38 polystyrene
	Wavelength shifter	3 mm Y7UVA acrylic
	Photomultiplier tubes	Hamamatsu R580
	(956 channels)	($1\frac{1}{2}$ in.)
Chambers		
	Depth	5.9 X_0 (including coil)
	Wire channels(64/module)	3072
	Strip channels(128/module)	6130
Angular coverage		
	θ	about 39° - 141°
	ϕ	complete
	η	about $\pm$1.1
Performance	(high = 30+ GeV)	
	pe/GeV	100+ /tube
	Energy resolution σ/E[GeV]	$13.5\%/\sqrt{E}$
	position resolution (high)	$\pm$2 mm
	Strip/wire PH correlation	8-10%
	Wire PH resolution(high)	$\pm$25%

Table 5.1: Central electromagnetic calorimeter (CEM) technical summary.

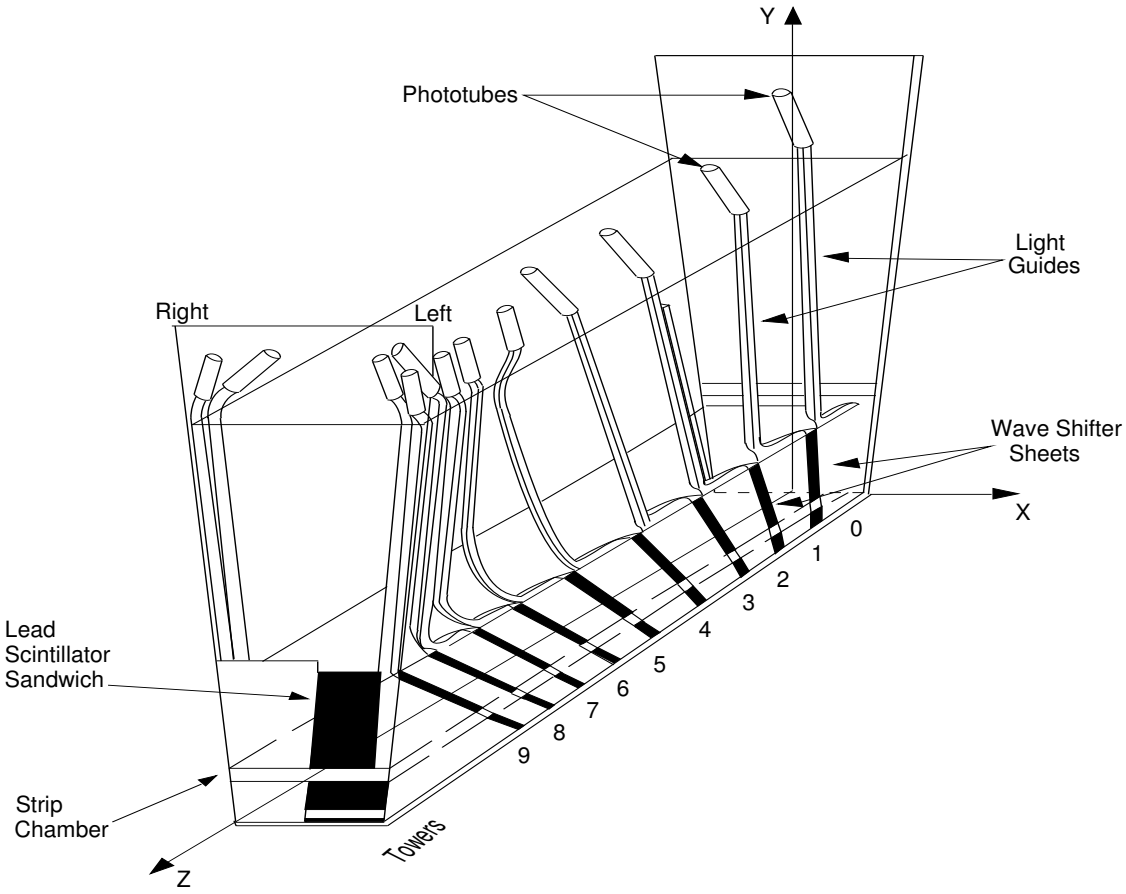

Figure 5.4: The cut-away view of a CEM wedge.

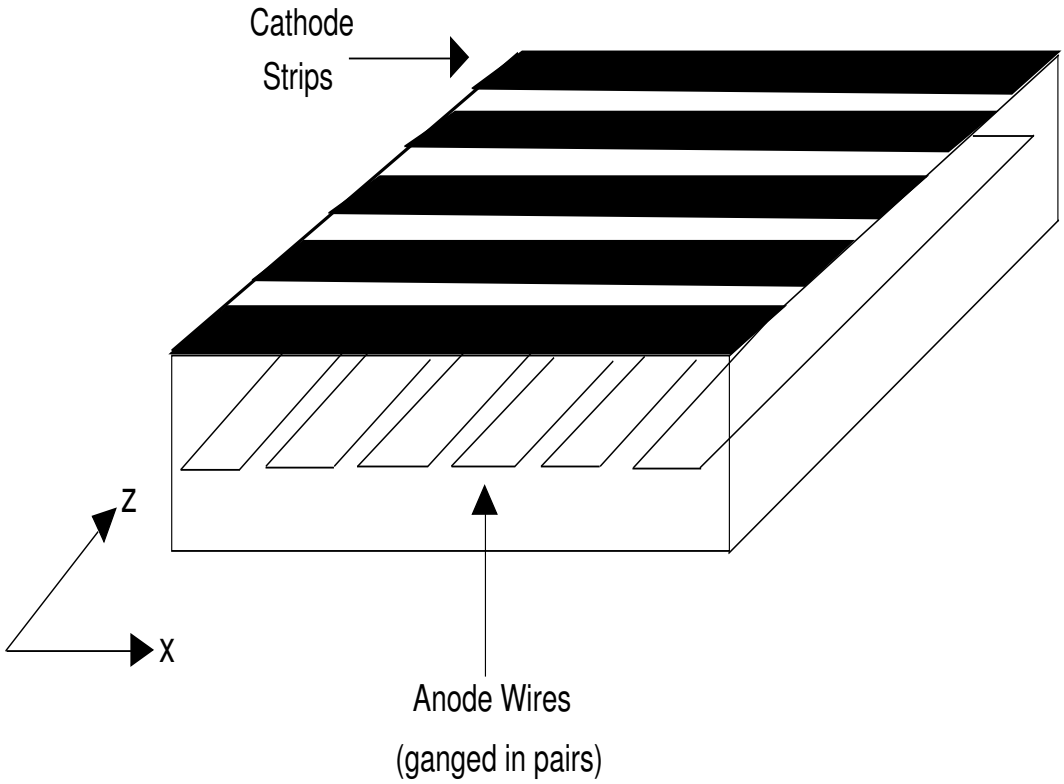

Figure 5.5: Diagram of the CES strip/wire orientations: Cathode strips running in the azimuthal direction provide z information, while anode wires running in the z direction provide r-ϕ information.

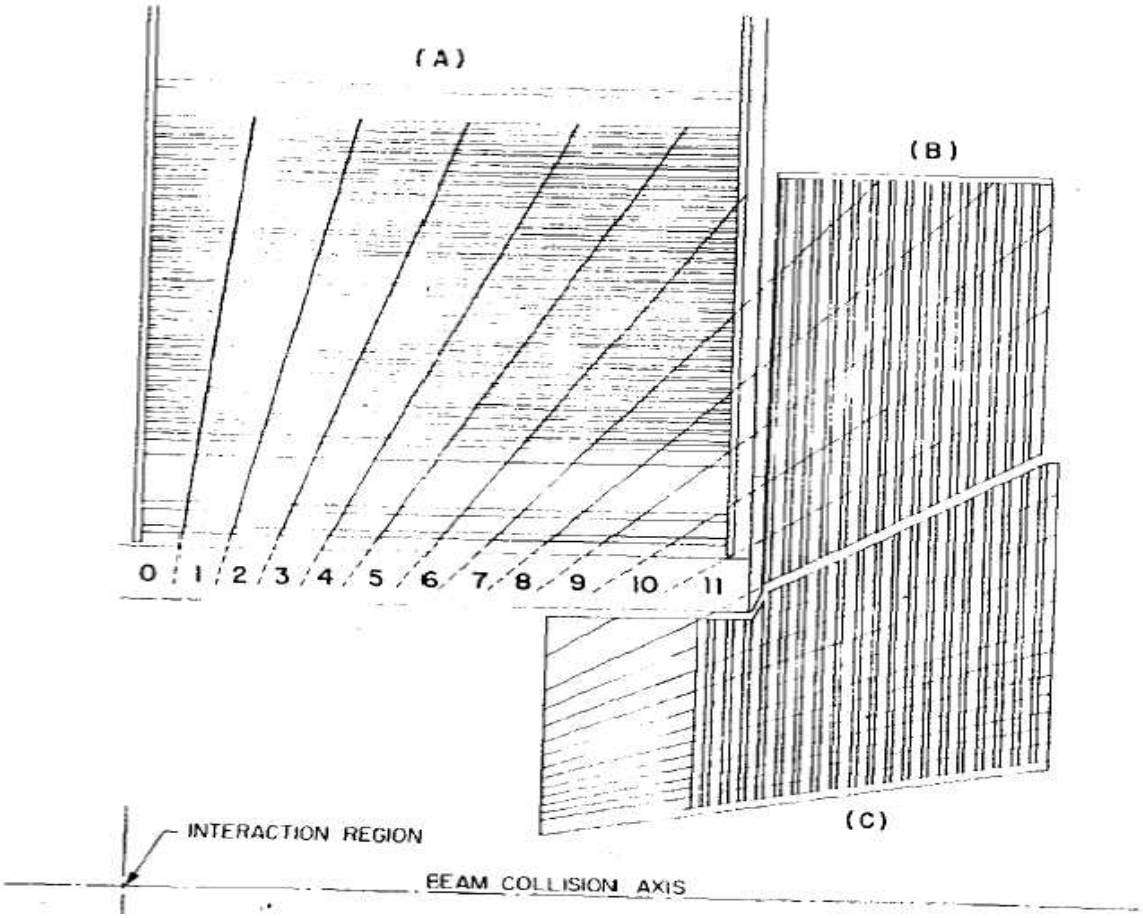

Figure 5.6: Quadrant of the calorimeter where A,B,C show Central, End-Wall and Plug respectively. Towers are numbered from 0 (at 90° in polar direction) to 11 (last tower of End-Wall modules). Hadronic towers 6,7 and 8 are shared between Central and End-Wall calorimeter. [17]

Modules	
Number of modules	48
Length	2.5 m
Width (in ϕ direction) 1.33 m	
weight per module	12,000 kg
towers	
Total number (8/module)	384
Length($\Delta\phi = 15°$)	0.56 to 0.91 m
Width ($\Delta\eta = 0.11$)	0.28 to 0.45 m
Total depth (hadron calorimeter alone)	4.7 Λ_{abs}
Layers	
Number	32
Steel thickness	2.5 cm
Scintillator thickness	1.0 cm
Scintillator type	PMMA doped with 8% Naphtalene 1% Butyl-PBD and .01% POPOP
Wave shifters	UVA PMMA doped with 30 mg/l Laser dye #481
Number of phototubes	768

Table 5.2: Parameter of the Central hadron Calorimeter [17].

Modules	
Number of modules	48
Approximate dimensions	$0.8 \times 1.0 \times 1.1 m^3$
Weight per module	7,000 kg
Towers	
Total number (6/module)	288
Length ($\Delta\phi = 15^\circ$)	0.35 to 0.78 m
Width ($\Delta\eta = 0.11$)	0.25 to 0.40 m
Total depth (hadron calorimeter alone)	4.5 Λ_{abs}
Layers	
Number	15
Steel thickness	5 cm
Scintillator thickness	1.0 cm.
Scintillator type	PMMA doped with 8% Naphtalene 1% Butyl-PBD and .01% POPOP
Wave shifters	UVA PMMA doped with 30 mg/l Laser dye #481
Number of phototubes	576

Table 5.3: Parameters of the End Wall hadron Calorimeter [17].

5.4.2 The Plug Calorimeter

The plug calorimeter is divided into electromagnetic and hadronic sections. In both sections, the active elements are scintillator tiles read out by wavelength shifting (WLS) fibers embedded in the scintillator.

The plug EM calorimeter [18] is a lead/scintillator sampling type, with unit layers composed of 4.5 mm lead and 4 mm scintillator. There are 23 layers in depth for a total thickness of about 21 X_0 (radiation lengths) at normal incidence. Just behind the 4th lead plate, a shower-max position detector (PES) [19] is embedded, which is composed of plastic scintillator strips (5 mm wide and 6 mm thick) with optical fiber readout. In front of the first lead layer is another scintillator layer, acting as a preshower detector (PPR). The energy resolution of the EM section is approximately $14.4\%/\sqrt{E}$ with a 0.7% constant term.

The hadron calorimeter is a 23 layer iron and scintillator sampling device. Some parameters of the the plug calorimeter are listed in Table. 5.4.

	EM	HAD
Segmentation	$\sim$8×8 cm^2	$\sim$24×24 cm^2
Total Channels	960	864
Thickness	21 X_0, 1λ_0	7 λ_0
Density	0.36 ρ_{Pb}	0.75 ρ_{Fe}
Samples	22+Preshower	23
Active	4 mm Scint	6 mm Scint
Passive	4.5 mm Pb	2 inch Fe
Light Yield (pe/MIP/tile)	$\geq$ 3.5	$\geq$ 2.2
Resolution	$16\%/\sqrt{E}\oplus 1\%$	$80\%/\sqrt{E}\oplus 5\%$

Table 5.4: Over view of the plug calorimeter [15]. The EM (hadron) resolution is the designed specification for a single electron (pion).

5.5 Muon detectors

Four systems of scintilators and proportional chambers in CDF II are used for the detection of muons over the region $|\eta| \leq 2.0$. The calorimeter steel, magnet return yoke, additional steel walls are the absorbers of the muon detectors. The design parameters of the 4 muon systems are listed in Table. 5.5.

The Central Muon detector (CMU) [20], the original set of drift chambers for muon detection, covers $|\eta| < 0.6$, and is embedded at the outer radius of the central calorimeter wedges.

The Central Muon Upgrade (CMP) consists of a second set of muon chambers behind an additional 60 cm of steel in the region $55^\circ \leq \theta \leq 90^\circ$. The central upgrade chambers are rectangular, single-wire drift tubes. The CSP is a layer of scintillation counters installed on the outside surface of the wall drift chambers. Further information about the CMP detector can be found in [21].

The Central extension consists of conical sections of drift tubes (CMX) and scintillation counters (CSX) located at each end of the central detector and extending in polar angle from 42° to 55°.

The Intermiediate MUon detector (IMU) is designed to trigger on muons with $|\eta| \leq 1.5$ and to identify offline muons with $|\eta| \leq 2.0$. The detector consists of a barrel of CMP-like chambers and CSP-like scintillation counters mounted on the outer

	CMU	CMP/CSP	CMX/CSX	IMU
Pseudo-rapidity coverage	$\lvert\eta\rvert \leq\sim 0.6$	$\lvert\eta\rvert \leq\sim 0.6$	$\sim 0.6 \leq \lvert\eta\rvert \leq\sim 1.0$	$\sim 1.0 \leq \lvert\eta\rvert \leq\sim 1.5$
Drift tube cross-section	2.68×6.35 cm	2.5×15 cm	2.5×15 cm	2.5×8.4 cm
Drift tube length	226 cm	640 cm	180 cm	363 cm
Max drift time	800 ns	1.4 μs	1.4 μs	800 ns
Total drift tubes	2304	1076	2208	1728
Scintillator counter thickness	-	2.5 cm	1.5 cm	2.5 cm
Scintillator counter width	-	30 cm	30-40 cm	17 cm
Scintillator counter length	-	320 cm	180 cm	180 cm
Total counters	-	269	324	864
Pion interaction lengths	5.5	7.8	6.2	6.2-20
Minimum detectable muon p_T	1.4 GeV/c	2.2 GeV/c	1.4 GeV/c	1.4-2.0 GeV/c
Multiple scattering resolution	12 cm/p (GeV/p)	15 cm/p	13 cm/p	13-25 cm/p

Table 5.5: Design parameters of the CDF II Muon detectors. Pion interaction lengths and multiple scattering are computed at a reference angle of $\theta = 90°$ in CMU and CMP/CSP, at an angle of $\theta = 55°$ in CMX/CSX, and show the range of values for the IMU. [15]

radius of the FMU toroids, and pinwheels of counters on the endwall and between the toroids for triggering.

5.6 The luminosity monitor

A Cherenkov Luminosity Counter (CLC) [22] has been constructed for the precision measurement of the machine luminosity. The detector consists of long, conical, gaseous Cherenkov counters that point to the collision region and monitor the average number of inelatic $p\overline{p}$ interactions by measuring the number of particles, and their arrival time, in each bunch crossing.

The CLC detector consists of 2 modules which are located inside the "3-degree holes" inside the CDF end-plug calorimeters, covering the pseudo-rapidity region $3.7\leq |\eta| \leq 4.7$. Each module consists of 48 thin, long, conical, gas-filled Cherenkov counters. The counters are mounted on a long ($\sim$ 230 cm), thin (0.9 mm) aluminium tube that surrounds the beam pipe. The complete structure is enclosed in a thin, aluminium pressure vessel, filled with isobutane. The nominal operation pressure is 1 atmosphere.

Prompt particles coming from the $p\overline{p}$ interactions traverse the full length of the

counter and generate a large amount of light (a large amplitude PMT signal : ~ 100 photoelectrons). The light yield of particles from beam-halo or secondary interactions is significantly smaller because they transverse the counters at large angles (therefore shorter path lengths), and the produced light experiences a large number of relfections. A suitable amplitude threshold at the data analysis stage can discriminate against non-prompt particles.

Additionally, the time resolution of the Cherenkov counters is below 100 ps [23], which makes it possible to estimate the number of $p\overline{p}$ interactions in a given beam crossing by studying the time distribution of the hits and counting the number of time clusters. The alternative method helps reduce the systematic uncertainties in the measurement.

5.7 The trigger system

The trigger plays an important role in hadron collider experiments because the collision rate is much higher than the rate at which the data can be stored on tape (at CDF Run II, the collision rate is effectively equal to the crossing rate of 7.6 MHz, while the tape writing speed is less than 50 Hz).

The CDF trigger system has a three-level architecture with each level providing a rate reduction sufficient to allow for processing in the next level with minimal deadtime [24]. The functional block diagram of the trigger system is shown in Fig. 5.7. The trigger system consists of two hardware levels. The Level-1 trigger reads an event and makes decision (L1-accept / L1-reject) in every beam crossing. The L1 buffer is 42 crossings deep. The Level-2 trigger processes events that have received a L1-accept in a time ordered fashion. It is structured as a two stage pipeline with data buffering at the input of each stage. The first stage is based on dedicated hardware processors which assemble information from a particular section of the detector (Calorimeter, Clusters, SVX tracks etc). The second stage consists of programmable processors (DEC Alpha processors) operating on lists of objects generated by the first stage. Storage of four events is provided in L2 buffers. Trigger decisions are based

on information from calorimeter towers (CAL), central strip chambers (CES), central outer tracker (COT), muon chambers and muon scintillators, and silicon vertex detectors. The Trigger Supervisor Interface (TSI) provides an interface between the trigger system and the DAQ and clock.

The L1CAL subsystem uses transverse energy summed into *trigger towers* of approximately $0.2 \times 15^{\circ}$ in $\eta - \phi$ space [25] and tracks from XFT track processor to form electron, photon and jet trigger objects. L1CAL also calculates the ΣE_T and missing E_T for the events for use by L1 GLOBAL. The MUON subsystem uses muon primitives and XFT tracks extrapolated to the muon chambers by the XTRP to form muon trigger objects. Coincidence with muon scintillators where applicable is used to remove muon stubs from other crossings. The L1 Track subsystem is designed to trigger purely on tracks in the COT to provide an efficient trigger path for hadronic B decays.

The Level-2 trigger has available as inputs the trigger primitives generated for L1 : Trigger Tower energies, XFT tracks and muon stubs. Additional data for L2 come from the shower maximum strip chambers and the $r - \phi$ strips of SVX II. There are three hardware sub-systems generating primitives at Level 2 : L2CAL, XCES, and Silicon Vertex Tracker (SVT).

The Level-3 trigger uses the full detector information to fully reconstruct events in a processor farm.

Photon candidates are collected by the calorimeter triggers : L1CAL, L2CAL and L3 reconstructed photon candidates. More details are described in Chapter 6.

5.8 Offline reconstruction

The events are processed with the full reconstruction code, which performs three dimentional tracking, and identifies jet, photons, electrons and muon candidates.

Jets are formed by finding clusters of energy in the calorimeter. There are various algorithms to combine towers to form jets. A good algorithm should satisfy a set of requirements such that the kinematic properties of the jets can be related to the corresponding properties of the energetic partons produced in the hard scattering

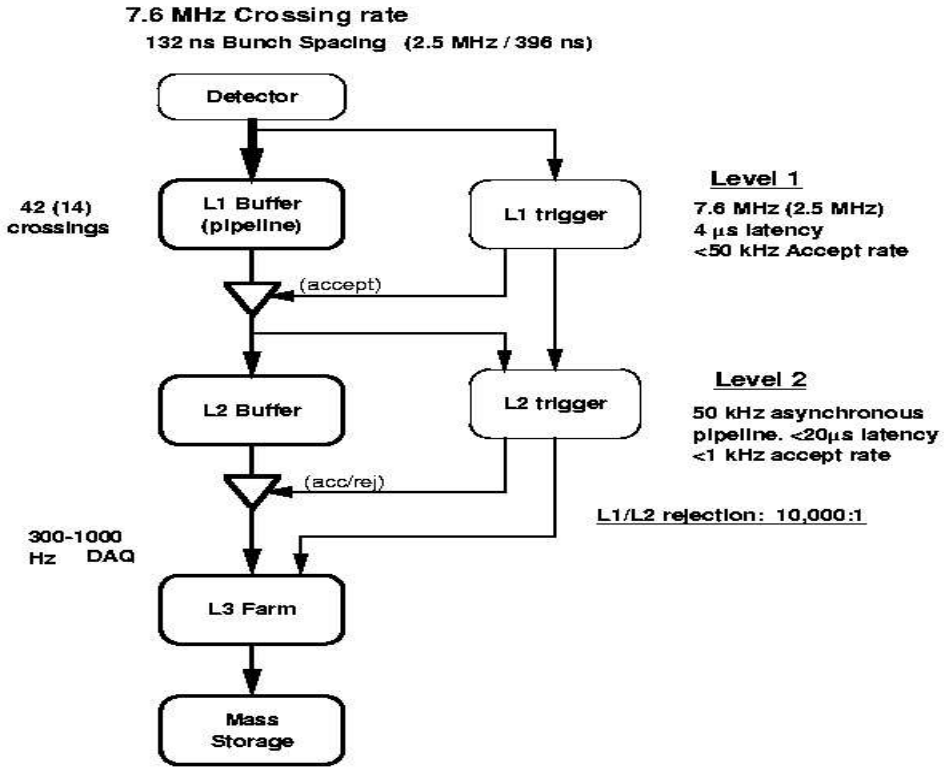

Figure 5.7: Functional block diagram of the 3-level trigger system. For each level-1 accept the data is stored in a L2/DAQ buffer while the Level-2 trigger works. A level-2 accept initiates the read-out of the event data into the Level-3 processor farm where an accept causes the data to be written to disk/tape.

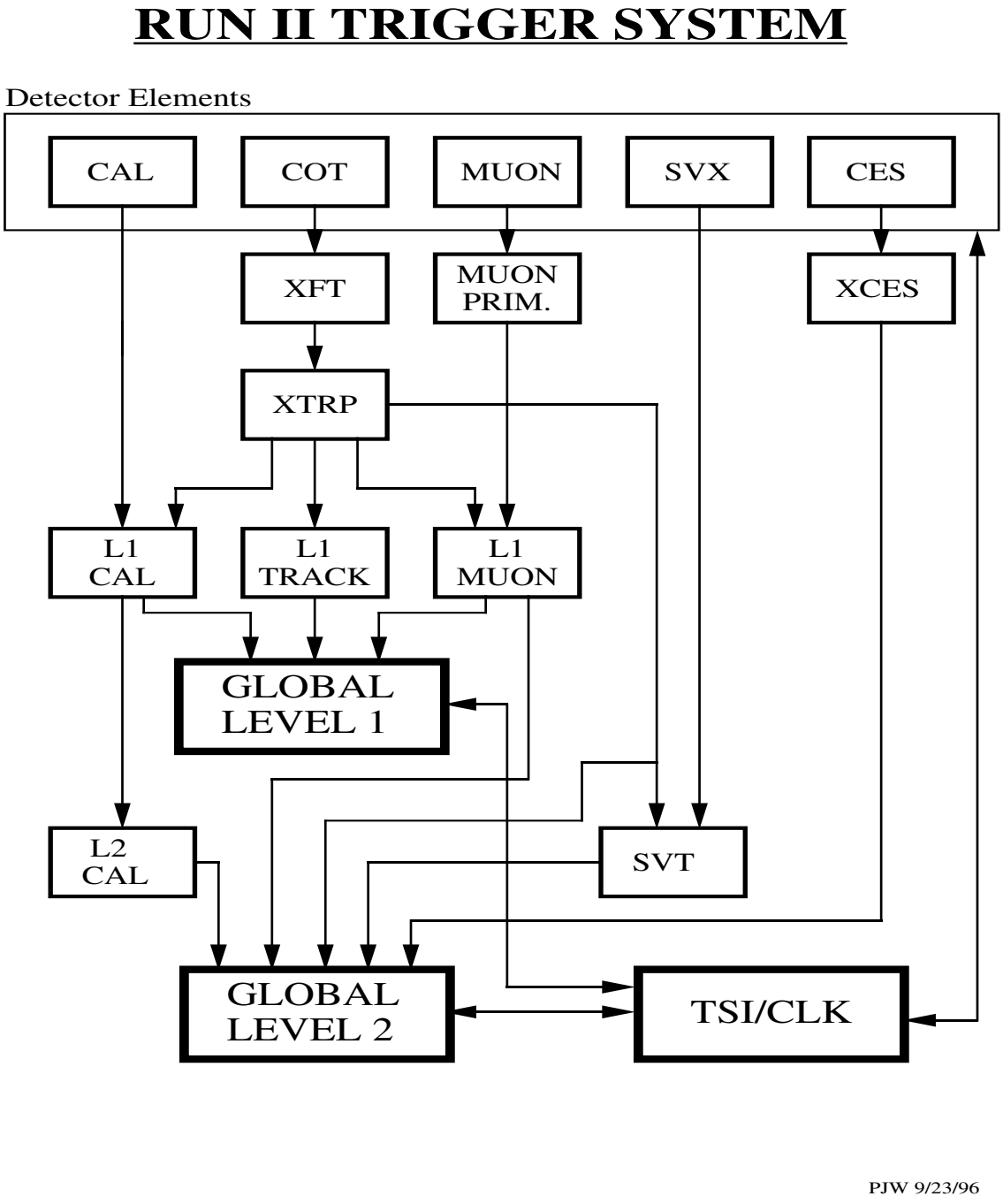

Figure 5.8: Functional block diagram of the L1 and L2 trigger system.

process. For example, an ideal jet algorithm should be insensitive to soft and/or collinear parton emissions to be applied in a straightforward way to fixed-order or resummed QCD calculations, particles or partons from a Monte Carlo event generator, or detector data [26].

The electron and photon identification starts with the tower cluster in the calorimeter : the algorithm is a seeded clustering algorithm [27]. In CEM, the EM cluster starts with a seed tower with at least 3 GeV of transverse electromagnetic energy. The neighouring two towers in the same wedge can be added as shoulders if they have transverse electromagnetic energy above the threshold (100 MeV).The clustering algorithm in the plug is a different one [28].

The tower clusters are associated to the CES, CPR clusters and tracks, if they exist, to form EM objects. Photons are distinguished from electrons typically by requiring that there is no reconstructed tracks pointing to the tower cluster.

Muon stubs are formed using hits in the muon chambers, and are linked to COT tracks for indentifying muon candidates.

Part III

Data Analysis

Chapter 6

The Analysis

Photons detected by the Central Electromagnetic calorimeter (CEM) are utilized in the analysis. In this chapter, the data analysis method is presented - starting with a brief description of the photon ID variables, then the data and MC samples are described. After the evaluations of efficiencies of the event selections, the background from neutral mesons (e.g π^0, η) decaying to multiple photons are classified with a statistical method.

6.1 Photon Identification

In the CEM, photons are identified as a combination of

- energy deposition spread over 2-3 EM calorimeter towers,
- a cluster at shower maximum found by CES,
- and possibly (if they have converted in the solenoidal coil), large amount of charge collected by the CPR, the preshower detector.

The detector components outside the tracking volume that are important for photon detection are sketched in Fig. 6.1, and the variables to identify photons are described as follows:

- Isolation : defined by the sum of the energy in the towers within a 0.4 cone around the photon minus the photon energy. The isolation is required to be less than 1 GeV in this analysis. This cut is very effective in reducing background from neutral mesons such as π^0's since they are almost always embedded in hadronic jets.

- No-track : It is required that there should be no track with p_T above 500 MeV pointing to the calorimeter tower cluster, to remove electrons from the data sample.

- No extra CES cluster : It is required that there should be no extra cluster above 1 GeV in the CES associated to the EM object to reduce neutral meson background.

- CES χ^2 : The shower shape measured by the CES is compared with the standard profiles from test beam . The χ^2 [34] from the comparison is a good handle for suppressing the background of neutral mesons. The χ^2 is required to be less than 20 in the event selection. The χ^2 distribution is further used for estimating the remaining background contamination from neutral mesons.

- CPR charge : If the photon converted in the solenoid coil, the CPR will collect large amount of charge from the charged particles ionizing the gas. For the $\pi^0 \rightarrow \gamma\gamma$ background, when the π^0 carries very large transverse momentum, the two photons from the decay are almost collinear to each other in the lab frame, so that the shower shape at the CES is not distinguishable from that of a single photon. However, the probability for the CPR to observe a conversion in the solenoidal coil is higher than a single photon. This fact is used to estimate the neutral meson background contamination at high E_T region.

- Had/EM : defined by the ratio of the energy deposited in the hadronic sector to that in the electromagnetic sector. This cut is used to suppress jet background. It is required that the ratio to be less than $0.055+0.00045*E^{\gamma}/GeV$; the scaling with the energy of the photon is to allow more energy leaking into the hadronic sector for energetic photons to ensure high detection efficiency.

6.2 Data Sample

This analysis utilizes a data sample collected during the Tevatron Run II period of February 2002 - September 2003. The run numbers range from 138425 to 168889. At CDF, there is a database recording the operational status of the detector: each detector component is assigned a bit in the database which can be set to 1(good) or 0(bad). In order to ensure a good photon detection efficiency, the good run bits for the Central Calorimeter, Shower-Max and COT are required [30].

The integrated luminosity of the data sample is 207 pb^{-1}.

The dataset for this analysis is collected by the low p_T di-photon trigger [29] : DI_PHOTON_12. The trigger requirements at each level are described as follows :

- Level 1 : The EM E_T of a single trigger tower is required to be above 8 GeV. The organization of trigger towers is listed in detail in [25]. In the central calorimeter, one trigger tower consists two adjacent towers in the same wedge. The granularity is approximately $\Delta\eta \times \Delta\phi \approx 0.2 \times 15^\circ$.

- Level 2 : An EM clustering algorithm called "PACMAN" is carried out by L2CAL (a hardware cluster finder), which combines trigger towers with non-trivial energy to form clusters. Each cluster starts with a trigger tower above "seed threshold" (8 GeV) and includes all towers above "shoulder threshold" (7.5 GeV) to form a contiguous region around the seed tower. [1]

  For each cluster, five "isolations" are formed by the L2ISO hardware. The definition of the five isolations are described in detail in [33]. In brief, they are

[1] This clustering potentially causes a long turn-on for high p_T electron triggers. An alternative clustering algorithm is proposed and implemented to L2 alpha processors [31]. The proposed algorithm finds clusters of "pass 0" clusters provided by hardware cluster finder, which are single trigger towers above 2 GeV, with the hadronic to EM energy ratio below 1/8. Another feature is that the algorithm doesn't allow the cluster to expand over different wedges, which is OK for the central because there is a crack of 1° between the adjacent wedges, and the EM objects sit across wedges are not considered in the offline reconstruction because the energy can not be well-determined. But there is no cracks in the plug calorimeter.

Ray Culbertson, Steve Kuhlmann, Jonathan Lewis and Yanwen Liu have studied the application of this algorithm for the plug calorimeter. It is concluded that the shoulder towers in adjacent wedges are important in the plug. In the real implementation, the expansion across wedges is allowed in plug calorimeter [32].

Had/EM $< 0.055 + 0.00045 \times E^{\gamma}/\text{GeV}$
$0.5(\chi^2_{wire} + \chi^2_{strip}) < 20.$
Corrected Isolation < 2 GeV

Table 6.1: List of the quality cuts which are used at L3 for photon triggers. χ^2_{wire} and χ^2_{strip} are the χ^2 of fitting the showermax profiles of wire and strip view respectively with standard profiles obtained from test beam data [34], the χ^2 cut is employed for central EM objects only.

the energy sums of the towers surrounding the seed or the seed plus a shoulder. The illustration of five sums is showin in Fig. 6.2. The minimum of the five sums is used by the triggers as a cut variable.

In the DI_PHOTON_12 path, the L2 trigger requires two EM clusters, each with EM $E_T > 10$ GeV, hadronic to EM energy ratio below 1/8, and the minimum of the five isolations below 3 GeV or the ratio to the EM cluster E_T less than 15%.

- Level 3 : A full event reconstruction is made in real time at L3. The photon triggers place a requirement on the quantities of the reconstructed EM objects [27], with the z vertex set to zero. In the DI_PHOTON_12 trigger, the L3 filter requires two EM objects to have EM $E_T > 12$ GeV, and each of them passing the quality cuts as shown in Table. 6.1.

The cross section of the DIPHOTON_12 is approximately 1 nb, see Fig. 6.3. Events collected by the inclusive photon trigger (PHOTON_25_ISO), which requires only one photon candidate have E_T above 25 GeV and satisfy the quality cuts in Table 6.1, are used to evaluate the trigger efficiency of the diphoton trigger. For each event with two photon candidates in the inclusive photon sample, the fraction of events that have the diphoton trigger bit on is shown in Fig. 6.4 as a function of the EM E_T of the second hardest photon candidate in the event. This fraction can be interpreted as the efficiency for one leg of a diphoton event fulfilling the trigger requirement because PHOTON_25_ISO trigger utilizes exactly the same quality cuts as the DIPHOTON_12 does per leg.

The definition of trigger efficiency is the probability of a signal event passing the trigger requirement. The sample used here to evaluate the trigger efficiency is a mixture of signal and background events, including background from high p_T neutral mesons (such as π^0, η, K_s^0) that decay to multiple photons, with the decay products boosted close to each other in the lab frame, and consequently reconstructed as a single EM object. The selection cuts are varied within a fairly large range to esimate the systematic uncertainty. The most sensitive cuts that control the background fraction are the isolation cuts : calorimeter isolation and extra shower-Max cluster energy cut. They are both varied from 1 GeV to 2 GeV in the trigger study. Both cuts are placed at 1 GeV in the event selection of this analysis. The fraction of events having the diphoton bit on is found to vary by 1%. This variation, and the error returned from the fitting in Fig. 6.4 are included in the systematic uncertainty, which contributes an uncertainty of 3% to the final cross sections.

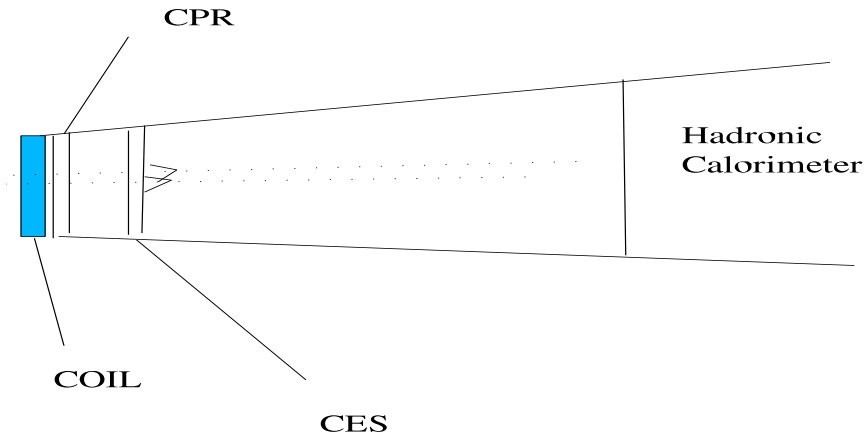

Figure 6.1: An illustration of the detector components outside the tracking volume at CDF II that are important for photon detection(not-to-scale). The solenoid coil is used as the preradiator by the preshower detector (CPR) mounted in front of the EM calorimenter towers immediately outside the magnet. A 2-dimensional multi-wire proportional chamber (CES) is embedded at the shower maximum at six radiation lengths. The two dotted lines illustrate two photons from neutral meson decay, which generate two clusters at the CES.

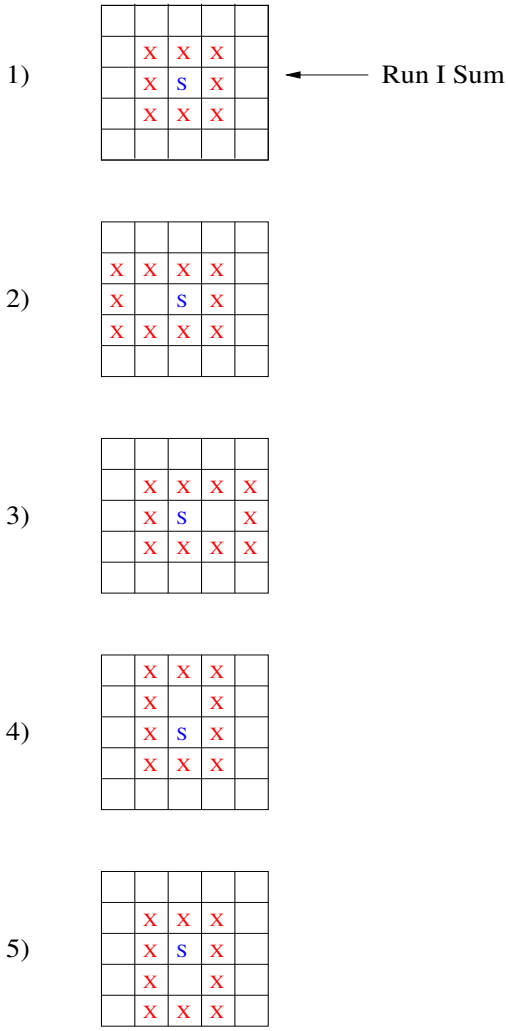

Figure 6.2: The five isolation sums [33]; ϕ is increasing upward, and η is increasing to the left. 'S' denotes the seed tower. Labelled with 'X' are the towers included in the isolation sum. The first sum is the one used in the CDF Run I triggers.

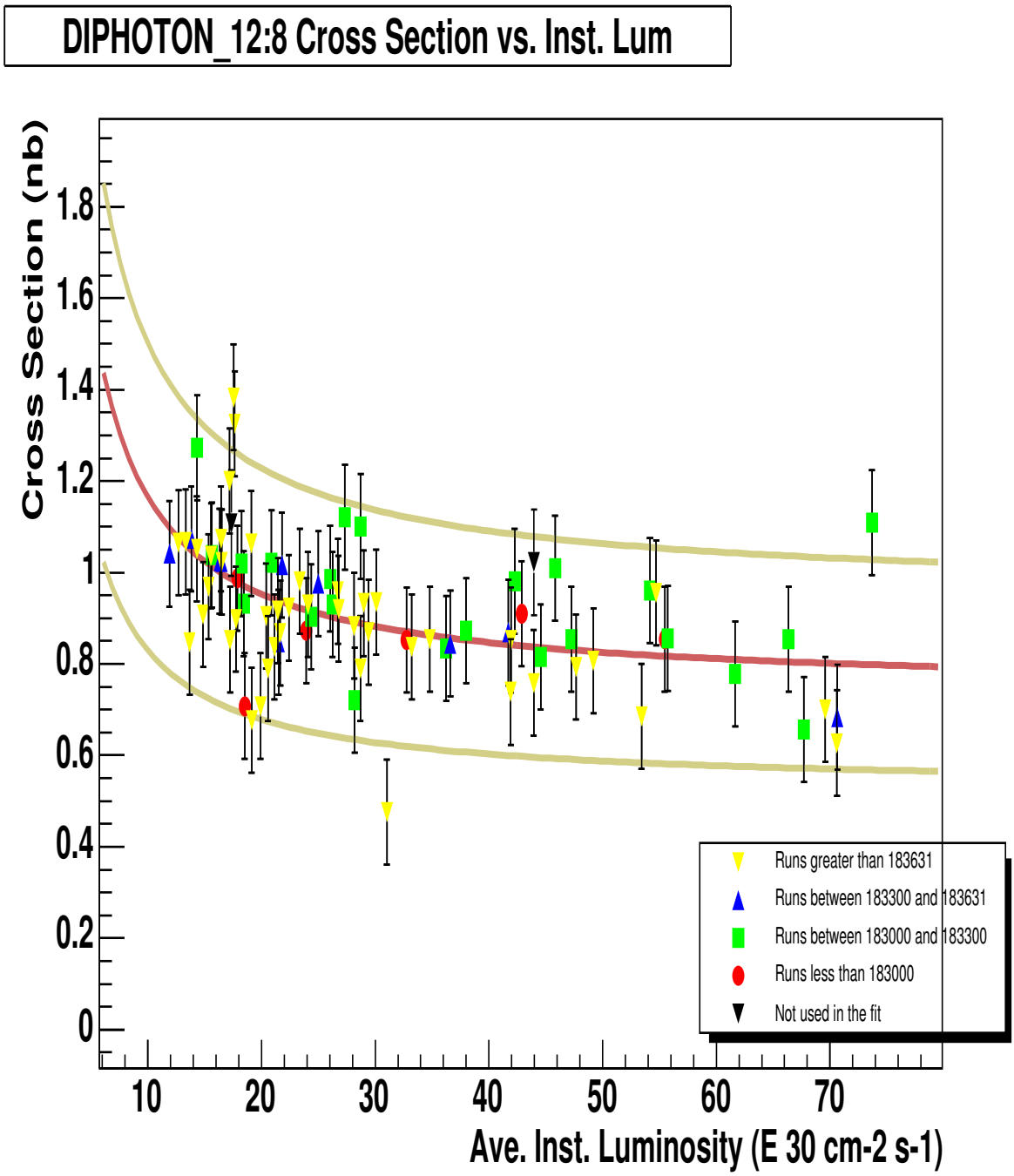

Figure 6.3: The DIPHOTON_12 trigger cross section [35].

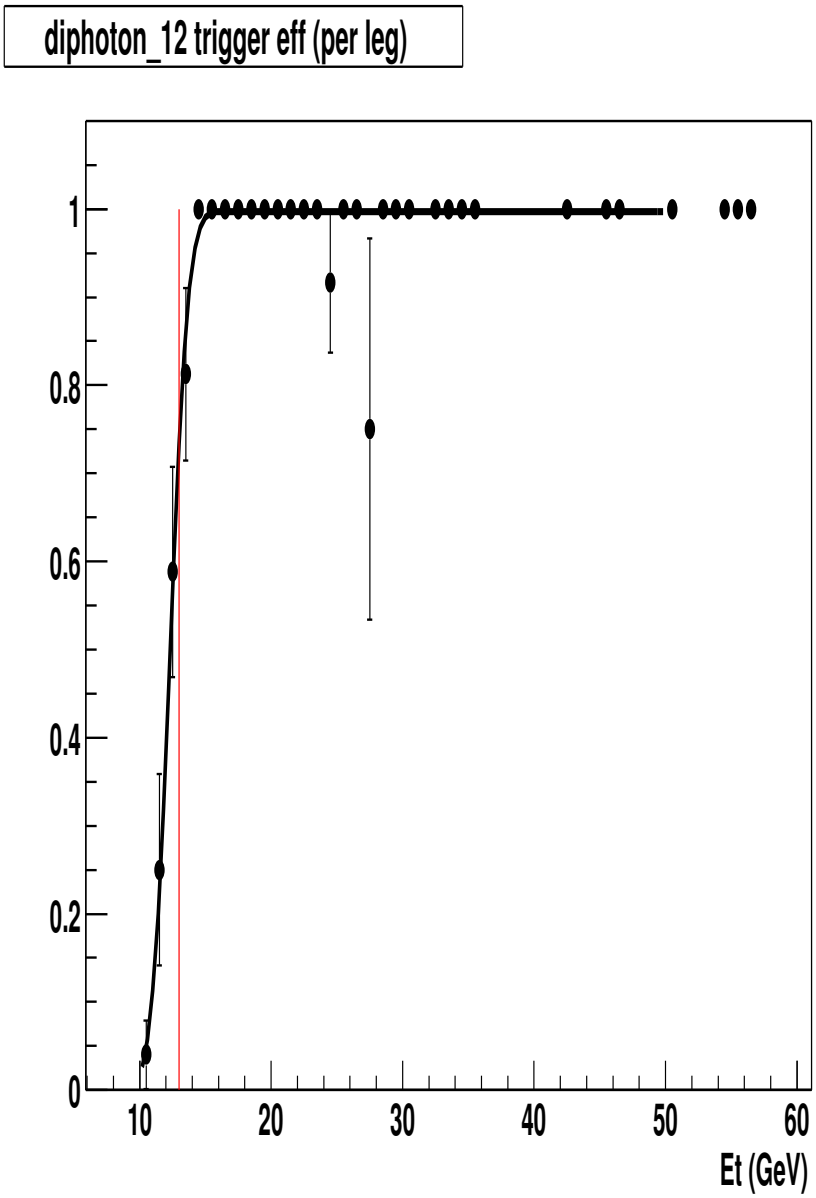

Figure 6.4: DI_PHOTON_12 efficiency (per leg) vs. EM E_T (GeV), parameterized as $p0 * Erfc(p1 * (p2 - Et))$ (fitted parameters are : p0 = 4.98695e-01 ± 6.56155e-03, p1= 6.49414e-01 ± 1.14311e-01, p2 =1.23154e+01 ± 2.06161e-01) to unweight data points. Numerator : diphoton_12 trigger bit. Denominator : photon_25_iso trigger bit and two isolated photon candidates in the CEM. See text for details. The red line is at 13 GeV.

6.3 Monte Carlo Samples

A $\gamma\gamma$ Monte Carlo sample is generated by PYTHIA [37], and fully simulated with CDF detector simulation [39] to estimate the detector acceptance, and selection efficiencies. The parameter set of "Tune A" [38] is adopted to describe the effect of underlying events, including initial state radiation (ISR) and activities of beam-beam remnants. The dataset identifier (ID) of the MC sample is "pexo2d". The sample corresponds to an integrated luminosity of 4.9 fb^{-1}.

Two other PYTHIA samples are generated to help understanding the systematics. One is generated using "Tune B" [38] for the description of underlying events. The other is generated with the effects of initial state and final state radiations turned off. Both samples are fully simulated with detector simulation.

6.4 Event selection

The offline cuts are the same as in the Run I analysis [36], except for the E_T threshold. The Run I diphoton analysis had 10 GeV as the E_T trigger threshold, 12 GeV threshold at the offline to avoid trigger inefficiency caused by E_T smearing. In Run II, the trigger threshold is $E_T > 12$ GeV. An offline threshold of 13 GeV is used to avoid the region where the trigger is very inefficient. The E_T cut on the leading photon is increased to 14 GeV to make the E_T cuts asymmetric because the NLO predictions are unstable if the E_T threshold on the two legs are set to the same value (see Chapter 3). The selection cuts are listed in Table 6.2. In succeeding sections, some explanations on the cut variables are provided, and the efficiencies are evaluated. The E_T and rapidity cuts are used to specify the phase space of interest. The same cuts are applied to theoretical cross section calculations for the comparisons with data. Photons in the plug calorimeter are not considered in this analysis.

6.4.1 Detector Acceptance

The detector acceptance is evaluated with diphoton Monte Carlo events in the official sample (pexo2d), by checking how often there is an offline EM object matching to

Central with $\|\eta\| < 0.9$
$E_T^{\gamma 1} > 14$ GeV and $E_T^{\gamma 2} > 13$ GeV
Fiducial, i.e, |Xces|< 17.5 cm and 14 cm <|Zces| < 217 cm
Isolation in 0.4 cone < 1 GeV.
No extra CES cluster above 1 GeV
No 3D track pointing to the EM cluster
|Z-Vertex| <60 cm
Average CES $\chi^2 < 20$
Had/EM < 0.055 + 0.00045*E/GeV

Table 6.2: Event selection cuts.

the prompt photons at generation level. For the generation level and offline particle matching, the offline photon is required to be within 0.4 cone in the $\eta - \phi$ plane around the photon at generation level, and the energy difference to be within 50%. The matching efficiency is plotted vs. η, ϕ in Fig 6.5 and Fig 6.6 respectively. The central acceptance is calculated to be 0.880 per photon by averaging the matching efficiency vs. η plot for η between -0.9 and 0.9 region.

The matching efficiency becomes 0.650 after the fiducial requirements, namely |Xces| <17.5 cm, 14 cm < |Zces| < 217 cm, to exclude the uninstrumented detector regions at the edges of the CES, where

- $Zces$ is the z position of the photon measured by the CES strips, using the CDF global coordinate (see the description in section 5.1);
- $Xces$ is the photon position measured by the CES wires, using a local coordinate with the origin ($x = 0$) at the center of the wedge (see Fig. 5.5).

The matching efficiency is plotted vs. the diphoton mass, q_T and $\Delta\phi$ in Fig. 6.7, Fig. 6.8, Fig. 6.9 respectively, in order to check the independence of the acceptance on the kinematics variables and the correlation of the two photons. The acceptance is found to be constant as a function of the diphoton mass, q_T and $\Delta\phi$, with negligible correlation.

The same studies are carried out with the other two PYTHIA samples in order to estimate the uncertainty on the acceptance. The PYTHIA sample with ISR turned

off is expected to be inappropriate to describe the data because the kinematics of the di-photon final state is very sensitive to the initial state radiations. Shown in Fig. 6.10 is the $\Delta\phi$ between the two photons. Without ISR, the two photons of the final state are mostly absolutely back-to-back in the x-y plane. If one of the photons is located in the uninstrumented region, most likely so is the other, i.e there is a correlation introduced : the acceptance is 0.656 $\pm$0.004(stat) for the first photon, 0.649$\pm$0.004 for the the second [2]. However, the probability for both photons at generation level to have a matching EM object in the fiducial region is 0.466$\pm$0.004. We also notice the mean q_T of this 'unphysical' PYTHIA sample is only 1.2 GeV, in contrast with 7.7 GeV in the official PYTHIA sample (pexo2d). The effect of turning off the initial and final state radiations is too dramatic to be used to evaluate the uncertainty on the acceptance. A reasonable approach is to use the difference between "tune A" and "tune B" [38]. The acceptance evaluated from the Tune B PYTHIA sample is 0.421$\pm$0.003. Compared with $0.650^2 = 0.423$ from the official PYTHIA sample (pexo2d), the difference is negligible .

[2]Since the ordering of the two photons is irrelevant, the photon appears first in the PYTHIA event record is called the first photon.

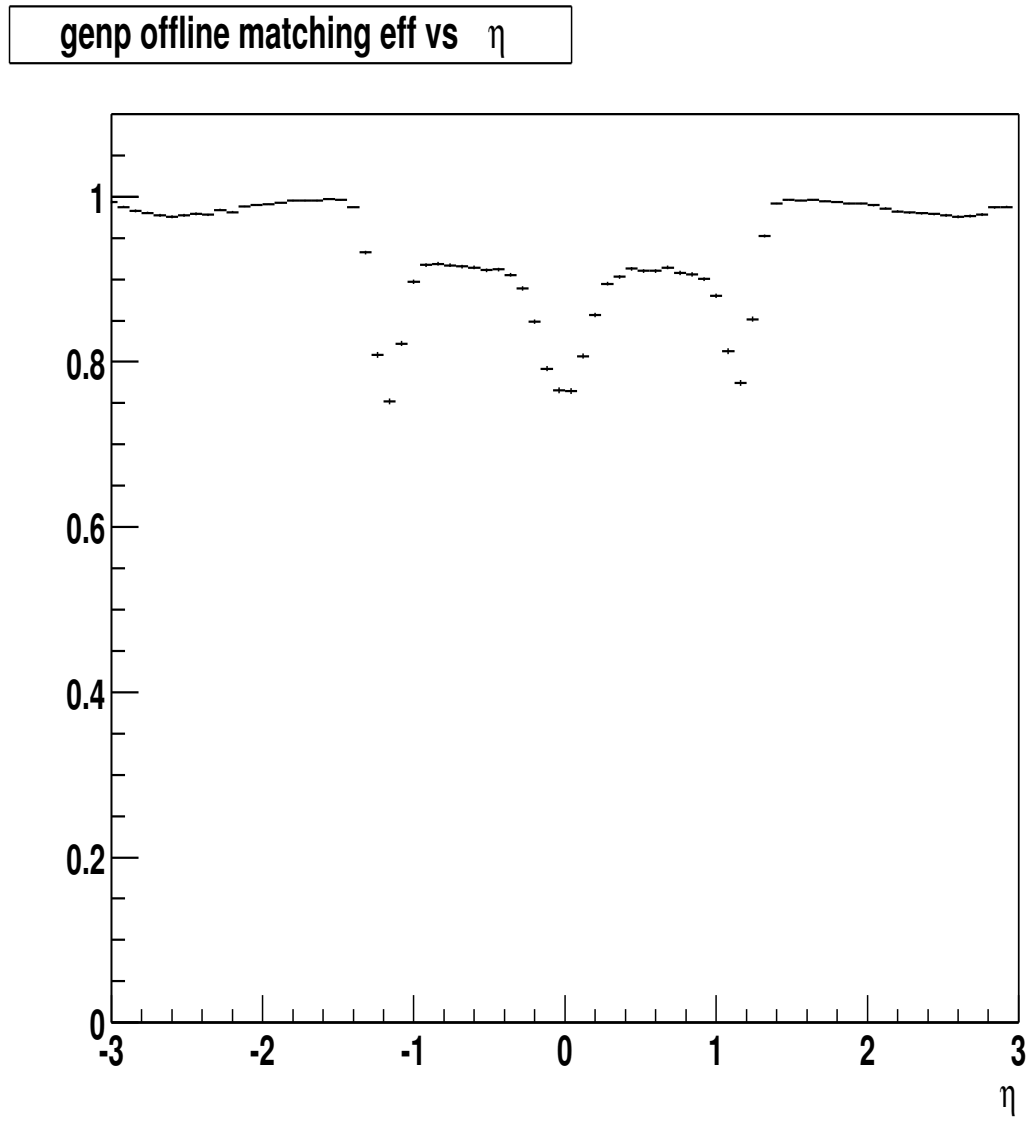

Figure 6.5: The efficiency of matching generation level photons to offline reconstructed photons vs. η from diphoton PYTHIA MC. Each event contributed two entries since there are two prompt photons in it.

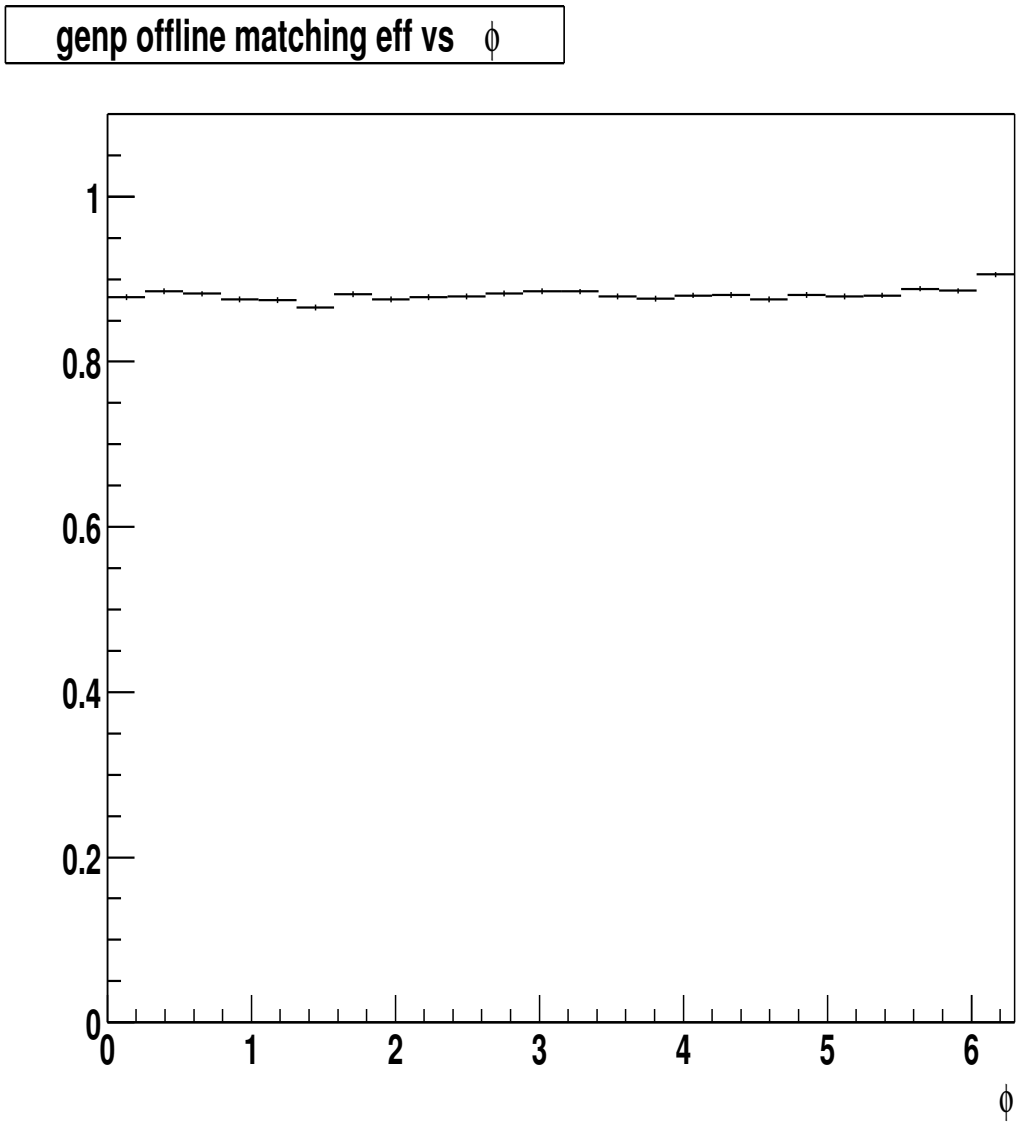

Figure 6.6: The efficiency of matching generation level photons to offline reconstructed photons vs. ϕ, Each event contributed two entries since there are two prompt photons in it.

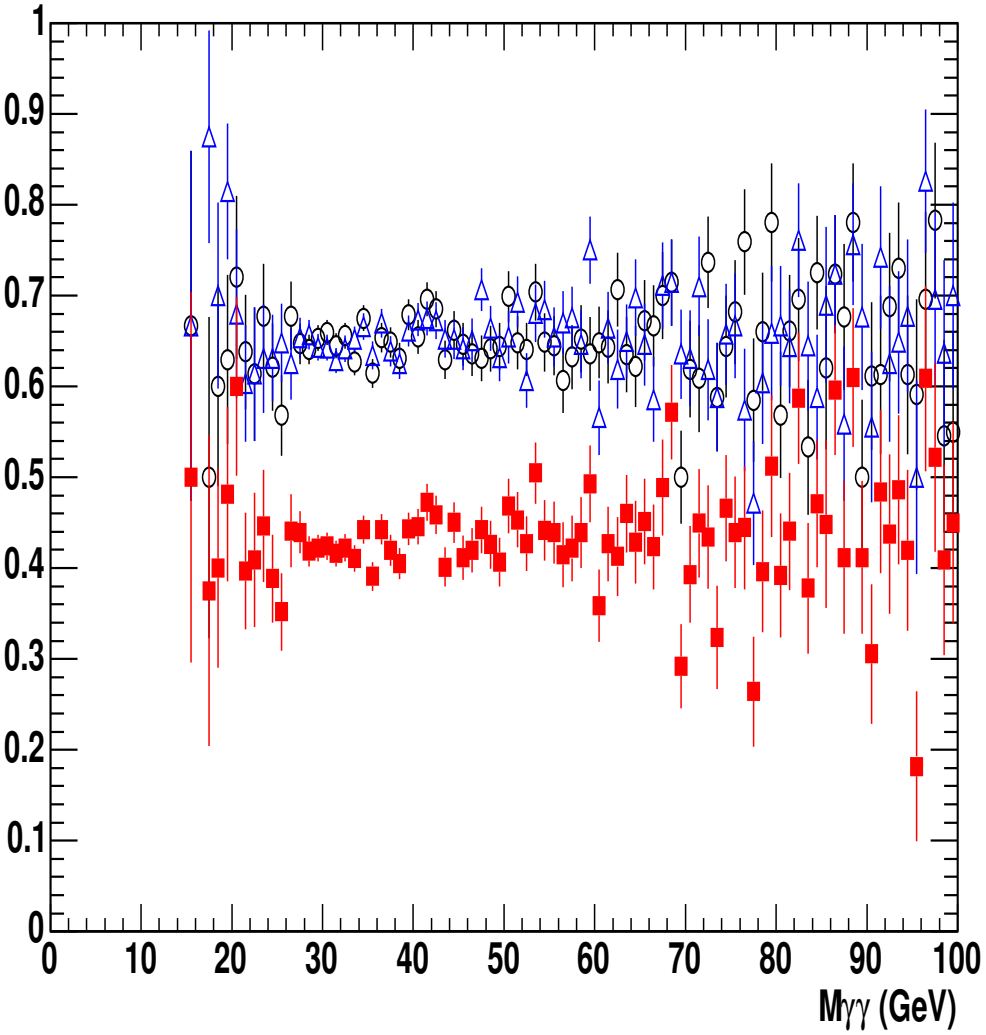

Figure 6.7: The efficiency of matching the generation level photons to offline reconstructed photons vs. diphoton mass. Plotted in red squared dots is the probability for both photons at generation level to have matching photon candidates in the fiducial detector region at offline level, in black circles and blue triangles the efficiency for each of the photons. We fit the three curves with horizontal straight lines, the fit values (A) and χ^2's are:
A(circle) = 0.652, with $\chi^2/ndf = 91/83$;
A(triangle) = 0.653, with $\chi^2/ndf = 88/83$;
A(square) = 0.428, with $\chi^2/ndf = 112/83$.
The correlation of the acceptance between the two photons is negligible.

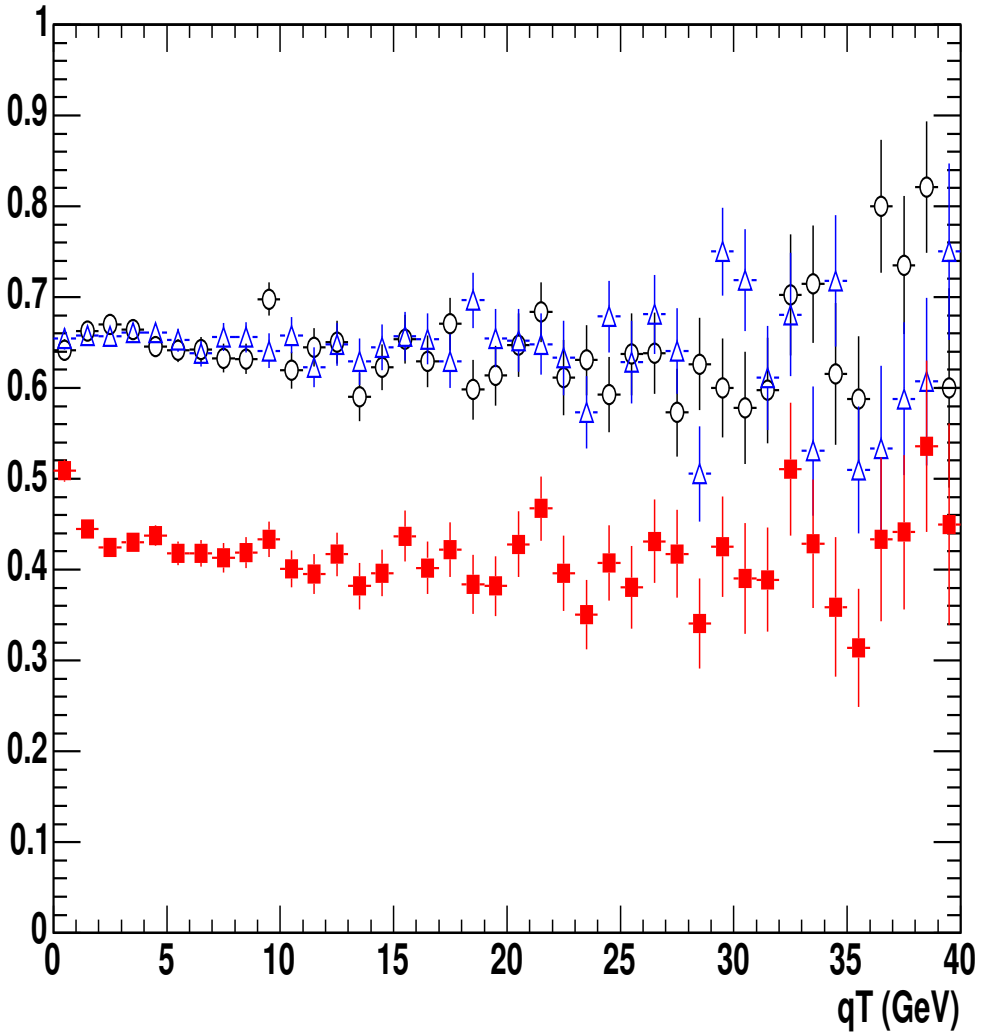

Figure 6.8: The efficiency of matching the generation level photons to offline reconstructed photons vs. diphoton q_T. Plotted in red squares is the probability for both photons at generation level to have matching photon candidates at offline level, in black circles and blue triangles the efficiency for each of the photons.

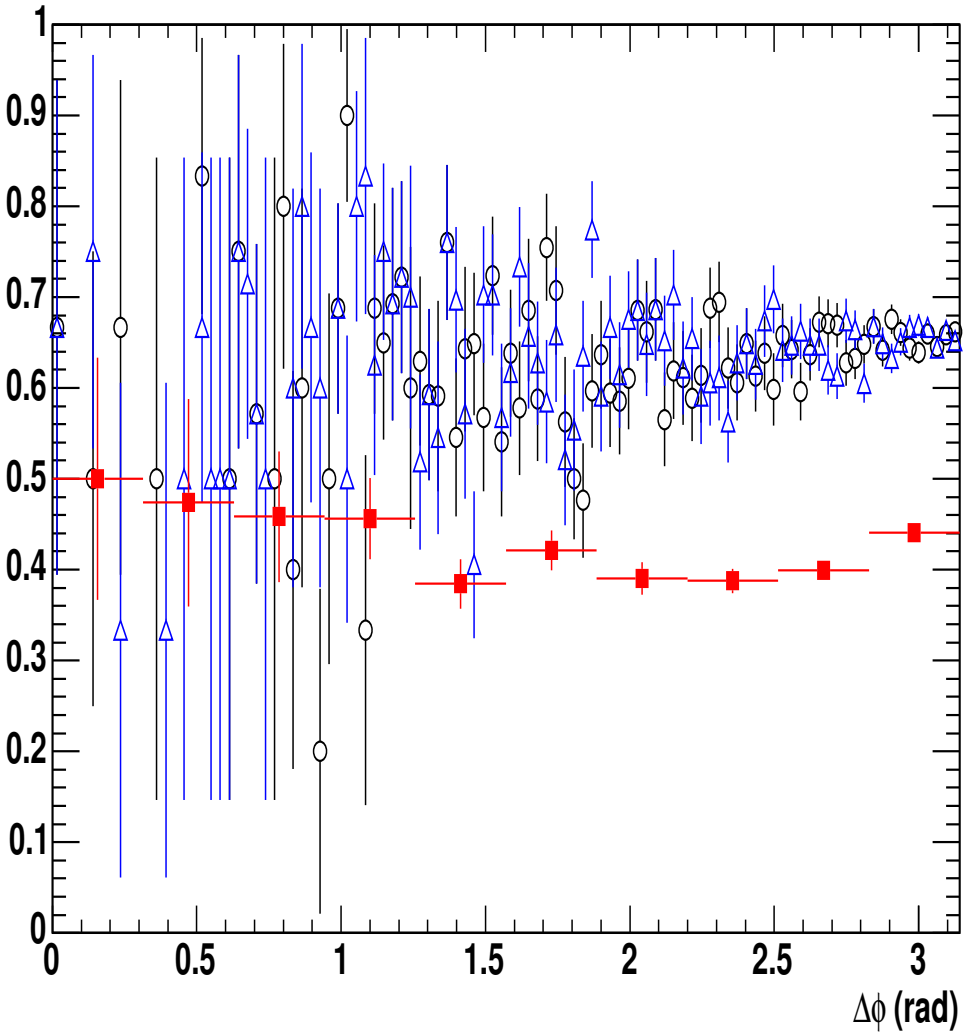

Figure 6.9: The efficiency of matching the generation level photons to offline reconstructed photons vs. diphoton $\Delta\phi$. Plotted in red squares is the probability for both photons at generation level to have matching photon candidates at offline level, in black circles and blue triangles the efficiency for each of the photons.

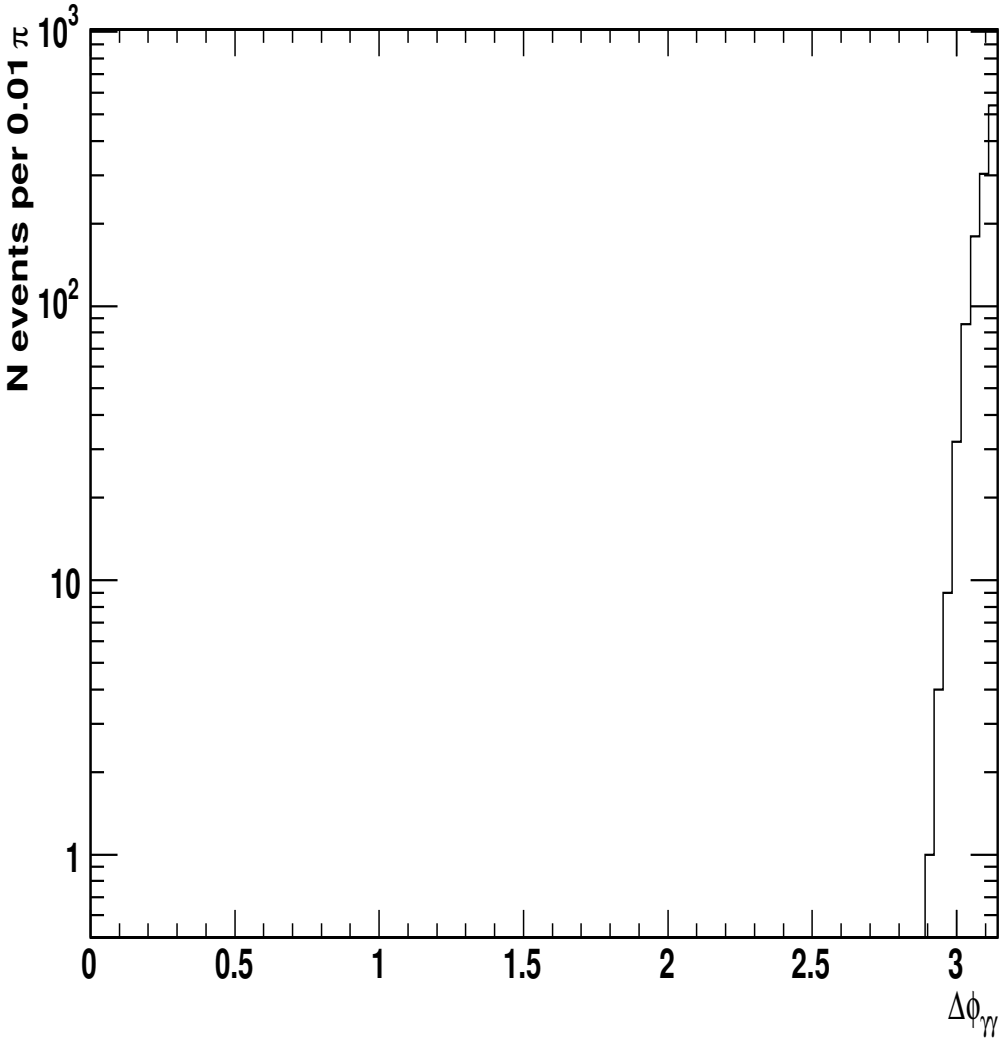

Figure 6.10: Diphoton $\Delta\phi$ from PYTHIA MC with ISR turned off.

6.4.2 Isolation

The isolation in an $\eta - \phi$ cone of 0.4 is required to be less than 1.0 GeV for each photon. Plotted in Fig. 6.11 is the isolation distribution of prompt photons from the diphoton Monte Carlo (pexo2d). The efficiency of the 1.0 GeV cut is found to be 0.867 per photon.

As was done in the Run I analysis [36], the isolation efficiency is verified by randomly placing virtual EM clusters(flat in η, ϕ) on minimum bias events, and calculating the isolations. For the virtual EM clusters, 0.864 (0.876) of the two- (three-) tower clusters have isolation below 1 GeV. The isolation efficiency from PYTHIA MC(pexo2d) is in-between the two fractions, proving that the calorimeter simulation matches the data fairly well. The 1% disagreement is taken as uncertainty on the isolation efficiency.

It turns out that, with the kinematics cuts ($|\eta| < 0.9$, $E_T^{\gamma 1} > 14$ GeV and $E_T^{\gamma 2} > 13$ GeV), the isolation cut efficiency slightly decreases as the diphoton mass increases, while it appears constant as a function of q_T and $\Delta\phi$. See Fig. 6.12, Fig. 6.13 and Fig. 6.14 .

The isolation < 1 GeV fraction is plotted as a function of photon E_T in Fig. 6.15. The isolation efficiency is constant at small photon E_T, and drops with a small slope at large E_T. The parameterization of the efficiency ε_{iso} as a function of E_T as

$$\varepsilon_{iso}(E_T) = \begin{cases} p0 & E_T < 26GeV \\ p0 + p1 * (E_T - 26)/GeV & E_T \geq 26GeV \end{cases} \tag{6.1}$$

gives the smallest χ^2. The fitted values of the parameters $p0, p1$ are shown in Fig. 6.15.

6.4.3 No-track cut

To eliminate electrons from the data sample, photon candidates with a track pointing to them are rejected. There are two inefficiency issues for this requirement : a good photon will be rejected if there is an underlying track pointing to it, or if the

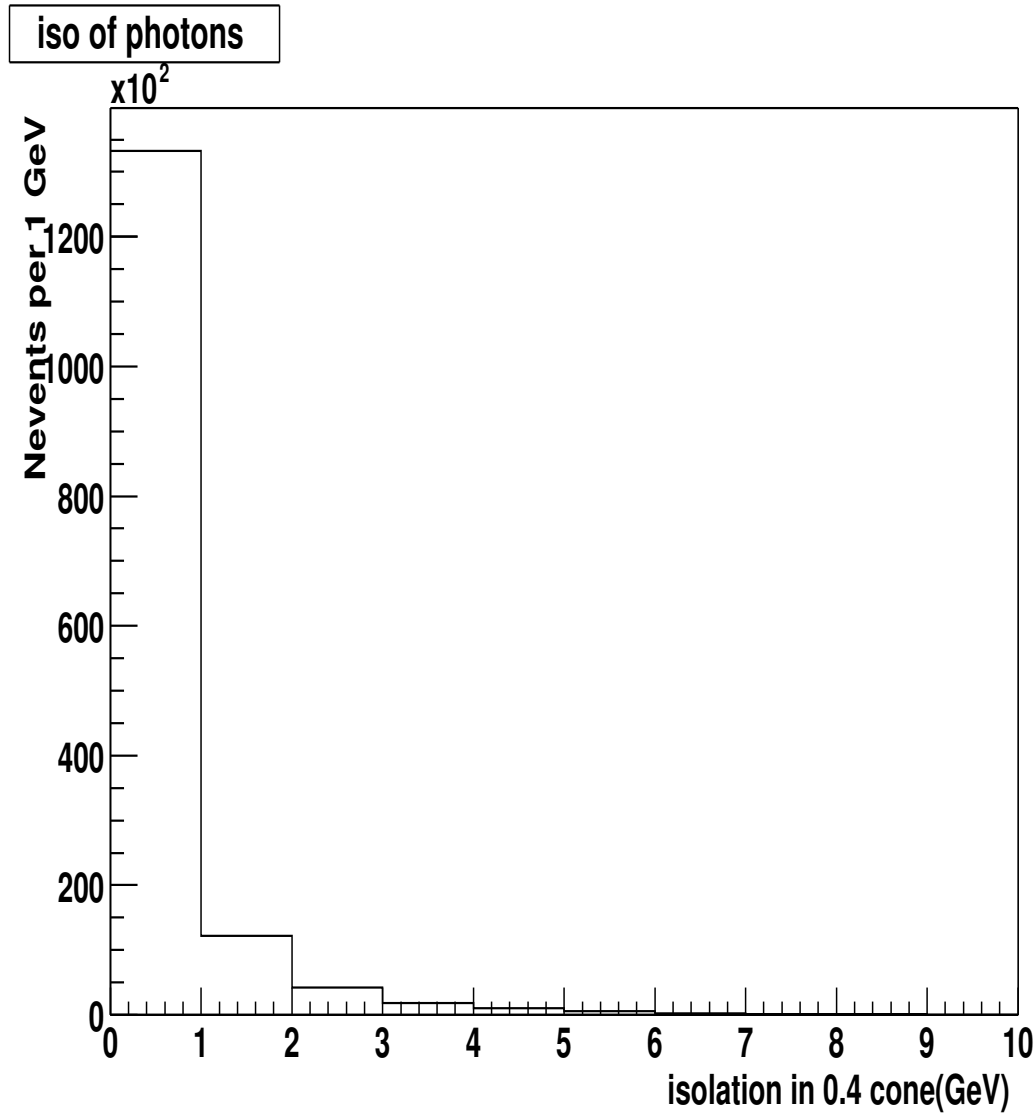

Figure 6.11: isolation in 0.4 cone (GeV) for prompt photons from PYTHIA diphoton MC.

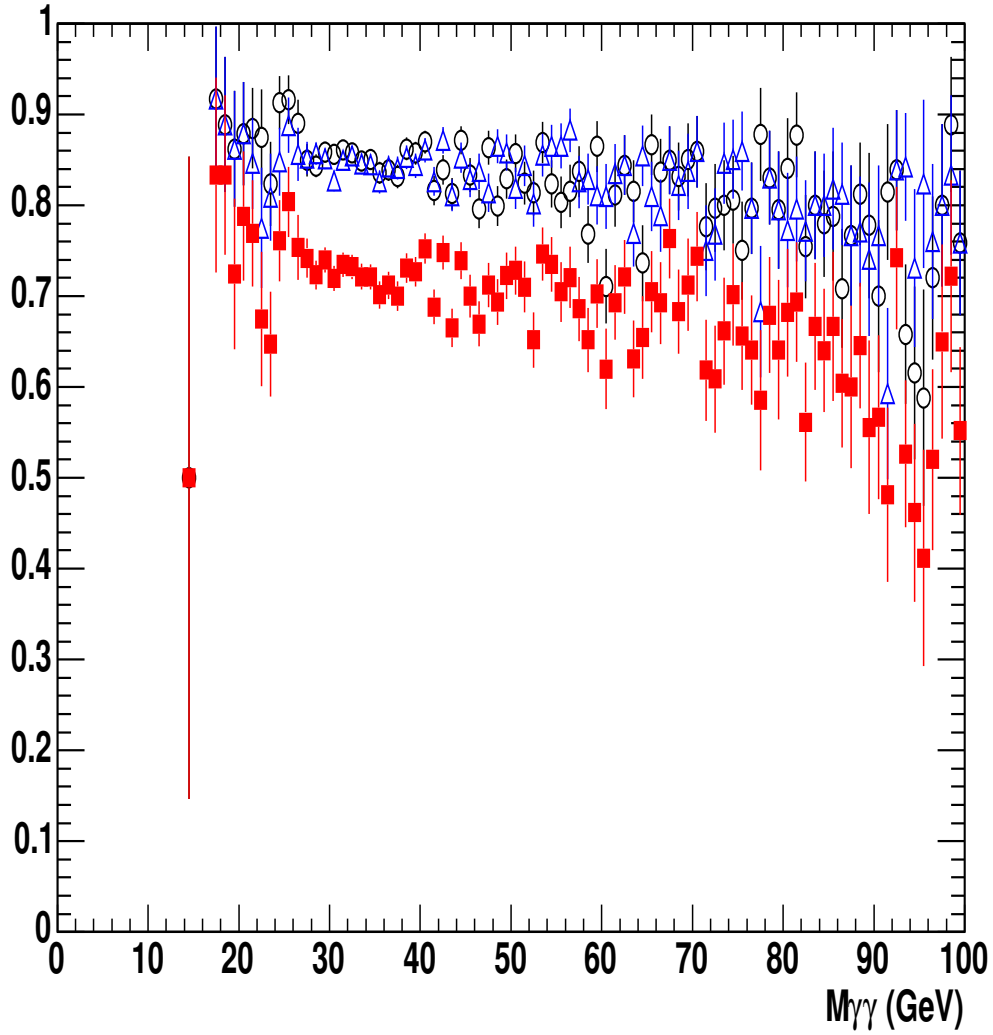

Figure 6.12: The isolation < 1 GeV efficiency as a function of the diphoton mass (in GeV). Plotted in red squares is the probability for both photons passing the isolation cut, in black circles and blue triangles the probability for each of the photons passing the isolation cut. We fit the 3 curves with flat straight lines and the fit values (ε) and χ^2's are:
ε(circles) $= 0.838$, with $\chi^2/ndf = 151.1/83$;
ε(triangles) $= 0.834$, with $\chi^2/ndf = 126.1/82$;
ε(squares) $= 0.703$, with $\chi^2/ndf = 197.7/83$.
The χ^2/ndf's are too large to justify a constant isolation efficiency for any mass.

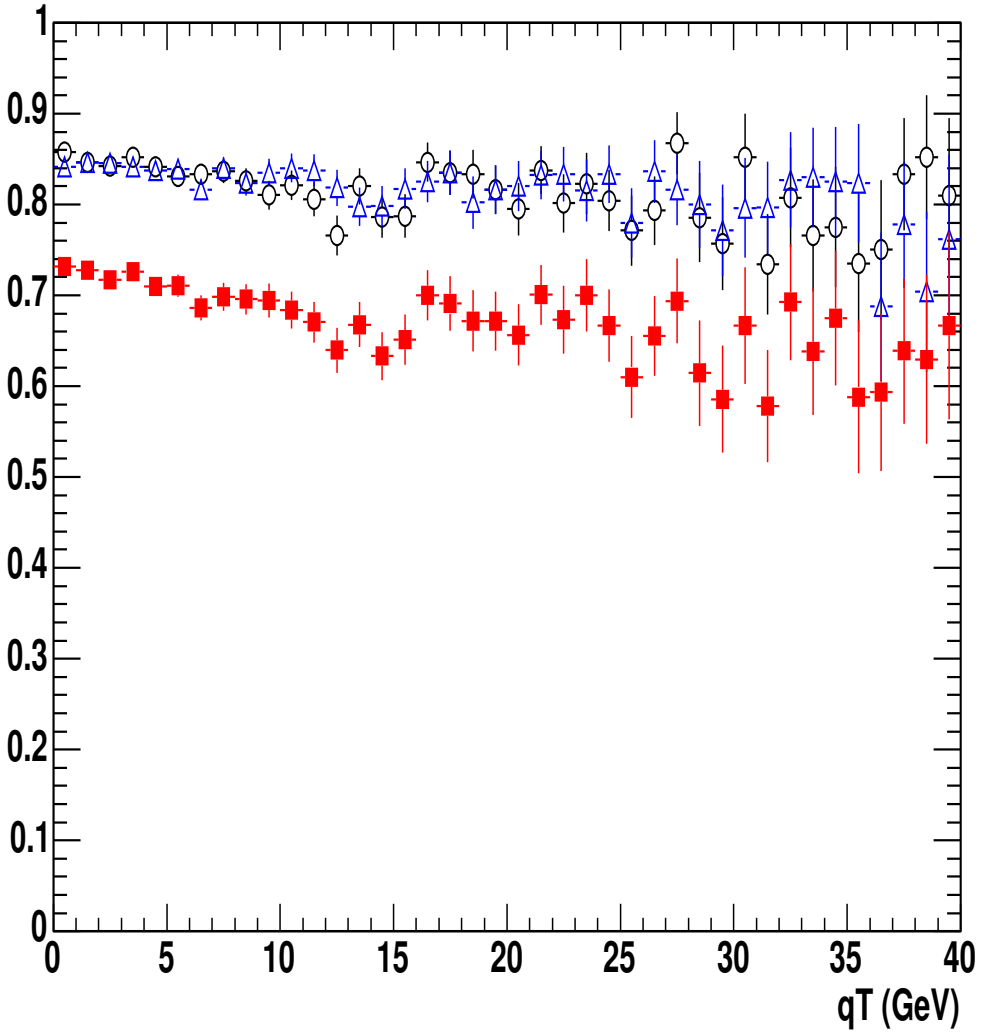

Figure 6.13: The isolation < 1 GeV efficiency as a function of the diphoton q_T (in GeV). Plotted in red squares is the probability for both photons passing the isolation cut, in black circles and blue triangles the probability for each of the photons passing the isolation cut.

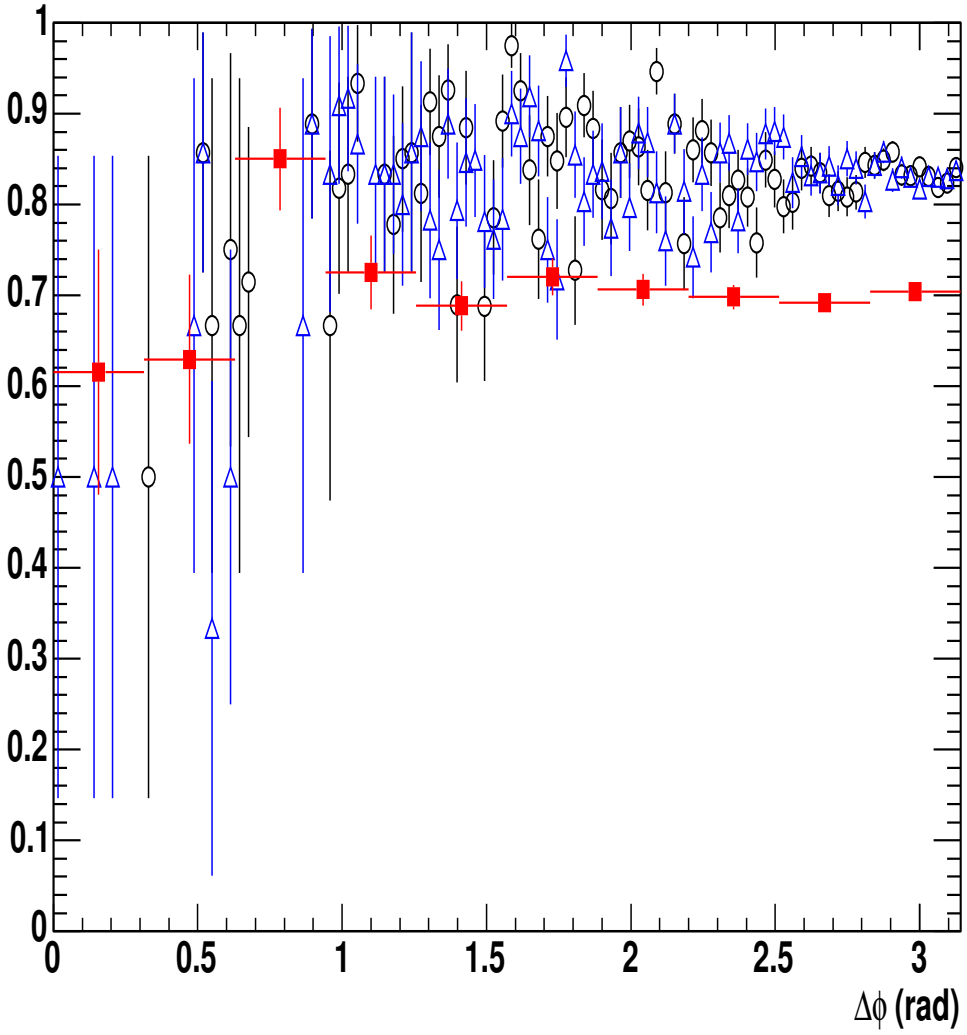

Figure 6.14: The isolation < 1 GeV efficiency as a function of the diphoton $\Delta\phi$ (in rad). Plotted in red squares is the probability for both photons passing the isolation cut, in black circles and blue triangles the probability for each of the photons passing the isolation cut.

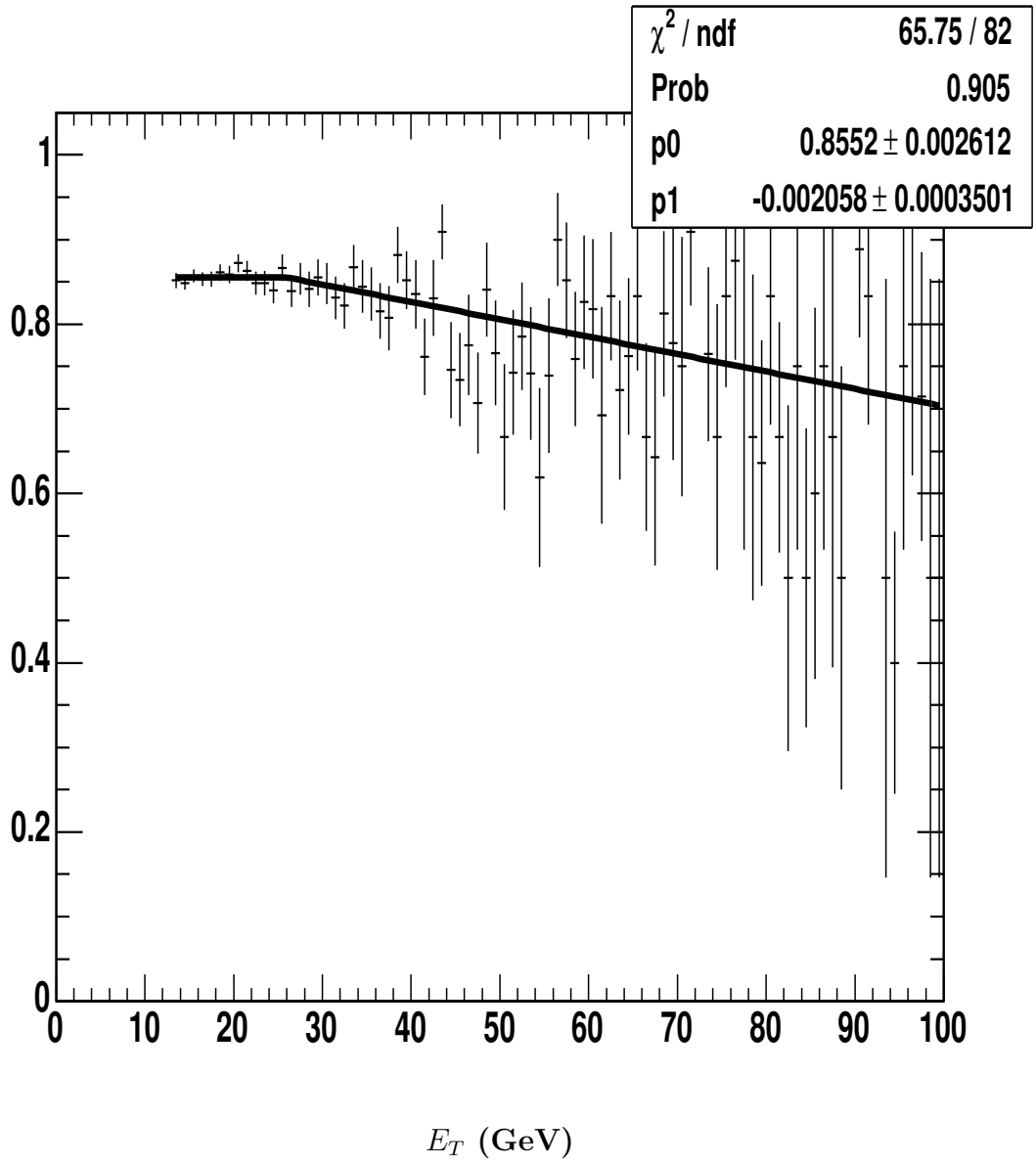

Figure 6.15: The isolation < 1 GeV efficiency as a function of the photon E_T (in GeV), from the diphoton PYTHIA sample (pexo2d).

photon has converted in tracking volume to cause a reconstructed track. The track multiplicity of prompt photons in the diphoton MC (pexo2d) is shown in Fig 6.16. From that plot, the no-track cut efficiency is evaluated to be 0.862 per photon. The probabilities for each of the two photons in the MC sample passing the no-track cut and for both passing the cut are plotted as functions of the diphoton mass, q_T and $\Delta\phi$ in Fig. 6.17, 6.18 and 6.19 respectively.

It has been noted in [40] that the material amount is underestimated in the simulation of the version with which the pexo2d sample is generated and that the no-track cut efficiency from MC should be reduced by a factor of 0.97. ($0.862 \times 0.97 = 0.836$). To be sure, the two efficiency issues are studied separately in alternative ways. Firstly, the conversion probability is determined by material amount. The conversion probability for photons in central region in the MC sample (pexo2d) is evaluated to be 0.141 after having applied the correction for additional material [40]. Secondly, the inefficiency caused by underlying tracks is measured with virtual EM clusters randomly superimposed on minimum bias events : virtual clusters are randomly placed, and every track with p_T above 0.5 GeV is extrapolated to the CES radius to check how often there would be at least one track associated with the virtual EM cluster according to the EM object cluster-track matching algorithm. A fraction of 0.933 of the virtual EM clusters do not have an associated underlying track. The total efficiency is (1-0.141)*0.933 = 0.801, which differed from what we got from diphoton MC(0.836) by 4%. This disagreement is included in the estimate of the systematic uncertainty.

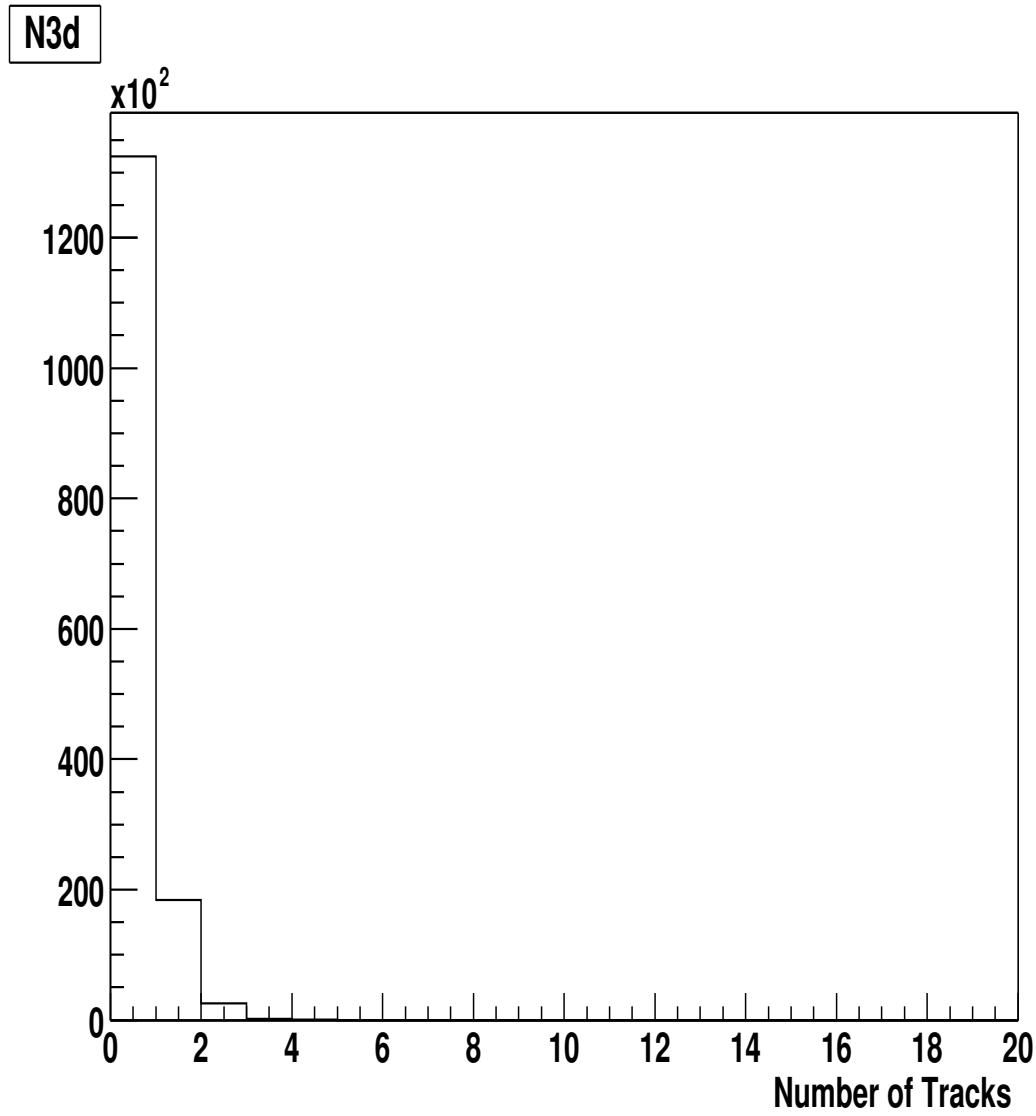

Figure 6.16: Track multiplicity of prompt photons in diphoton PYTHIA MC.

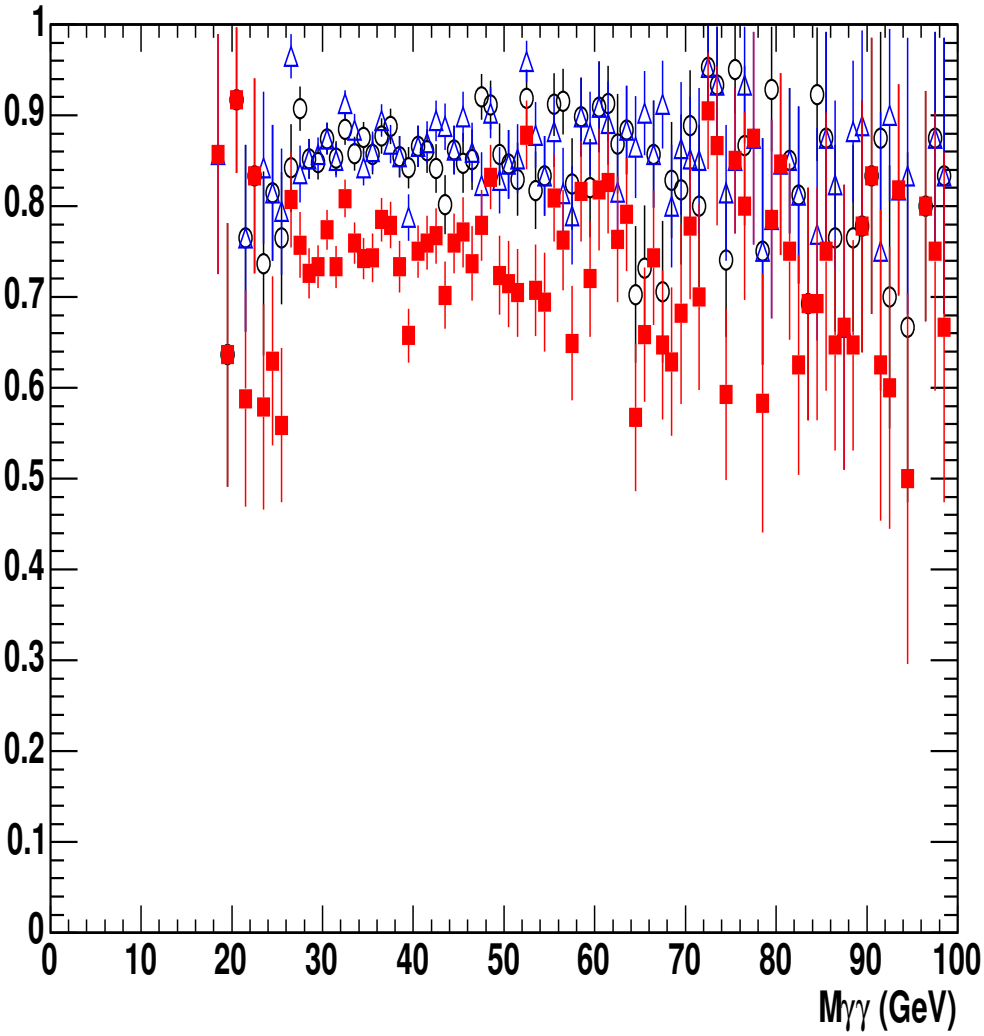

Figure 6.17: No-track cut efficiency as a function of the diphoton mass. Plotted in red squares is the probability for both photons passing the no-track requirement, in black circles and blue triangles the probability for each of the photons passing the cut.
We fit the three curves with flat straight lines, the fitted efficiencies ($\varepsilon_{no-track}$) and the χ^2's are:
$\varepsilon_{no-track}(circles) = 0.865$, with $\chi^2/ndf = 66.3/80$;
$\varepsilon_{no-track}(triangles) = 0.870$, with $\chi^2/ndf = 104.6/81$;
$\varepsilon_{no-track}(squares) = 0.751$, with $\chi^2/ndf = 92.6/82$.

The correlation of the probabilities for each of the two photons passing the no-track cut is negligible.

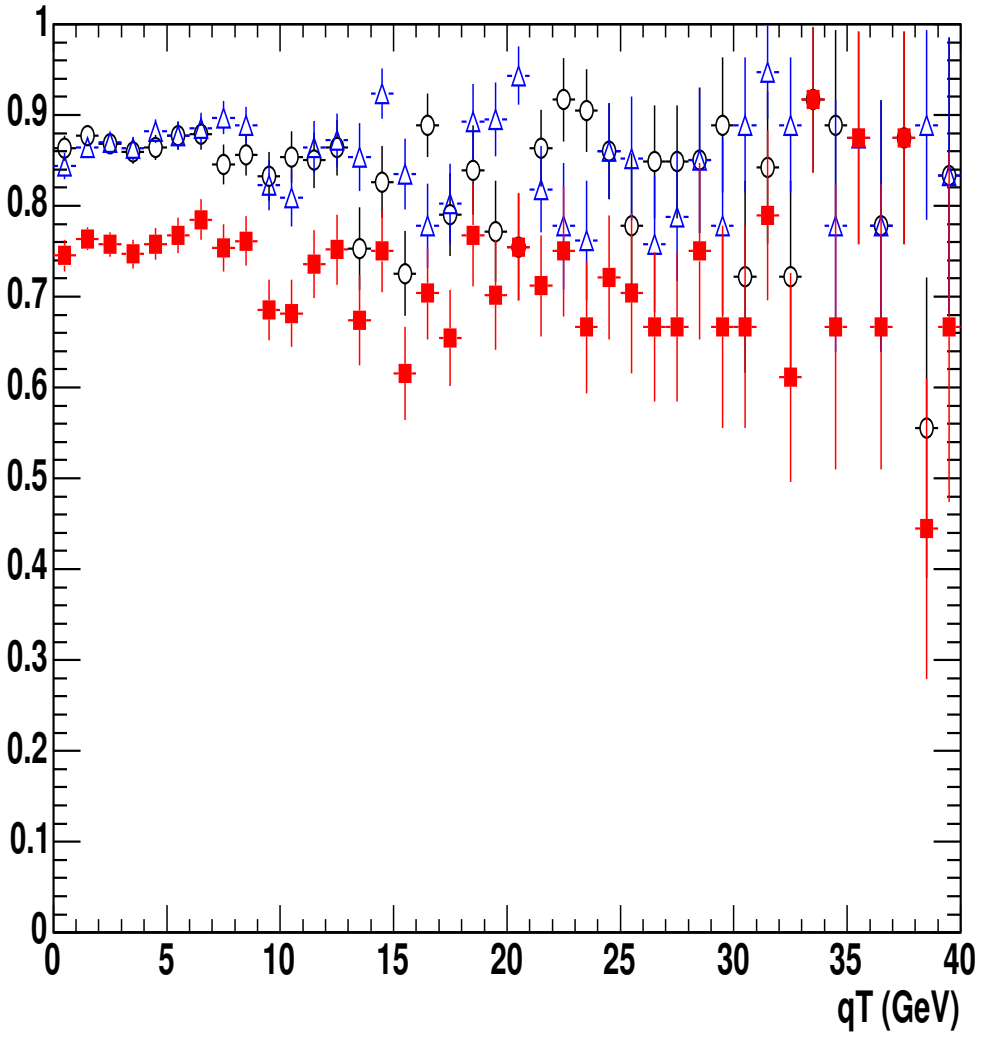

Figure 6.18: No-track cut efficiency as a function of the diphoton q_T. Plotted in red squares is the probability for both photons passing the no-track requirement, in black circles and blue triangles the probability for each of the photons passing the cut.

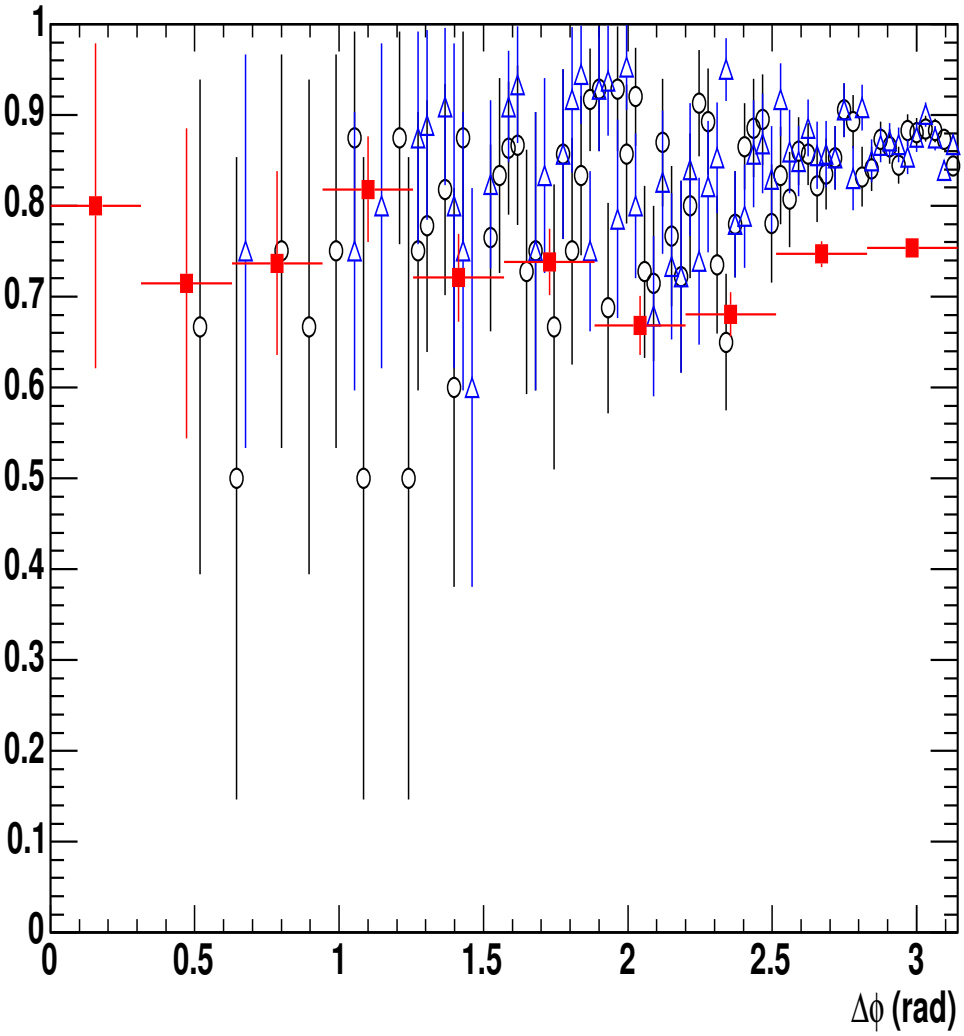

Figure 6.19: No-track cut efficiency as a function of the diphoton $\Delta\phi$. Plotted in red squares is the probability for both photons passing the no-track requirement, in black circles and blue triangles the probability for each of the photons passing the cut.

6.4.4 No extra CES cluster

It is required that there should be no extra CES cluster above 1 GeV for each of the two photons. The main motivation of this cut is to suppress the neutral meson background, such as π^0's.

The efficiency of this cut is measured with the diphoton MC to be 0.894. Since the CES simulation is not a detailed GEANT [41] simulation, a cross check is conducted using the inclusive electron data sample. The method is described as follows: a Z$\rightarrow$ *ee* peak is reconstructed using tight electron identification cuts for one leg, and very loose cuts (only those quality cuts listed in Table 6.1) for the other leg. Under the Z mass peak, the second legs form an electron sample of very high purity with the minimum selection bias. The electron sample is referred as "the unbiased Z legs".

A tight E/p cut (requiring it to be between 0.9 and 1.1) is placed on the unbiased Z legs to reduce the bremsstrahlung effects. After the E/p cut, the no-extra CES cluster above 1 GeV cut efficiency is evaluated to be 0.908$\pm$ 0.008, which agrees well with the efficiency from the diphoton MC sample.

The efficiency of the no-extra CES cluster above 1 GeV cut is correlated to that of the no-track and isolation cuts. With the diphoton MC sample (pexo2d), the no-extra CES cluster above 1 GeV cut efficiency increases to 0.948 per photon, (which is used later for cross section calculations) when the prerequisite of the isolation $<$ 1 GeV and no-track cuts is imposed. The efficiency of no-extra CES cluster above 1 GeV cut plotted as a function of the diphoton mass, q_T and $\Delta\phi$ in Fig 6.20, 6.21, 6.22.

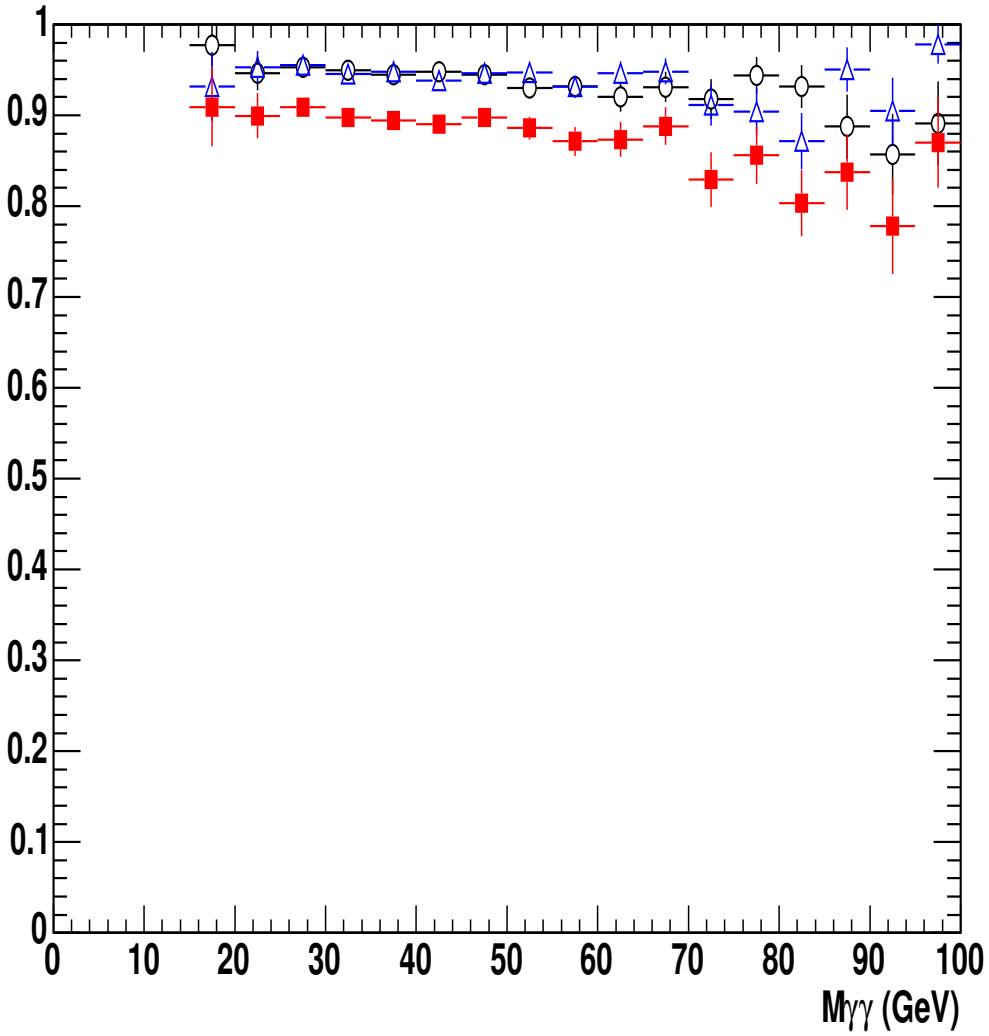

Figure 6.20: The efficiency of no-extra CES cluster cut as a function of the diphoton mass. Plotted in red squares is the probability for both photons passing the no-extra cluster requirement, in black circles and blue triangles the probability for each of the photons passing the cut. No-track and isolation cuts are imposed as prerequisite. We fit the three curves with flat straight line, the fitted efficiencies ($\varepsilon_{no-extraCES}$) and the χ^2's are:
$\varepsilon_{no-extra\,CES}(squares) = 0.948$, with $\chi^2/ndf = 71.9/72$;
$\varepsilon_{no-extra\,CES}(triangles) = 0.948$, with $\chi^2/ndf = 73.9/73$;
$\varepsilon_{no-extra\,CES}(squares) = 0.897$, with $\chi^2/ndf = 104.2/78$;
(As indicated by the ndf's, the fittings are done with finer binning than what's shown in the plot.)

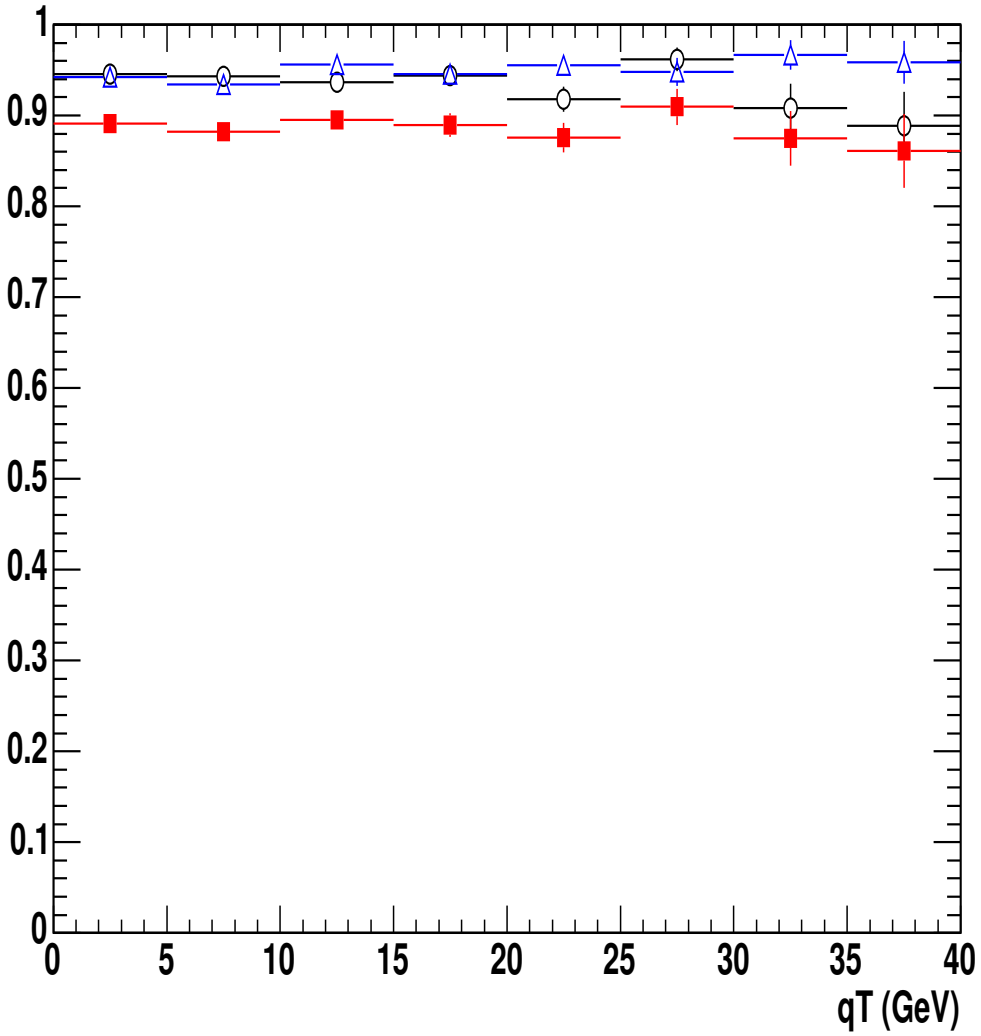

Figure 6.21: The efficiency of the no-extra CES cluster cut as a function of the diphoton q_T. Plotted in red squares is the probability for both photons passing the no-extra cluster requirement, in black circles and blue triangles the probability for each of the photons passing the cut.

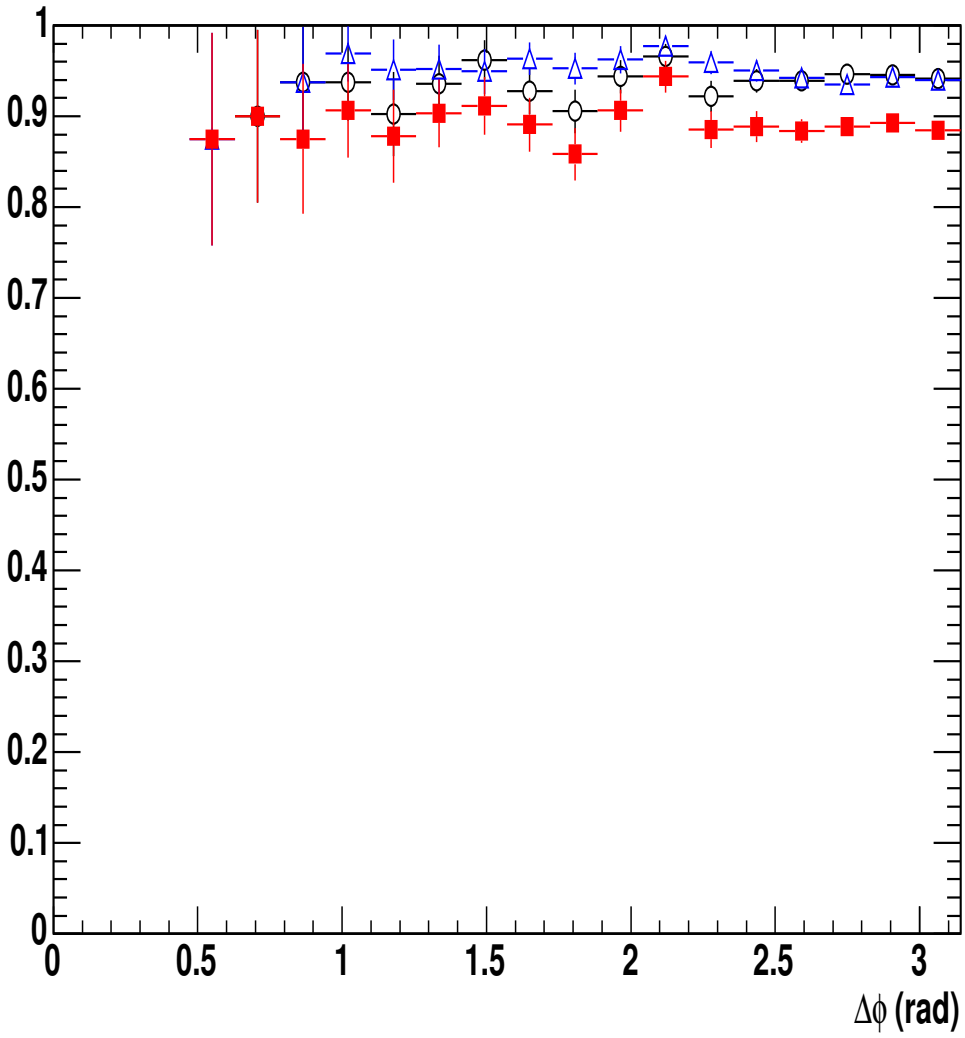

Figure 6.22: The efficiency of the no-extra CES cluster cut as a function of the diphoton $\Delta\phi$. Plotted in red squares is the probability for both photons passing the no-extra cluster requirement, in black circles and blue triangles the probability for each of the photons passing the cut. No-track and isolation cuts are imposed as prerequisite.

6.4.5 Z-Vertex

The Z-Vertex is required to be within 60 cm from the center of the CDF detector. The efficiency of this cut has been measured in [42] to be 0.951. But for the diphoton final state, the vertex finding efficiency should be considered. The OBSP [3] and reconstructed Z-Vertex distributions of diphoton MC events are plotted in Fig 6.23. The Z-Vertex finding efficiency is found to be 0.922. This is cross checked with data. For 628 diphoton candidates in the Run II data sample [4] if the Z-Vertex cut is left out, of which 34 are found with no vertices reconstructed. It is verified that background events have higher vertex finding efficiency by varying the isolation family cuts to change the signal to background ratio. The vertexing efficiency from the 628 candidates (1-34/628 = 0.946) can be taken as the upper limit. It is estimated that there are 325.5 $\gamma\gamma$ events in the sample (see section 6.5). The case that all the 34 candidates with no vertices are $\gamma\gamma$'s corresponds to the lowest vertexing efficiency for diphoton events : 1-34/325.5 = 0.896. The $|Z_{Vertex}|$ <60 cm cut efficiency is evaluated to be 0.951*0.922 = 0.877. Both the lower and upper limit of vertexing efficiency are covered by adding 3% uncertainty to the systematic uncertainty.

6.4.6 CES χ^2 and Had/EM energy ratio

Both cuts, CES χ^2 < 20 and Had/EM < 0.055 + 0.00045*E/GeV, were assumed 100% efficient in the Run I analysis [36]. They are checked with unbiased Z legs(The E/p is required to be between 0.8 and 1.2 to reduce bremsstrahlung effect; and only strip view is sampled for the χ^2 cut). Both cuts are about 99% efficient : 0.988 for the Had/EM cut, 0.985 for the χ^2 cut.

[3] OBSP is the data block in the MC event record that keeps the information of observable particles and the primary interaction vertex of the event.

[4] This is the diphoton sample when there is only 100 pb^{-1} of data collected.

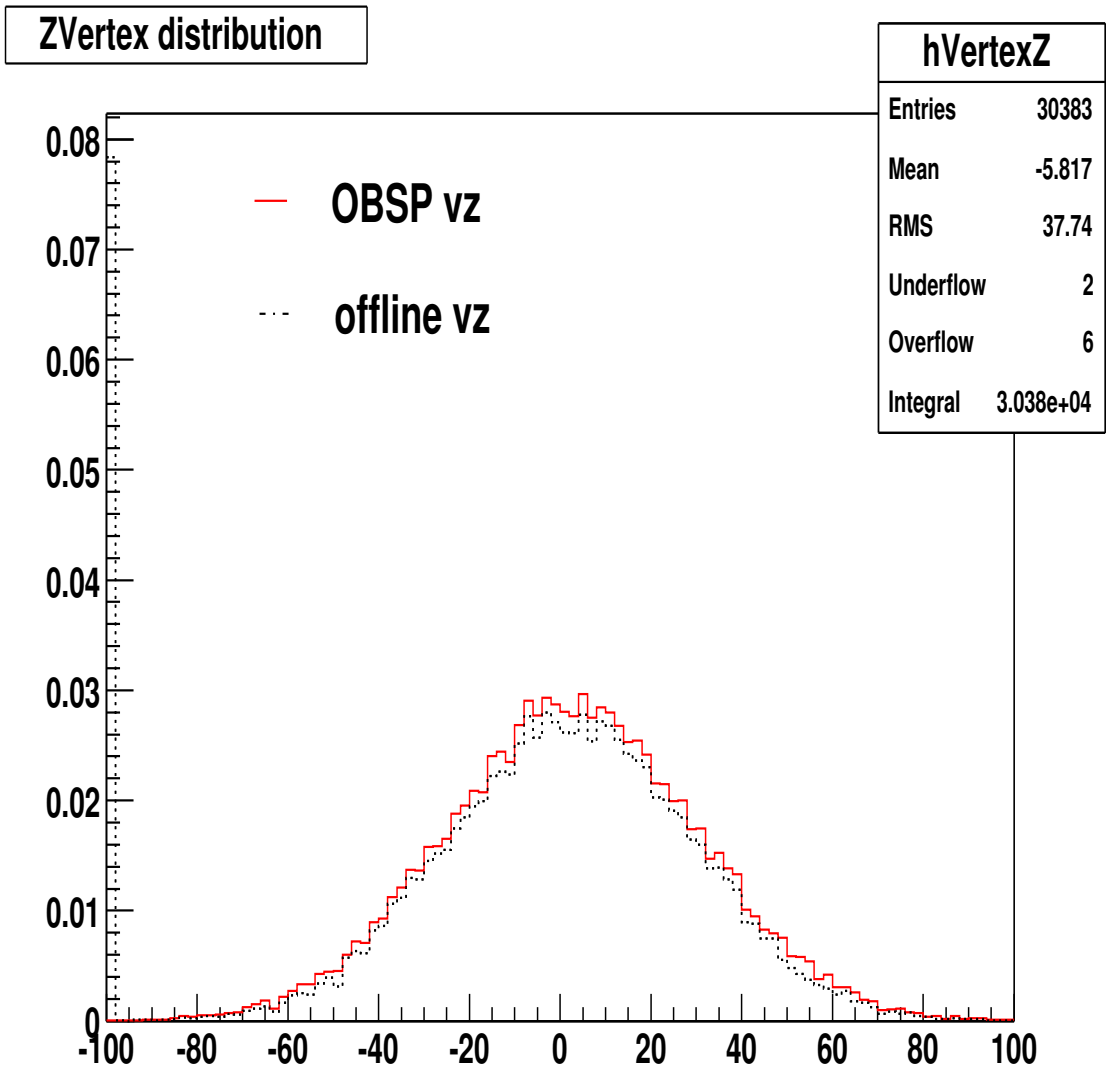

Figure 6.23: Z-Vertex distribution of diphoton MC events : a number of events were found with no vertex reconstructed, and placed at the first bin (zv = -100.0)

	efficiency	contribution to syst uncer
Trigger	0.951	3%
Reconstruction efficiency and fiducial cuts	0.423	negligible
Isolation energy in 0.4 cone < 1 GeV	0.727	2%
No track pointing to the EM cluster	0.699	10%
No extra CES cluster above 1 GeV	0.899	negligible
CES $\chi^2 < 20$	0.970	negligible
Had/EM $<0.055 + 0.00045\times$E	0.976	negligible
$\lvert$z-vertex $\rvert < 60$ cm	0.877	3%
Total	0.152	11%

Table 6.3: The efficiencies for the cuts used in the $\gamma\gamma$ analysis.

6.4.7 Summary

The efficiencies and the contribution to systematic uncertainty from the uncertainties on the efficiencies are summarized in Table. 6.3. The dominant factor is the acceptance due to the 1° cracks between the wedges. The largest systematic uncertainty comes from the no-track cut efficiency, due to the limited knowledge of the material amount of the tracking volume.

The overall detection efficiency is 0.152. The uncertainty is 11% in total.

After these offline cuts, 889 diphoton candidates are left. The invariant mass, the two-body system p_T (q_T) and $\Delta\phi$ distributions are shown in Fig 6.24, Fig 6.25 and Fig 6.26 respectively.

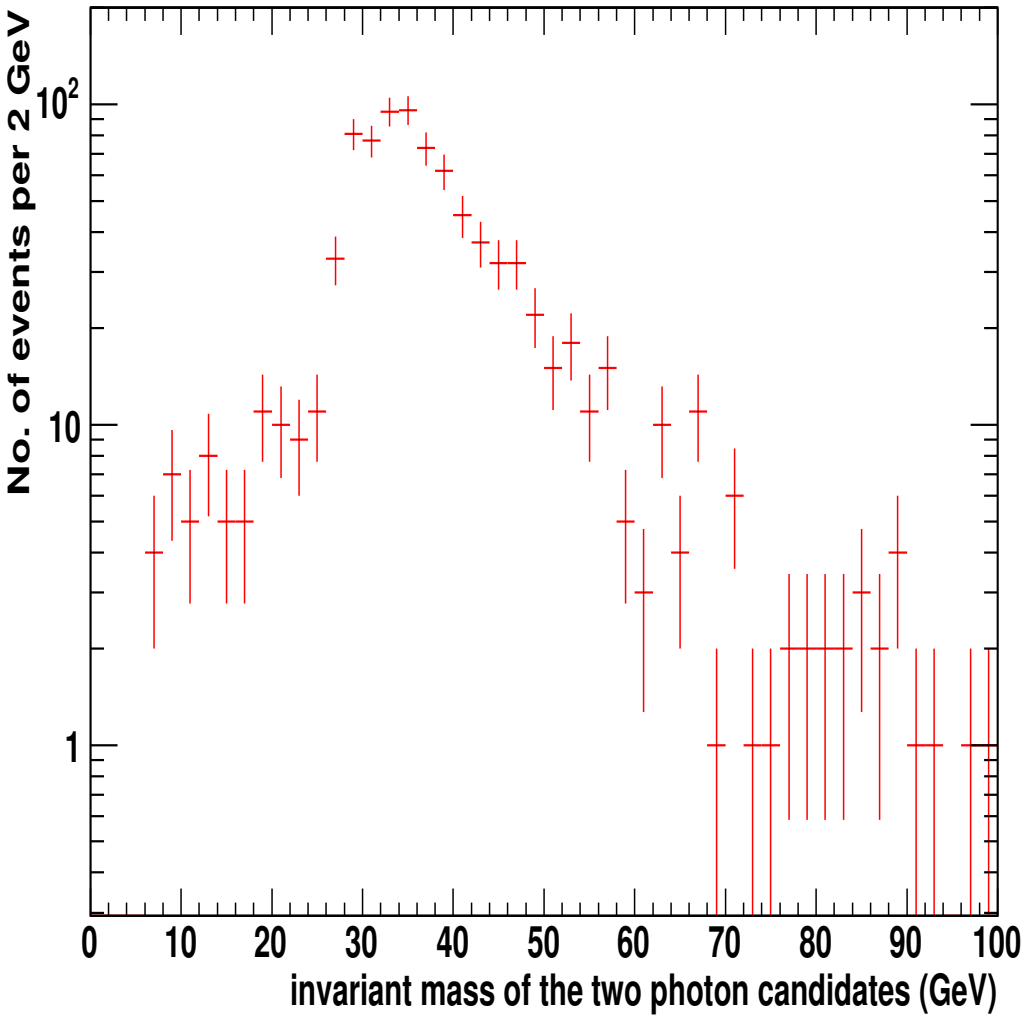

Figure 6.24: mass distribution (GeV) of the diphoton candidates

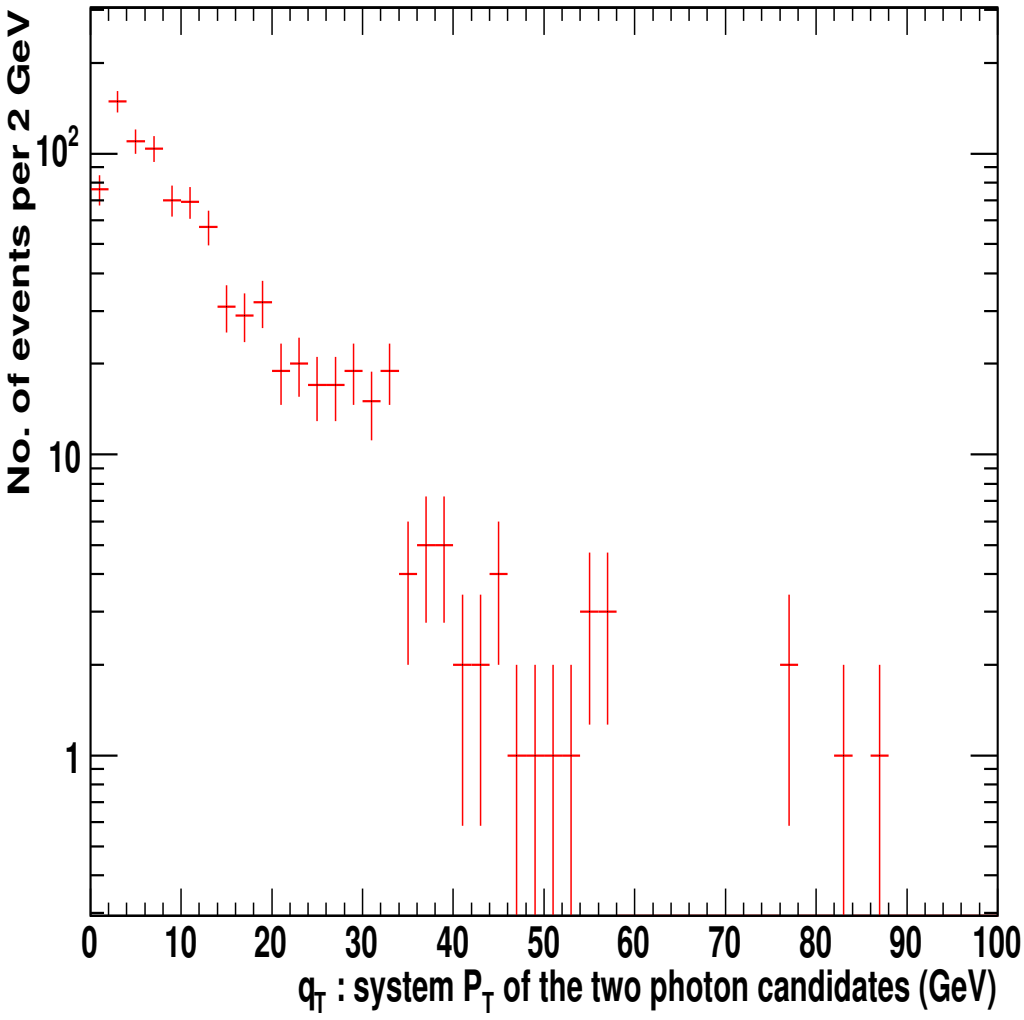

Figure 6.25: q_T (two-body system pT) distribution (GeV) of the diphoton candidates

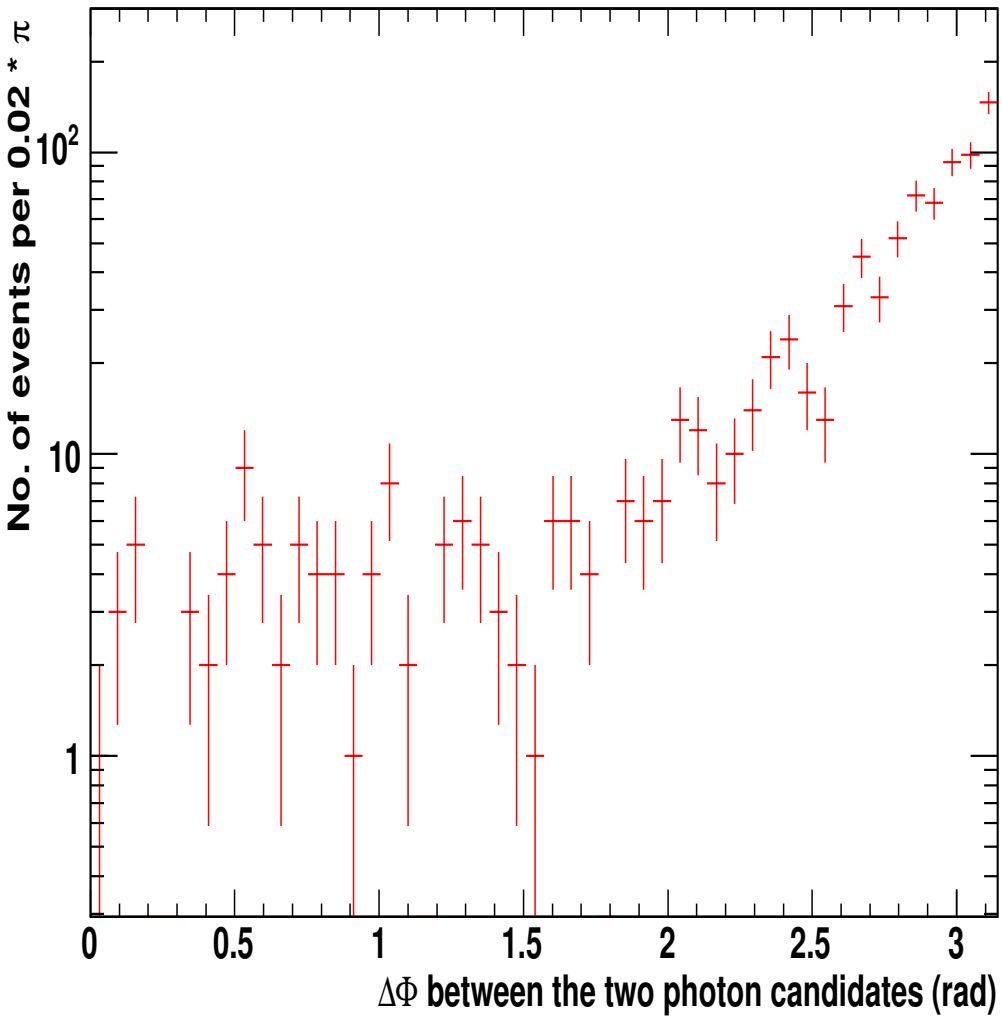

Figure 6.26: ϕ separation of the two photon candidates.

6.5 Background Subtraction

A major background left after the selections cuts is from neutral mesons such as π^0, η that decay to multiple photons. The procedure for subtracting these background is described below.

Suppose there is an ID variable X. The distributions from signal and background are different, as illustrated in Fig. 6.27. The fraction of signal and background passing a cut, for example, $X < X_0$, is ε_s, ε_b respectively. Suppose, in the data sample, there are N_p candidates that pass the cut, and N_f candidates that fail. Unbiased estimators of numbers of signal events N_s and of background events N_b can be obtained by solving the linear equation array 6.2.

$$\begin{cases} (1-\varepsilon_s) \times N_s + (1-\varepsilon_b) \times N_b = N_f \\ \varepsilon_s \times N_s + \varepsilon_b \times N_b = N_p \end{cases} \tag{6.2}$$

Following Eq. 6.2,

$$N_s = N_{total} \times \frac{\varepsilon - \varepsilon_b}{\varepsilon_s - \varepsilon_b} \tag{6.3}$$

where $\varepsilon \equiv N_p/N_{total}, N_{total} \equiv N_p + N_f$. Eq. 6.3 suggests that the signal to background ratio in the sample is just $(\varepsilon - \varepsilon_b)/(\varepsilon_s - \varepsilon)$. The efficiencies $\varepsilon_s, \varepsilon_b$ and ε are functions of E_T. To overlay the three curves in the same plot is then a very intuitive way to present the signal/background composition in the data sample. This method was used in the inclusive photon analysis at CDF Run 1A [50], where the cut $X > X_0$ is CES $\chi^2 < 4$ for $E_T < 35$ GeV, or CPRQ > 500 fC for $E_T > 35$ GeV. See Fig. 6.28.

For the two-photon case, the method must be generalized : there are two cuts, one for each EM object, which classify the candidates in 4 categories :

- N_{pp} of the candidates having both legs pass the cuts.
- N_{pf} of the candidates having the first leg pass, and the second fail (the photon candidates in the event are ordered with descending E_T).
- N_{fp} vice versa.
- N_{ff} having both legs fail the cuts.

Suppose the number of events with both legs being background, one background and one photon, or both photons are $N_{bb}, N_{bs}, N_{sb}, N_{ss}$ respectively, which are related to $N_{pp}, N_{fp}, N_{pf}, N_{ff}$ by an efficiency matrix.

$$\begin{bmatrix} N_{ff} \\ N_{fp} \\ N_{pf} \\ N_{pp} \end{bmatrix} = E \times \begin{bmatrix} N_{bb} \\ N_{bs} \\ N_{sb} \\ N_{ss} \end{bmatrix} \tag{6.4}$$

The 4x4 matrix E is defined as:

$$\begin{bmatrix} (1-\varepsilon_{b1})(1-\varepsilon_{b2}) & (1-\varepsilon_{b1})(1-\varepsilon_{s2}) & (1-\varepsilon_{s1})(1-\varepsilon_{b2}) & (1-\varepsilon_{s1})(1-\varepsilon_{s2}) \\ (1-\varepsilon_{b1})\varepsilon_{b2} & (1-\varepsilon_{b1})\varepsilon_{s2} & (1-\varepsilon_{s1})\varepsilon_{b2} & (1-\varepsilon_{s1})\varepsilon_{s2} \\ \varepsilon_{b1}(1-\varepsilon_{b2}) & \epsilon_{b1}(1-\varepsilon_{s2}) & \varepsilon_{s1}(1-\varepsilon_{b2}) & \varepsilon_{s1}(1-\varepsilon_{s2}) \\ \varepsilon_{b1}\varepsilon_{b2} & \varepsilon_{b1}\varepsilon_{s2} & \varepsilon_{s1}\varepsilon_{b2} & \varepsilon_{s1}\varepsilon_{s2} \end{bmatrix}. \tag{6.5}$$

The Eq. 6.4 can be solved to obtain the estimations of N_{ss}, as well as the estimations of N_{bb}, N_{bs} and N_{sb}. The statistical uncertainty can be evaluated by taking $N_{ff}, N_{fp}, N_{pf}, N_{pp}$ as independently distributed according to Poisson statistics. The efficiency numbers in Eq. 6.5 are a function of E_T.

In the analysis implementation, the linear equation is solved on an event-by-event basis : For each event, the fail-pass 4-vector $(N_{ff}, N_{fp}, N_{pf}, N_{pp})$ is one of the 4 possibilities (1,0,0,0), (0,1,0,0), (0,0,1,0), (0,0,0,1). Suppose the solution of Eq. 6.4 is $N_{ss} = \omega_i$ for event i in the sample; ω_i is taken as the "weight" of the event i. The weighted kinematics distribution represents the distribution of $\gamma\gamma$ events. Explicitly, if there are k candidates in one bin of a histogram, with "weights" $\omega_{i_1}, \omega_{i_2}, ..., \omega_{i_k}$. The $\gamma\gamma$ contribution in the bin is

$$W = \sum_{j=1}^{k} \omega_{i_j}. \tag{6.6}$$

The statistical uncertainty is defined by

$$\sigma = \sqrt{\sum_{j=1}^{k} \omega_{i_j}^2}. \tag{6.7}$$

With the method described, 427±59(stat) $\gamma\gamma$ events are estimated in the sample of 889 candidates : the cuts are the standard cuts used in the inclusive photon analysis, namely $\chi^2 < 4$ for $E_T < 35$ GeV, CPRQ > 500 fC for $E_T > 35$ GeV.

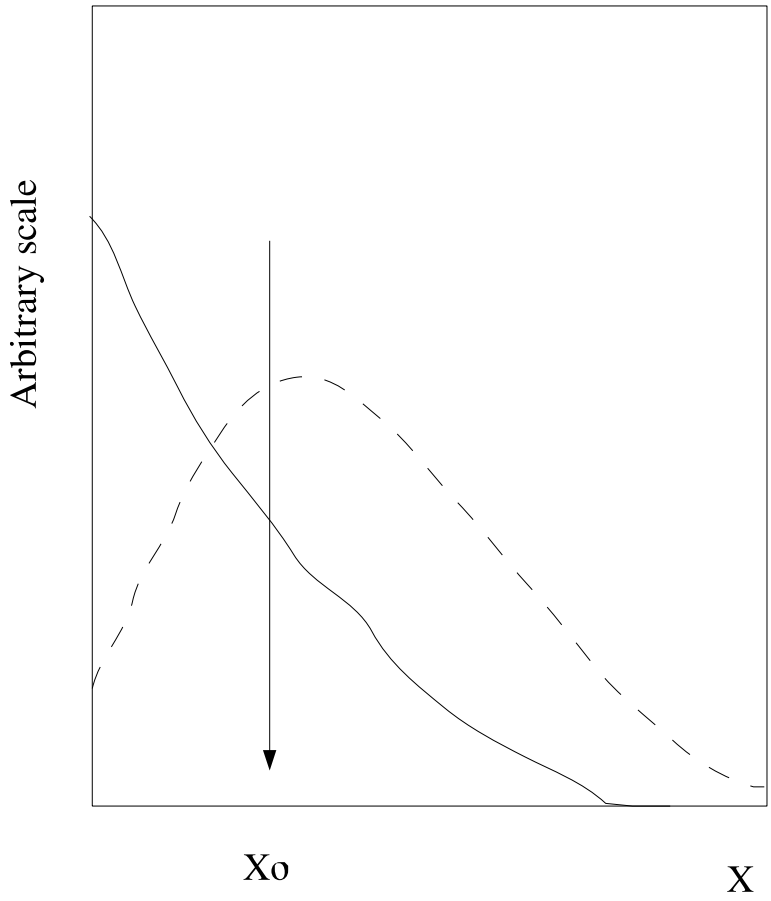

Figure 6.27: The shapes of the distribution of an ID variable X are different in signal and background events. The efficiencies of the cut $X < X_0$ are different for signal (solid line) and background (dashed line) .

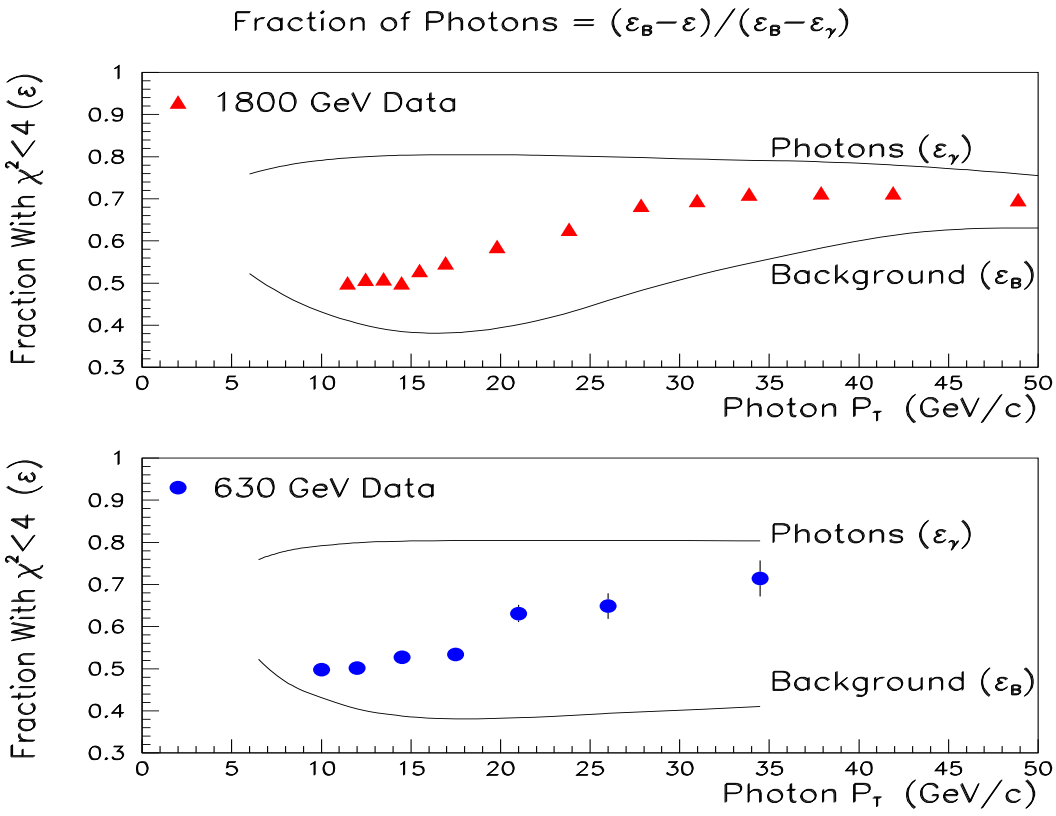

Figure 6.28: Application of the background subtraction method in Run 1, using CES χ^2 variable.

6.6 Efficiency calibration

The efficiency numbers in the 4x4 matrix presented in Eq. 6.5 are very important for this analysis. They are determined in Run 1 using test beam and calibration samples from collision data [50]. They are checked with calibration samples from Run 2 collision data.

6.6.1 CES χ^2 Efficiency calibration

The CES $\chi^2 < 4$ efficiency decreased by ∼5% in the Run 2 data, as verified with low E_T photons from η decay and high E_T electrons from W and Z calibration samples.

$\eta \rightarrow \gamma\gamma$

The $\eta \rightarrow \gamma\gamma$ peak is not difficult to construct if the two photons are contained in different towers. If the two towers are in the same wedge, and neighboring to each other, they are combined as one EM cluster. However, if there are clusters found in the CES in each tower, the positions of the two photons can be determined precisely, combined with the measurement of photon energies by the towers, the invariant mass of the two photons can be calculated. Explicitly, from the fact that photons are massless, the invariant mass of two photons is

$$m_{\gamma\gamma} = \sqrt{2 \times E_1 \times E_2 \times (1 - \cos\theta^*)}, \tag{6.8}$$

where θ^* is the angle between the two photons in the lab frame, measured by the CES, and E_1, E_2 are the energies of the two photons, measured by the CEM towers. The same selection cuts to reduce the background described in Ref. [51] are utilized. The two-photon invariant mass is shown in Fig. 6.29.

From the photons (with E_T ranges from 7 to 12 GeV) under the η peak, after the side-band subtraction, the CES $\chi^2 < 4$ efficiency is found to be 5% lower than in Run 1.

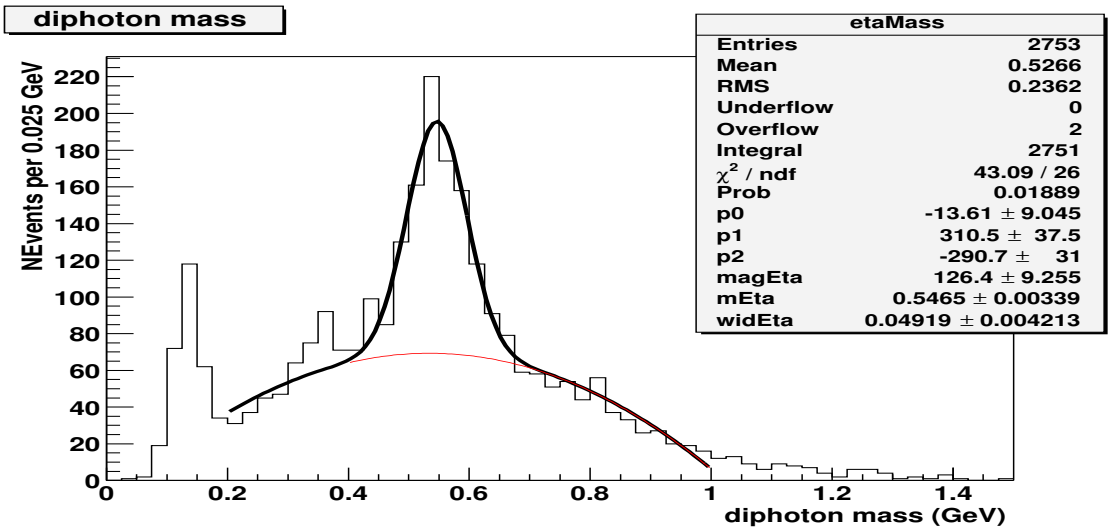

Figure 6.29: Two-photon invariant mass spectrum.

Electrons From W/Z's

For the high E_T part, electrons from the W and Z samples are used. Shown in Fig. 6.30 is the CES wire view $\chi^2 < 4$ fraction as a function of E/p of the electrons from W decay. The shower shape in the wire view can be distorted by the effects of bremsstrahlung, which explains the decrease in the efficiency as E/p deviates from 1. The efficiency is constant when E/p $\approx$ 1, but is lower than that in Run 1 by 5%.

Isolation Tests

To further verify the degradation, the isolation distribution of inclusive photons is measured using the CES efficiencies shifted down by 0.05 and compared with that of electrons under the z peak. It is found that without the -0.05 shift, the measured number of events at large isolation goes significantly negative after the background subtraction, which indicates over-subtracting, see Fig. 6.31. Another check is to use CPR and CES independently to obtain photon fractions from the sample and compare them. Shown in Fig. 6.32 are the results of the tests described above with an inclusive photon sample collected by the 25 GeV trigger. The same set of tests are made with 10 GeV trigger dataset too.

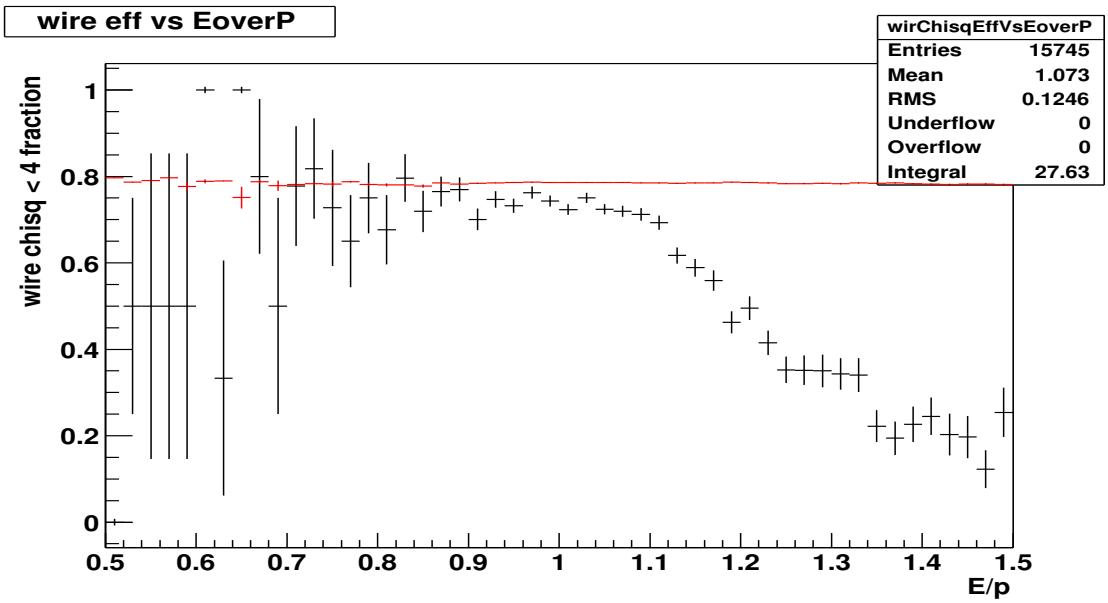

Figure 6.30: CES wire view χ^2 <4 fraction as a function of E/p of the electrons from W decay. The line in red is the predicted fraction for photons in Run 1.

6.6.2 CPR efficiencies

The CPR is used to subtract the background for photons with E_T above 35 GeV, which makes use of the fact that the background of multiple collinear photons from neutral meson decay have a larger chance to generate a hit in the CPR than a photon because the probability of a conversion to take place in the solenoid or the tracker is higher. The material amount for the solenoid and the tracker is studied in Ref. [43]. The probability for the secondary electrons from photon conversions to generate a large charge deposition ($CPRQ > 500fC$) is studied in Ref. [44]. The effect of tracks from underlying event is factorized using the number of vertices in the event [45]. These studies result in slightly different $CPRQ > 500fC$ efficiencies for Run 2. The difference in the $\gamma\gamma$ fraction resulted from these new efficiencies are doubled and included the systematics.

The CES and CPR methods are applied independently to the inclusive photon sample collected by the 25 GeV photon trigger. The photon fraction obtained from background subtraction using CPR Run 1 efficiencies are closer to that from the CES

method. The CPR Run 1 constants are used for the evaluation central values of number of photon-photon events.

6.6.3 Systematic uncertainty from background subtraction.

For the systematic uncertainty from the background subtraction, apart from the uncertainty on the efficiencies in Run 1 analyses, the following contributions are included:

- For the CES: the Run 1 efficiencies are shifted down by 0.03 and 0.05, and the difference in the $\gamma\gamma$ fractions resulted is doubled and included in the systematic uncertainties.

- For the CPR: the difference in the $\gamma\gamma$ fractions from the subtractions using Run 1 CPR efficiencies and those obtained using the Run 2 CPR constants is doubled and included in the systematics.

Shown in Fig. 6.33 is the relative systematic uncertainty from background subtraction as a function of the $\gamma\gamma$ mass.

The data analysis has been described. The results will be shown in the next chapter along with theoretic predictions.

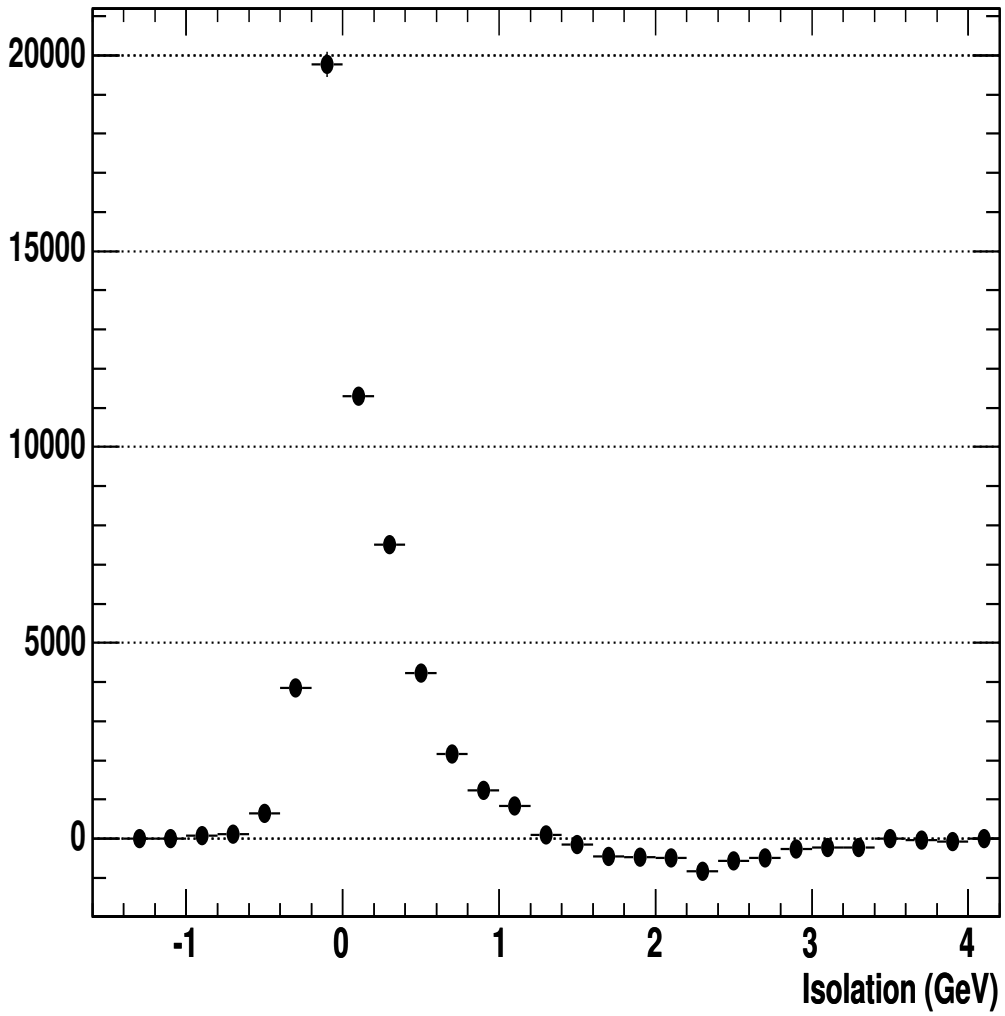

Figure 6.31: The measured photon isolation distribution from the inclusive photon sample, using the Run 1 CES $\chi^2 < 4$ efficiency. At large isolation, the estimated number of photon events is significantly negative, which indicates over-subtracting.

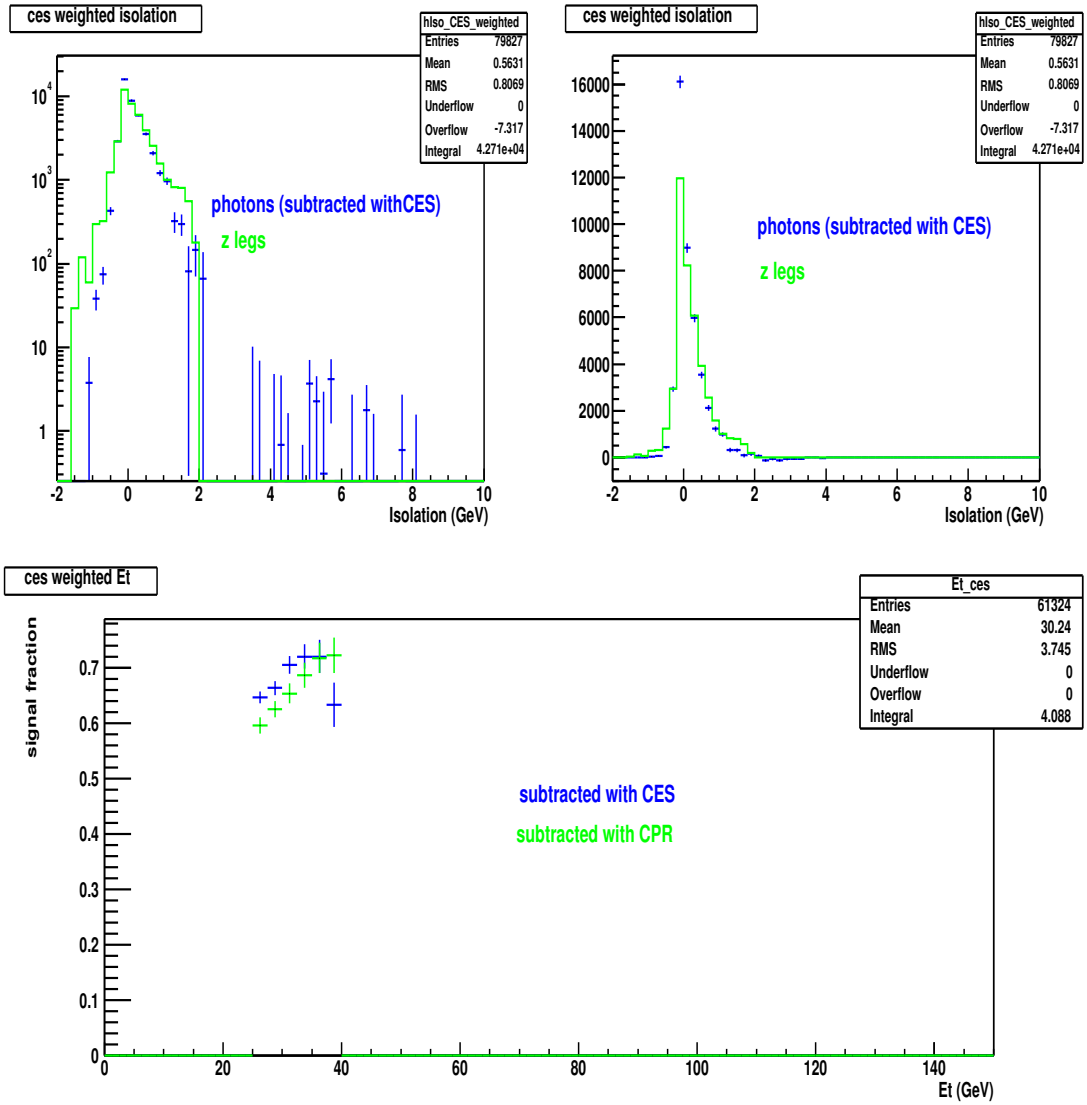

Figure 6.32: More verification of the CES $\chi^2 < 4$ efficiency degradation. Upper plots are the photon isolation distribution (blue) measured with adjusted efficiencies for background subtraction, overlaid with the isolation distribution of electrons under z peak (green) , the comparison is presented in log scale(left) and linear scale(right). The lower plot is the comparison of photon fractions obtained from CES (blue) and CPR (green) independently as a function of photon E_T.

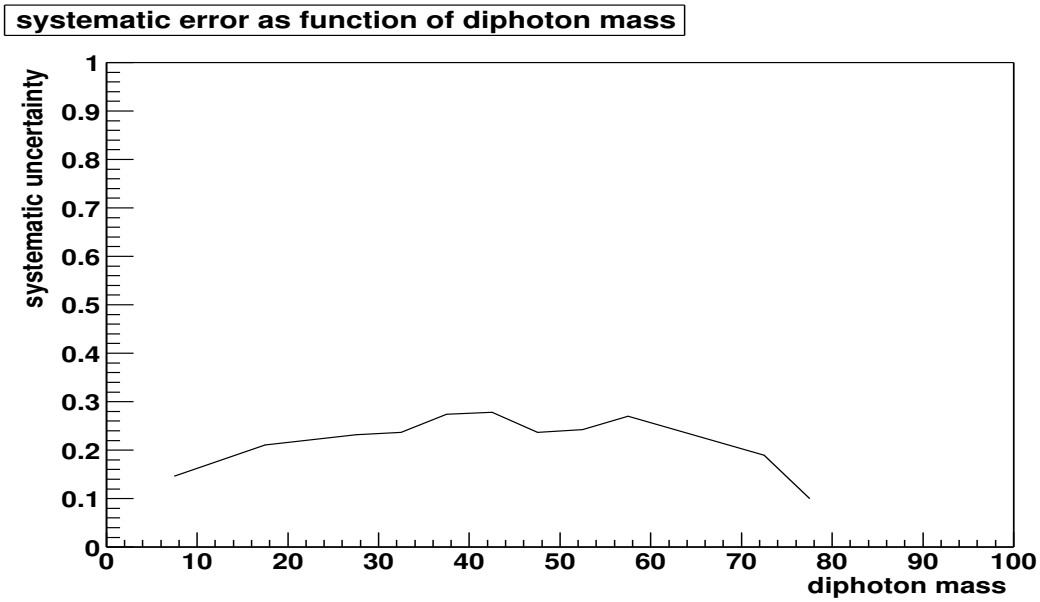

Figure 6.33: Relative systematic uncertainty from background subtraction as a function of the two-photon invariant mass.

Chapter 7

Diphoton Production Cross Sections

The data analysis has been described in the previous chapter. The results will be presented along with theoretical predictions in this chapter. The calculations DIPHOX and ResBos have been introduced and compared in Chapter 3. Recently, higher order corrections for the $gg \rightarrow \gamma\gamma$ contribution have become available [46]. These corrections are included for the data/theory comparisons.

7.1 Data/Theory comparisons

The $\gamma\gamma$ mass distribution from data is shown in Fig. 7.1, along with predictions from DIPHOX, ResBos and PYTHIA. The q_T distribution is shown in Fig. 7.2 and the $\Delta\phi$ distribution between the two photons is shown in Fig. 7.3. The vertical error bars on the data indicate the combined statistical and systematic uncertainties with the inner tick marks indicating the statistical uncertainty alone. The PYTHIA predictions have been scaled (by a factor of 2) to the total measured cross section. The cross sections as a function of these three different variables are also tabulated in Tables 7.1, 7.2 and 7.3.

The data are in good agreement with the predictions for the mass distribution. In the lowest mass bin, the data are closer to the DIPHOX prediction than to those

$M_{\gamma\gamma}$ (GeV)	CDF Data (pb/GeV)	DIPHOX (pb/GeV)	ResBos (pb/GeV)	PYTHIA (pb/GeV)
10-25	0.03 ± 0.03 ± 0.01	0.04	0.01	0.01
25-30	0.44 ± 0.13 ± 0.12	0.41	0.31	0.18
30-35	0.61 ± 0.17 ± 0.16	0.70	0.65	0.38
35-45	0.46 ± 0.10 ± 0.14	0.46	0.43	0.24
45-60	0.16 ± 0.05 ± 0.04	0.19	0.16	0.09
60-100	0.01 ± 0.02 ± 0.01	0.04	0.04	0.02

Table 7.1: A comparison of the cross section as a function of the $\gamma\gamma$ mass for the data and predictions from DIPHOX, ResBos and PYTHIA.

q_T (GeV)	CDF Data (pb/GeV)	DIPHOX (pb/GeV)	ResBos (pb/GeV)	PYTHIA (pb/GeV)
0-1	0.70 ± 0.30 ± 0.14	-2.45	0.34	0.53
1-2	1.18 ± 0.43 ± 0.28	5.59	0.95	1.15
2-4	0.92 ± 0.35 ± 0.28	2.06	1.03	0.94
4-8	0.96 ± 0.23 ± 0.32	1.17	0.94	0.46
8-12	0.29 ± 0.21 ± 0.13	0.44	0.59	0.21
12-16	0.42 ± 0.14 ± 0.12	0.24	0.36	0.12
16-24	0.19 ± 0.09 ± 0.05	0.13	0.19	0.07
24-32	0.12 ± 0.06 ± 0.03	0.09	0.07	0.03
32-40	0.10 ± 0.05 ± 0.05	0.06	0.03	0.01

Table 7.2: A comparison of the cross section as a function of the $\gamma\gamma$ q_T for the data and predictions from DIPHOX, ResBos and PYTHIA.

$\Delta\phi$ (π rad)	CDF Data (pb/rad)	DIPHOX (pb/rad)	ResBos (pb/rad)	PYTHIA (pb/rad)
0.0-0.2	1.06 ± 0.52 ± 0.34	0.69	0.01	0.02
0.2-0.4	0.89 ± 0.52 ± 0.32	0.56	0.23	0.09
0.4-0.6	0.51 ± 0.63 ± 0.19	0.71	0.73	0.44
0.6-0.8	3.34 ± 1.10 ± 1.04	1.83	3.08	1.09
0.8-1.0	15.56 ± 2.59 ± 4.70	23.37	17.52	10.68

Table 7.3: A comparison of the cross section as a function of the $\gamma\gamma$ $\Delta\phi$ for the data and predictions from DIPHOX, ResBos and PYTHIA.

from ResBos or PYTHIA, but the statistical errors are large in this region. At low to moderate q_T and $\Delta\phi$ greater than $\pi/2$, where the effect of soft gluon emissions are important, the data agree better with ResBos than DIPHOX. By contrast, in the regions where the $2\rightarrow3$ fragmentation contribution becomes important, large q_T and $\Delta\phi$ less than $\pi/2$, the data agree better with DIPHOX. Although the data is suggestive of these differences higher statistics will be needed for a definitive comparison.

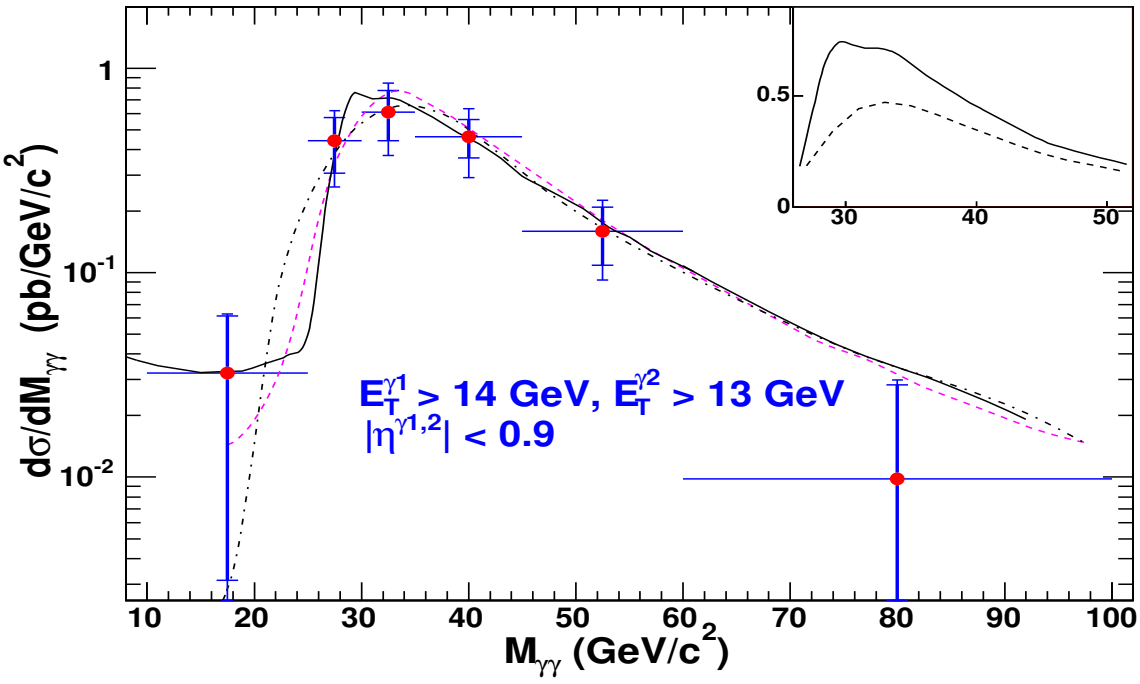

Figure 7.1: The cross sections as function of $\gamma\gamma$ mass from the CDF Run II data, along with predictions from DIPHOX(solid), ResBos(dashed), and PYTHIA(dot-dashed). The PYTHIA predictions have been scaled by a factor of 2. The inset shows, on a linear scale, the total NLO $\gamma\gamma$ cross section from DIPHOX with (solid)/without (dashed) the gg contribution.

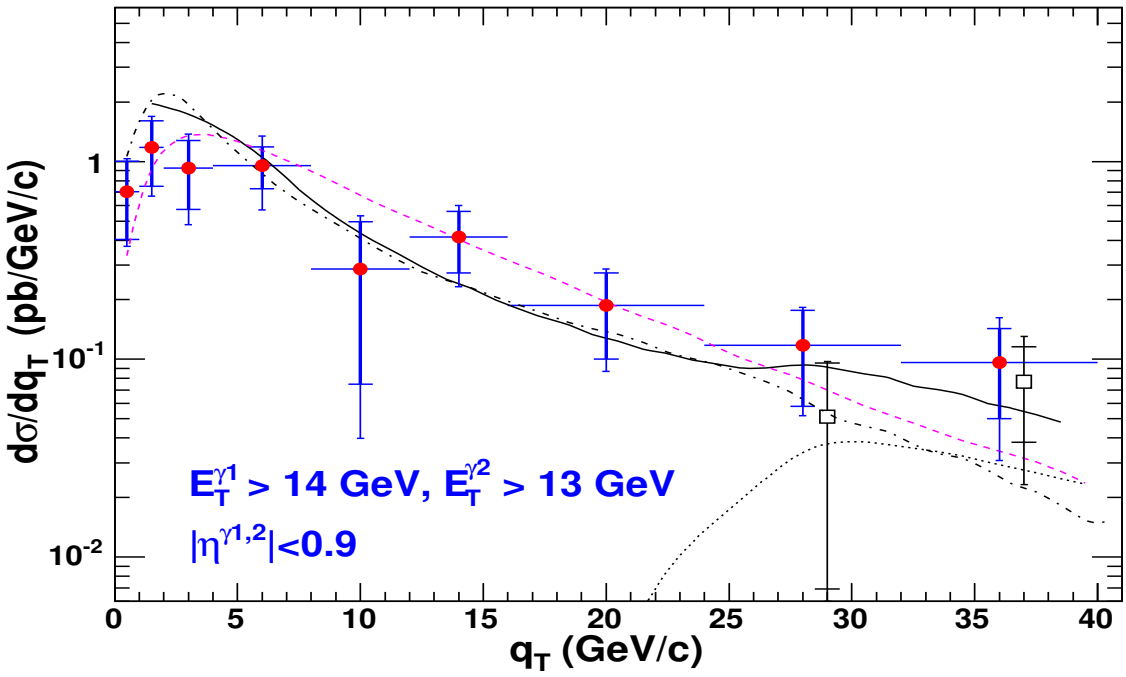

Figure 7.2: The $\gamma\gamma$ q_T from the CDF Run II data, along with predictions from DIPHOX(solid), ResBos(dashed), and PYTHIA(dot-dashed). The PYTHIA predictions have been scaled by a factor of 2. Also shown, at larger q_T, are the DIPHOX prediction (dot) and the CDF Run II data (open squares, shifted to the right by 1 GeV for visibility) for the configuration where the two photons are required to have $\Delta\phi < \pi/2$

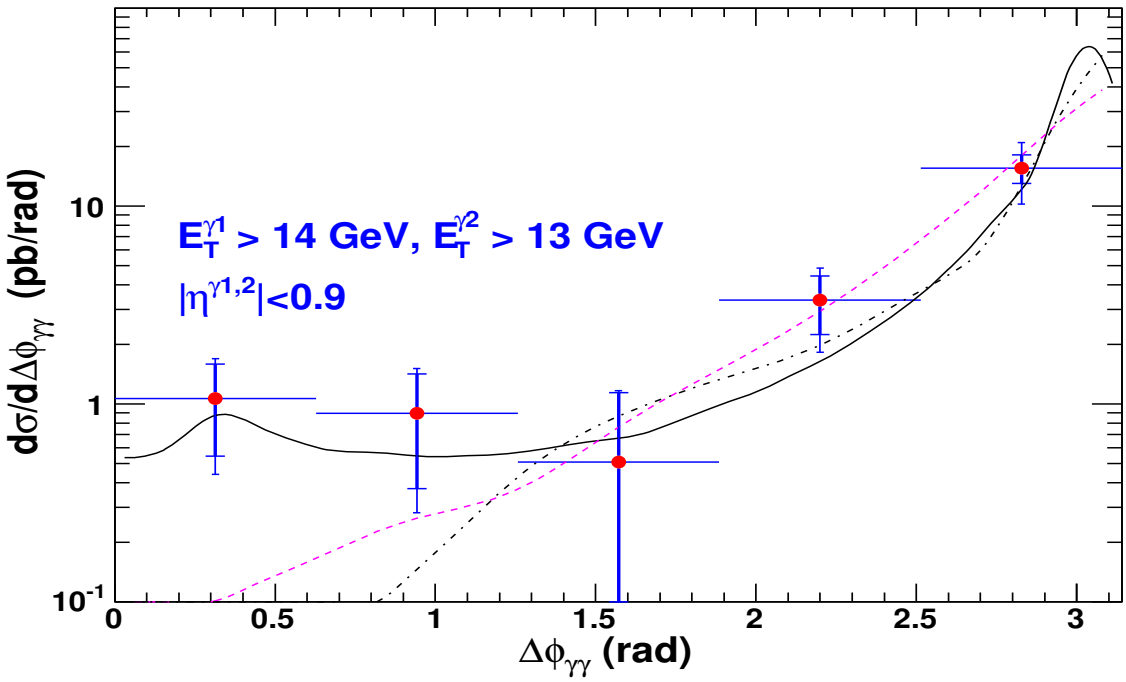

Figure 7.3: The $\Delta\phi$ angle between the two photons from the CDF Run II data, along with predictions from DIPHOX(solid), ResBos(dashed), and PYTHIA(dot-dashed). The PYTHIA predictions have been scaled by a factor of 2.

7.2 Conclusion

Diphoton production serves both as a venue for precision tests of QCD as well as a background for potential new physics processes. We have presented results for $\gamma\gamma$ production in $p\overline{p}$ collisions at a center-of-mass energy of 1.96 TeV using a data sample twice that previously available. Good agreement has been observed with resummed and NLO predictions in different regions of phase space. For agreement in all areas, however, a resummed fully NLO calculation will be necessary.

List of Tables

1.1 L'efficacité des différents critères de sélection. 16
1.2 Section efficace en fonction de la masse invariante $\gamma\gamma$ pour les données et les prédictions de DIPHOX, ResBos et PYTHIA. 18
1.3 Section efficace en fonction de q_T pour les données et les prédictions de DIPHOX, ResBos et PYTHIA. 18
1.4 Section efficace en fonction de $\Delta\phi$ pour les données et les prédictions de DIPHOX, ResBos et PYTHIA. 18

2.1 Leptons in the Standard Model [5] 26
2.2 Quarks in the Standard Model [5] 27

5.1 Central electromagnetic calorimeter (CEM) technical summary. . . . 60
5.2 Parameter of the Central hadron Calorimeter [17]. 64
5.3 Parameters of the End Wall hadron Calorimeter [17]. 65
5.4 Over view of the plug calorimeter [15]. The EM (hadron) resolution is the designed specification for a single electron (pion). 66
5.5 Design parameters of the CDF II Muon detectors. Pion interaction lengths and multiple scattering are computed at a reference angle of $\theta = 90°$ in CMU and CMP/CSP, at an angle of $\theta = 55°$ in CMX/CSX, and show the range of values for the IMU. [15] 67

6.1 List of the quality cuts which are used at L3 for photon triggers. χ^2_{wire} and χ^2_{strip} are the χ^2 of fitting the showermax profiles of wire and strip view respectively with standard profiles obtained from test beam data [34], the χ^2 cut is employed for central EM objects only. 77
6.2 Event selection cuts. 84
6.3 The efficiencies for the cuts used in the $\gamma\gamma$ analysis. 109

7.1 A comparison of the cross section as a function of the $\gamma\gamma$ mass for the data and predictions from DIPHOX, ResBos and PYTHIA. 126
7.2 A comparison of the cross section as a function of the $\gamma\gamma$ q_T for the data and predictions from DIPHOX, ResBos and PYTHIA. 126
7.3 A comparison of the cross section as a function of the $\gamma\gamma$ $\Delta\phi$ for the data and predictions from DIPHOX, ResBos and PYTHIA. 126

List of Figures

1.1 Exemple de diagrammes où les deux photons finaux sont produits dans des processus durs: ces contribution sont appellées “two-direct”. . . . 12
1.2 Exemple de diagrammes où un photon direct est produit ainsi qu’un photon issu de la fragmentation d’un parton. Ces contribution sont appellées “one-fragmentation”. 13
1.3 Exemple de diagrammes où les deux photons finaux sont issus de la fragmentation de partons. Ces contribution sont appellées “two-fragmentation”. 14
1.4 Le diagramme de boîte $gg \rightarrow \gamma\gamma$: deux gluons initiaux produisant deux photons finaux via une boucle de quarks. 15
1.5 La distribution de masse invariante $\gamma\gamma$, $M_{\gamma\gamma}$, pour les données avec les prédictions de DIPHOX (trait plein), ResBos (traitillé), et PYTHIA (point et trait). Les prédictions de PYTHIA ont été multipliées par un facteur 2. L’encart montre (échelle linéaire) la section efficace NLO prédite par DIPHOX avec (trait plein) et sans (traitillé) la contribution gg. 17
1.6 La distribution de l’impulsion transverse du système des deux photons, q_T, pour les données (ronds pleins) avec des prédiction de DIPHOX (trait plein), ResBos (traitillé), et PYTHIA (point et trait). Les prédictions de PYTHIA ont été multipliées par un facteur 2. Les résultats pour les données (ronds vides) et les prédictions de DIPHOX (pointillés) lorsque $\Delta\phi < \pi/2$ sont visibles pour $q_T > 20$ GeV. 19

1.7 La distribution de l'angle entre les deux photons $\Delta\phi$ pour les données (rond pleins) avec des prédictions de DIPHOX (trait plein), ResBos (traitillé), et PYTHIA (point et trait). Les prédictions de PYTHIA ont été multipliées par un facteur 2. 20

3.1 Examples of diagrams with the two photons at final state produced at hard-scattering : these contributions are called "two-direct". 35
3.2 Examples of diagrams with one of the two photons at final state produced at fragmentation : these contributions are called "one-fragmentation". 36
3.3 Examples of diagrams with both photons produced at fragmentation : these contributions are called "two-fragmentation". 37
3.4 The "box" diagram : the gluon-gluon at initial state coupled to $\gamma\gamma$ via a quark loop. This process is at order of $\alpha_{em}^2\alpha_s^2$, but the rate is still appreciable at some kinematic regions because of the high gluon density at low x. 38
3.5 Invariant mass distributions by DIPHOX NLO predictions. The box contribution is negligible at high mass region. But the calculated cross section is negative at the 26 GeV bin in the prediction without box contribution, because the cancellation of divergences from real and virtual soft/collinear gluon emissions becomes imperfect with the symmetric cuts. 39
3.6 Invariant mass distributions by DIPHOX NLO predictions. No singular point on either of the two curves, with the asymmetric E_T cut. The prediction is more reliable with asymmetric cuts, and we adopt the asymmetric E_T cut for data/theory comparisons. 40
3.7 The final state of "one-fragmentation" contribution : a photon balanced against a jet, within which embeded another photon. For this configuration, the q_T of the two photons is equal to the isolation of the photon insided the jet. The isolation cut makes q_T distribution a step function for this contribution. 41

3.8 Kinematics of the 2→3 processes in DIPHOX : quark-gluon fusion. The quark in the final state radiates a photon, and another photon is produced at the hadronization of the quark. 42
3.9 Invariant mass distributions from DIPHOX and ResBos. The transverse energy (E_T)of the leading photon is required to be above 14 GeV; the E_T of the softer photon is required to be above 13 GeV. The threshold effect at $m_{\gamma\gamma} = 28$ GeV from the back-to-back contributions is evident. At lower mass, DIPHOX predicts a higher production rate than ResBos due to the $2 \rightarrow 3$ contributions illustrated in Fig. 3.8, which is currently absent in ResBos. 43
3.10 Diphoton q_T (the transverse momentum of the two-photon system) distributions from DIPHOX and ResBos. DIPHOX curve is unstable at low q_T due to the divergences of the fixed-order calculation. ResBos resums the effect of multiple soft gluon emissions at initial state and predicts a smooth q_T distribution. DIPHOX curve is enhanced at large q_T due to the $2 \rightarrow 3$ processes illustrated in Fig. 3.8, which is currently absent in ResBos. 44
3.11 $\Delta\phi$ between the two photons ($\phi_{\gamma\gamma}$) from ResBos and DIPHOX. The fixed-order calculation, DIPHOX, is divergent at $\phi_{\gamma\gamma} = 0$ and $\phi_{\gamma\gamma} = \pi$. The divergence at $\phi_{\gamma\gamma} = \pi$ is supressed by an anti-collinear cut implemented in DIPHOX, which requires $\sqrt{(y_{\gamma 1} - y_{\gamma 2})^2 + (\phi_{\gamma 1} - \phi_{\gamma 2})^2} > 0.3$. This cut produces the bump at $\phi_{\gamma\gamma} = 0.3$. On average, the DIPHOX predicts a higher rate for $\phi_{\gamma\gamma} < \pi/2$ region due to the $2 \rightarrow 3$ processes illustrated in Fig. 3.8, which is currently absent in ResBos. 45

4.1 The accelerator complex at FNAL. 50
4.2 Instaneous luminosity of Tevatron Run II as function of store number. The corresponding period is indicated on the top of the figure. . . . 51
4.3 CDF acquired luminosities as function of the day in 2001-2004 calendar years. 51

5.1 An isometric view of the CDF II detector 53

5.2 An elevation view of the CDF II detector 54
5.3 The cross section schematic view of the CDF II inner tracking system. The tracking system consists of a silicon tracker at small radius surrounded by a large open cell drift chamber. The silicon tracker is made of five layers of Silicon Vertex detector (SVX II) at very small radius, followed by three layers of Intermediate Silicon Layers(ISL). 57
5.4 The cut-away view of a CEM wedge. 61
5.5 Diagram of the CES strip/wire orientations: Cathode strips running in the azimuthal direction provide z information, while anode wires running in the z direction provide r-ϕ information. 62
5.6 Quadrant of the calorimeter where A,B,C show Central, End-Wall and Plug respectively. Towers are numbered from 0 (at 90° in polar direction) to 11 (last tower of End-Wall modules). Hadronic towers 6,7 and 8 are shared between Central and End-Wall calorimeter. [17] 63
5.7 Functional block diagram of the 3-level trigger system. For each level-1 accept the data is stored in a L2/DAQ buffer while the Level-2 trigger works. A level-2 accept initiates the read-out of the event data into the Level-3 processor farm where an accept causes the data to be written to disk/tape. 70
5.8 Functional block diagram of the L1 and L2 trigger system. 71

6.1 An illustration of the detector components outside the tracking volume at CDF II that are important for photon detection(not-to-scale). The solenoid coil is used as the preradiator by the preshower detector (CPR) mounted in front of the EM calorimenter towers immediately outside the magnet. A 2-dimensional multi-wire proportional chamber (CES) is embedded at the shower maximum at six radiation lengths. The two dotted lines illustrate two photons from neutral meson decay, which generate two clusters at the CES. 79

6.2 The five isolation sums [33]; ϕ is increasing upward, and η is increasing to the left. 'S' denotes the seed tower. Labelled with 'X' are the towers included in the isolation sum. The first sum is the one used in the CDF Run I triggers. 80
6.3 The DIPHOTON_12 trigger cross section [35]. 81
6.4 DI_PHOTON_12 efficiency (per leg) vs. EM E_T (GeV), parameterized as $p0 * Erfc(p1 * (p2 - Et))$ (fitted parameters are : p0 = 4.98695e-01 ± 6.56155e-03, p1= 6.49414e-01 ± 1.14311e-01, p2 =1.23154e+01 ± 2.06161e-01) to unweight data points. Numerator : diphoton_12 trigger bit. Denominator : photon_25_iso trigger bit and two isolated photon candidates in the CEM. See text for details. The red line is at 13 GeV. 82
6.5 The efficiency of matching generation level photons to offline reconstructed photons vs. η from diphoton PYTHIA MC. Each event contributed two entries since there are two prompt photons in it. 86
6.6 The efficiency of matching generation level photons to offline reconstructed photons vs. ϕ, Each event contributed two entries since there are two prompt photons in it. 87
6.7 The efficiency of matching the generation level photons to offline reconstructed photons vs. diphoton mass. Plotted in red squared dots is the probability for both photons at generation level to have matching photon candidates in the fiducial detector region at offline level, in black circles and blue triangles the efficiency for each of the photons. We fit the three curves with horizontal straight lines, the fit values (A) and χ^2's are:
A(circle) = 0.652, with $\chi^2/ndf = 91/83$;
A(triangle) = 0.653, with $\chi^2/ndf = 88/83$;
A(square) = 0.428, with $\chi^2/ndf = 112/83$.
The correlation of the acceptance between the two photons is negligible. 88

6.8 The efficiency of matching the generation level photons to offline reconstructed photons vs. diphoton q_T. Plotted in red squares is the probability for both photons at generation level to have matching photon candidates at offline level, in black circles and blue triangles the efficiency for each of the photons. 89
6.9 The efficiency of matching the generation level photons to offline reconstructed photons vs. diphoton $\Delta\phi$. Plotted in red squares is the probability for both photons at generation level to have matching photon candidates at offline level, in black circles and blue triangles the efficiency for each of the photons. 90
6.10 Diphoton $\Delta\phi$ from PYTHIA MC with ISR turned off. 91
6.11 isolation in 0.4 cone (GeV) for prompt photons from PYTHIA diphoton MC. 93
6.12 The isolation < 1 GeV efficiency as a function of the diphoton mass (in GeV). Plotted in red squares is the probability for both photons passing the isolation cut, in black circles and blue triangles the probability for each of the photons passing the isolation cut. We fit the 3 curves with flat straight lines and the fit values (ε) and χ^2's are:
ε(circles) = 0.838, with $\chi^2/ndf = 151.1/83$;
ε(triangles) = 0.834, with $\chi^2/ndf = 126.1/82$;
ε(squares) = 0.703, with $\chi^2/ndf = 197.7/83$.
The χ^2/ndf's are too large to justify a constant isolation efficiency for any mass. 94
6.13 The isolation < 1 GeV efficiency as a function of the diphoton q_T (in GeV). Plotted in red squares is the probability for both photons passing the isolation cut, in black circles and blue triangles the probability for each of the photons passing the isolation cut. 95
6.14 The isolation < 1 GeV efficiency as a function of the diphoton $\Delta\phi$ (in rad). Plotted in red squares is the probability for both photons passing the isolation cut, in black circles and blue triangles the probability for each of the photons passing the isolation cut. 96

6.15 The isolation < 1 GeV efficiency as a function of the photon E_T (in GeV), from the diphoton PYTHIA sample (pexo2d). 97
6.16 Track multiplicity of prompt photons in diphoton PYTHIA MC. . . 99
6.17 No-track cut efficiency as a function of the diphoton mass. Plotted in red squares is the probability for both photons passing the no-track requirement, in black circles and blue triangles the probability for each of the photons passing the cut. 100
6.18 No-track cut efficiency as a function of the diphoton q_T. Plotted in red squares is the probability for both photons passing the no-track requirement, in black circles and blue triangles the probability for each of the photons passing the cut. 101
6.19 No-track cut efficiency as a function of the diphoton $\Delta\phi$. Plotted in red squares is the probability for both photons passing the no-track requirement, in black circles and blue triangles the probability for each of the photons passing the cut. 102
6.20 The efficiency of no-extra CES cluster cut as a function of the diphoton mass. Plotted in red squares is the probability for both photons passing the no-extra cluster requirement, in black circles and blue triangles the probability for each of the photons passing the cut. No-track and isolation cuts are imposed as prerequisite. We fit the three curves with flat straight line, the fitted efficiencies ($\varepsilon_{no-extraCES}$) and the χ^2's are:
$\varepsilon_{no-extra\,CES}(squares) = 0.948$, with $\chi^2/ndf = 71.9/72$;
$\varepsilon_{no-extra\,CES}(triangles) = 0.948$, with $\chi^2/ndf = 73.9/73$;
$\varepsilon_{no-extra\,CES}(squares) = 0.897$, with $\chi^2/ndf = 104.2/78$;
(As indicated by the ndf's, the fittings are done with finer binning than what's shown in the plot.) 104
6.21 The efficiency of the no-extra CES cluster cut as a function of the diphoton q_T. Plotted in red squares is the probability for both photons passing the no-extra cluster requirement, in black circles and blue triangles the probability for each of the photons passing the cut. . . 105

6.22 The efficiency of the no-extra CES cluster cut as a function of the diphoton $\Delta\phi$. Plotted in red squares is the probability for both photons passing the no-extra cluster requirement, in black circles and blue triangles the probability for each of the photons passing the cut. No-track and isolation cuts are imposed as prerequisite. 106
6.23 Z-Vertex distribution of diphoton MC events : a number of events were found with no vertex reconstructed, and placed at the first bin (zv = -100.0) 108
6.24 mass distribution (GeV) of the diphoton candidates 110
6.25 q_T (two-body system pT) distribution (GeV) of the diphoton candidates 111
6.26 ϕ separation of the two photon candidates. 112
6.27 The shapes of the distribution of an ID variable X are different in signal and background events. The efficiencies of the cut $X < X_0$ are different for signal (solid line) and background (dashed line) 116
6.28 Application of the background subtraction method in Run 1, using CES χ^2 variable. 117
6.29 Two-photon invariant mass spectrum. 119
6.30 CES wire view χ^2 <4 fraction as a function of E/p of the electrons from W decay. The line in red is the predicted fraction for photons in Run 1. 120
6.31 The measured photon isolation distribution from the inclusive photon sample, using the Run 1 CES $\chi^2 < 4$ efficiency. At large isolation, the estimated number of photon events is significantly negative, which indicates over-subtracting. 122

6.32 More verification of the CES $\chi^2 < 4$ efficiency degradation. Upper plots are the photon isolation distribution (blue) measured with adjusted efficiencies for background subtraction, overlaid with the isolation distribution of electrons under z peak (green) , the comparison is presented in log scale(left) and linear scale(right). The lower plot is the comparison of photon fractions obtained from CES (blue) and CPR (green) independently as a function of photon E_T. 123
6.33 Relative systematic uncertainty from background subtraction as a function of the two-photon invariant mass. 124

7.1 The cross sections as function of $\gamma\gamma$ mass from the CDF Run II data, along with predictions from DIPHOX(solid), ResBos(dashed), and PYTHIA(dot-dashed). The PYTHIA predictions have been scaled by a factor of 2. The inset shows, on a linear scale, the total NLO $\gamma\gamma$ cross section from DIPHOX with (solid)/without (dashed) the gg contribution. 128
7.2 The $\gamma\gamma$ q_T from the CDF Run II data, along with predictions from DIPHOX(solid), ResBos(dashed), and PYTHIA(dot-dashed). The PYTHIA predictions have been scaled by a factor of 2. Also shown, at larger q_T, are the DIPHOX prediction (dot) and the CDF Run II data (open squares, shifted to the right by 1 GeV for visibility) for the configuration where the two photons are required to have $\Delta\phi < \pi/2$ 129
7.3 The $\Delta\phi$ angle between the two photons from the CDF Run II data, along with predictions from DIPHOX(solid), ResBos(dashed), and PYTHIA(dot-dashed). The PYTHIA predictions have been scaled by a factor of 2. 130

Bibliography

[1] Addison-Wesley publishing company *Modern Physics and antiphysics* Aldoph Baker (1970). Chapter 1. Is Physics Relevant?

[2] Presses polythechniques et universitaires romandes *Théorie quantique des champs*, Jean-Pierre Derendinger

[3] McGraw-Hill INTERNALTIONAL EDITIONS Physics Series *Quantum Field Theory*, Claude Itzykson, Jean-Bernard Zuber

[4] M. Kobayashi and T. Maskawa, Prog. Theor. Phys. **49**,652(1973) N. Cabibbo, Phys. Rev. Lett. **10**,531(1963)

[5] Paticle Data Group *The Review of Particle Physics* European Jounrnal of Physics **C15**(2000). http://pdg.lbl.gov

[6] P. W. Higgs (1964), Physics Letters **12**,132-133 (1964) F. Englert, R. Brout, Phys. Rev. Lett. **13**, 321-323 (1964)

[7] H. Lehmann, K. Symanzik and W. Zimmermann, Nuovo Cimento **1** 1425 (1955).

[8] J. Collins and D. Soper, *Nucl. Phys.* **B193**,381 (1981); *Nucl. Phys.* **B213**,545(E) (1983); *Nucl. Phys.* **B 197**,446(1982). J. Collins, D. Soper and G. Sterman, *Nucl. Phys.* **B250**,199 (1985).

[9] Eur. Phys. J. **C 16** ,311-330(2000) *A full next-to-leading order study of direct photon pair production in hadronic collisions.* , T.Binoth, J.Ph.Guillet, E.Pilon, M.Werlen.

[10] J. Ph. Guillet, private communications.

[11] Phys. Rev. **D57**,6934-6947(1998) [hep-ph/9712471] *Photon pair production with soft gluon resummation in hadronic interactions.* C. Balazs, E.L. Berger, S. Mrenna, C.P. Yuan.

[12] Cambridge University Press *QCD and Collider Physics* R. K. Ellis, W. J. Stirling,B. R. Webber (1996)

[13] JHEP **9710** ,005(1997) *Infrared Safe But Infinite: Soft Gluon Divergences Inside the Physical Region.* S.Catan and B. Webber.

[14] Joey Huston, *Talk at the Generator Workshop during the CMS CPT week on Nov 3, 2004.*

[15] FERMILAB-Pub-96/390-E *The CDF II Detector Technical Design Report* the CDF II collaboration.

[16] Nuclear Instruments and Methods in Physics Research **A267** (1988) 272-279 *The CDF Central Electromagnetic Calorimeter* L.BALKA et al.

[17] Nuclear Instruments and Methods in Physics Research **A267** (1998) 301-314. *The CDF Central and Endwall Hadron Calorimeter* S. Bertolucci et al.

[18] Nuclear Instruments and Methods in Physics Research **A480** (2002) 524-546. *The CDF plug upgrade electromagnetic calorimeter : test beam results* M. Albrow et al.

[19] Nuclear Instruments and Methods in Physics Research **A412** (1998) 515-526. *Shower maximum detector for the CDF plug upgrade calorimeter* G. Apollinari, K.Goulianos, P.Melese, M. Lindgren.

[20] Nuclear Instruments and Methods in Physics Research **A268** (1988) 33-40. *CDF CENTRAL MUON DETECTOR* G. Ascoli et al.

[21] CDF Internal note 2858 (1994) *The 1992 CDF Muon System upgrade* FermiLab, Harvard, Illinois, Pisa, Osaka, Tsukuba, Pisa Frascati, etc.

[22] Nuclear Instruments and Methods in Physics Research **A461** (2001) 540-544 *The CDF Cherenkov luminosity monitor* D. Acosta et al.

[23] Nuclear Instruments and Methods in Physics Research **A441** (2000) 366-373 *Luminosity monitor based on Cherenkov counters for $p\overline{p}$ colliders* J.Elias et al.

[24] CDF Internal note 2038 (1994) *conceptual Design of a Deadtimeless Trigger for the CDF Trigger Upgrade* H. Frisch, M. Shochet, G. Sullivan, D. Toback, J. Wahl, P. Wilson, M.Campbell

[25] CDF Internal note 2045 (1994) *Trigger Tower organization and summing in $\eta - \phi$ space for Run II and beyond.* H. Frisch, M. Shochet, G. Sullivan and P.J.Wilson.

[26] CDF Internal note 5293 (2000) *Run II Jet Physics* Gerald C. Blazey et al.

[27] CDF Internal note 5456 (2003) *Electron Identification for Run II : algorithms* Bob Wagner.

[28] CDF Internal note 5682 (2001) *A New PEM Clustering algorithm for Run II* David Goldstein.

[29] CDF Internal note 4718 (2001) *CDF Run-II Trigger Table and Datasets Plan* The Trigger and Datasets Working Group.

[30] CDF Data Quality Monitoring Home Page *http://www-cdf.fnal.gov/internal/dqm/dqm.html* CDF DQM Group. Offline software version 4.11.2 is used in this analysis; the corresponding DQM ntuple version is "Version 4.0".

[31] CDF Internal note 6292 (2003) *Study of Level 2 Electron Clustering.* Carla Grosso-Pilcher, Monica Tecchio

[32] *talk at Trigger and Dataset Working group (25/07/2003)* Yanwen Liu

[33] CDF Internal note 5788 (2001) *Level 2 Isolation Trigger Information* Bob Blair, John Dawson, William Haberichter, Steve Kuhlmann, Monica Tecchio.

[34] CDF Internal note 1329 (1990) *Definition of CES* χ^2 Robert M. Harris

[35] Trigger and Dataset Working Group.
http://www-cdf.fnal.gov/internal/upgrades/daq_trig/twg/index.html

[36] CDF Internal note 5172 (1999) *Diphoton Production in 1.8TeV Proton-Antiproton Collisions.*
Takeshi Takano (thesis, not published)

[37] Computer Physics Commun. **135** (2001) 238. T. Sjostrand, P. Eden, C. Friberg, L. Lonnblad, G. Miu, S. Mrenna and E. Norrbin,

The large manual is T. Sjostrand, L. Lonnblad and S. Mrenna, LU TP 01-21 [hep-ph/0108264]. The Pythia version used in this analysis is 6.216

[38] Rick Field Phys. Rev. **D65**, 092002, (2002)
http://www.phys.ufl.edu/∼rfield/cdf/tunes/rdf_tunes.html, and private communications.

[39] CDF Detector Simulation
http://www-cdf.fnal.gov/cdfsim/cdfsim_main.html

[40] CDF Internal note 6601 (2004) *Measurement of the Wgamma and Zgamma Production Cross Sections* Doug Benjamin, Alfred Goshaw, Michael Kirby, Beate Heinemann, Helen Hayward, Naho Tanimoto.

[41] GEANT is a tool for detector description and simulation of the passages of particles through the matter. *http://wwwasdoc.web.cern.ch/wwwasdoc/geant_html3/geantall.html*

[42] CDF Internal note 6331 (2003) *Event $|Zvtx| < 60$ cm Cut Efficiency for Run II*, W.K. Sakumoto and A. Hocker

[43] CDF Internal note 6101 (2002) *CPR material Counts for CDF Run II* Minsuk Kim, Ray Culbertson, Robert Blair.

[44] CDF Internal note 6368 *Jet$\rightarrow \gamma$ Fake Rate Measurment using the CPR Detector* Heather Gerberich and Ashutosh Kotwal.

[45] Raymond Culbterson, private communications.

[46] Nucl. Phys. Proc. Suppl. **166** (2003) 178-182 *the Di-Photon Background to a Light Higgs Boson at LHC* Z. Bern, L. Dixon, C. Schmidt.

[47] Phys. Rev. Lett. **70**, 2232 (1993) *Measurement of the Cross Section for Production of Two Isolated Prompt Photons in $p\bar{p}$ Collisions at s**(1/2) = 1.8 TeV* F. Abe et al., The CDF Collaboration,

[48] Phys. Rev. **D63**, 114016 (2003) *Beyond Leading Order Effects in Photon Pair Production at the Tevatron.* T.Binoth, J.Ph.Guillet, E.Pilon and M.Werlen.

[49] FermiLab "inquiring minds" web site *Accelerators : high-energy instruments to reveal a new world"* http://www.fnal.gov/pub/inquiring/physics/accelerators/

[50] Phys. Rev. Lett. **73**, 2662-2666 (1994) erratum : Phys. Rev. Lett. **74**, 1891-1893 (1995) *Precision Measurement of the Prompt Photon Cross Section in pp-bar Collisions at sqrt[s]=1.8 TeV* F. Abe et al (CDF Collaboration)

[51] CDF Internal note 1356 *Measurement of Photon CES χ^2 from $\eta \rightarrow \gamma\gamma$ Decays* Robert M. Harris